

# ACOUSTIC EMISSION-BASED MONITORING OF MANUFACTURING PROCESSES INVOLVING BIOMATERIALS

Roshan Mishra

Submitted in Partial Fulfillment of the Requirements  
for the Degree of

*DOCTOR OF PHILOSOPHY*

Approved by:  
Dr. Johnson Samuel, Chair  
Dr. Daniel Walczyk  
Dr. Kristen Mills  
Dr. Henry Scarton  
Dr. Chang Ryu



*Department of Mechanical, Aerospace and Nuclear Engineering*  
Rensselaer Polytechnic Institute  
Troy, New York

[August 2020]  
Submitted July 2020

© Copyright 2020

By

Roshan Mishra

Note: Portions of this thesis may be submitted as part of peer-reviewed publications in the future.

All Rights Reserved

# TABLE OF CONTENTS

LIST OF TABLES .....	viii
LIST OF FIGURES .....	ix
ACKNOWLEDGEMENT .....	xiii
ABSTRACT.....	xiv
1. INTRODUCTION .....	1
1.1 Motivation and Background .....	1
1.2 Research Objective, Scope, and Tasks .....	2
1.3 Thesis Outline.....	4
2. LITERATURE REVIEW .....	7
2.1 Biomaterials: Microstructures and Properties .....	7
2.1.1 Material 1: Bovine Bone.....	7
2.1.2 Material 2: Agarose Hydrogel .....	10
2.2 Acoustic Emission Signal: Background and General Applications in Manufacturing ...	12
2.2.1 Acoustic Emission Signal Basics.....	12
2.2.2 Acoustic Emission Applications in Manufacturing .....	16
2.3 Acoustic Emission Applications in Machining .....	19
2.3.1 Machining Experiments: Macro and Micro-Scale Cutting.....	19
2.3.1.1 Acoustic Emission Sensor Placement in Machining .....	22
2.3.1.2 Acoustic Emission Signal Metrics in Machining .....	23
2.3.2 Acoustic Emission Models in Machining .....	24

2.3.2.1	Acoustic Emission Signal Power Modeling in Orthogonal Cutting .....	24
2.3.2.2	Other Acoustic Emission Modeling Strategies .....	28
2.4	Acoustic Emission Applications in Bone Characterization .....	29
2.5	Hydrophone Signal: Background and General Applications .....	32
2.6	Acoustic-based Characterization of Hydrogels .....	34
2.7	Gaps in Knowledge .....	37
3.	<b>ACOUSTIC EMISSION ANALYSIS OF FAILURE MECHANISMS</b>	
	<b>ENCOUNTERED IN FRACTURE-CUTTING OF BOVINE BONE.....</b>	<b>38</b>
3.1	Bone Microstructure .....	38
3.2	Machining Experiment .....	39
3.3	Experimental Findings.....	41
3.3.1	Failure Mechanisms in Haversian Bone .....	43
3.3.2	Failure Mechanisms in Plexiform-0° Bone.....	46
3.3.3	Failure Mechanisms in Plexiform-90° Bone.....	47
3.3.4	Distinguishing Features in Acoustic Emission Signals .....	47
3.4	Discussion.....	50
3.5	Conclusions .....	54
4.	<b>REVIEW OF A RELEVANT MICROSTRUCTURE-BASED CUTTING FORCE</b>	
	<b>MODEL FOR BONE SAWING.....</b>	<b>56</b>
4.1	Nomenclature.....	56
4.2	Model-related Bone Sawing Experiments .....	57
4.3	Modeling Strategy .....	59

4.4	Cutting Force Equations and Predictions .....	60
4.5	Summary.....	62
5.	MICROSTRUCTURE-BASED MECHANISTIC MODEL FOR BONE SAWING: ACOUSTIC EMISSION SIGNAL POWER PREDICTIONS .....	64
5.1	Acoustic Emission in Bone Sawing.....	65
5.2	Basic Model Assumptions and Energy Dissipation Components .....	67
5.2.1	Model Assumptions .....	68
5.2.2	Shearing and Ploughing Contributions .....	70
5.3	Model Modifications .....	73
5.3.1	Effect of Microstructure Interfaces .....	74
5.3.2	Realistic Tool-Workpiece Intersection .....	75
5.3.2.1	Tool Edge Variation .....	75
5.3.2.2	Workpiece Surface Height Variation .....	76
5.3.2.3	Evaluating the Probability of Cutting Material .....	78
5.3.3	Porosity Effect .....	80
5.4	Model Calibration and Validation .....	81
5.4.1	Estimation of Calibration Coefficients .....	82
5.4.2	Calibration Accuracy .....	82
5.4.3	Model Validation .....	84
5.5	Model Uses for Process Planning.....	86
5.5.1	Predicting Cutting Force Variation.....	86
5.5.2	Predicting Region-specific Variations .....	87
5.6	Conclusions .....	89

6.	A MULTI-SENSOR MODALITY TO MONITOR BULK HYDROGEL GELATION...	90
6.1	Experiment Testbed.....	91
6.1.1	Hydrogel Signal Characterization.....	94
6.1.2	Digital Image Characterization.....	96
6.1.3	Multi-sensor Signal Metric.....	97
6.1.4	Gel-state Estimate: Calibration, Indirect Validation, and Prediction.....	97
6.2	Summary and Limitations.....	101
7.	CONCLUSIONS AND RECOMMENDATIONS.....	103
7.1	Conclusions.....	104
7.1.1	Acoustic Emission Analysis of Failure Mechanisms Encountered in Fracture-cutting of Bovine Bone.....	104
7.1.2	Microstructure-based Mechanistic Model for Bone Sawing: Acoustic Emission Signal Power Predictions.....	105
7.1.3	A Multi-sensor Modality to Monitor Bulk Hydrogel Gelation.....	106
7.2	Directions of Future Research.....	106
7.2.1	Clinically-relevant Studies on Human Bone Specimens.....	107
7.2.2	Exploring Diverse and Realistic Bone Cutting Strategies.....	108
7.2.3	Monitoring Failures in Heterogeneous Materials.....	109
7.2.4	Monitoring Layer-by-layer Hydrogel Printing.....	109
	REFERENCES.....	110
	APPENDICES.....	122
	A.1 Sensor Specifications.....	122

A.1.1	Acoustic Emission Sensor.....	122
A.1.2	Hydrophone.....	123
A.2	Matlab Codes .....	124
A.2.1	Codes used in Chapter 3 .....	124
A.2.2	Codes used in Chapter 5 .....	126
A.3	Supplemental Files.....	128
A.3.1	Permissions for Chapter 2.....	128
A.3.2	Permissions for Chapter 4.....	128
A.3.3	Permissions for Chapter 5.....	129

## LIST OF TABLES

Table 2.1: Hardness and stiffness values of the haversian and plexiform microstructures [4].....	9
Table 2.2: Acoustic emission monitoring in (a) traditional, and (b) non-traditional manufacturing processes [3]. .....	18
Table 3.1: Machining conditions. ....	41
Table 3.2: Differentiating features in the Acoustic emission signals. ....	48
Table 4.1: Microstructure-specific shear stress values [5].....	60
Table 4.2: Calibration constants [5].....	62
Table 5.1: Summary of the experimental conditions [5]. ....	65
Table 5.2: Observed chip thickness values. ....	72
Table 5.3: Acoustic emission model calibration coefficients. ....	82
Table 6.1: Sample thicknesses considered in this study. ....	92
Table 6.2: The half-time value corresponding to sample thickness L. ....	99
Table 6.3: Calibration constants. ....	99

## LIST OF FIGURES

Figure 1.1: Outline of the research objective.....	2
Figure 2.1: (a) Location of haversian and plexiform regions in the bovine femur, and microscopy images of (b) the haversian, and (c) the plexiform regions [4]. .....	9
Figure 2.2: (i) Gelation process in agarose solutions [11], and (ii) evolution of the absorbance with gelation [23]. .....	11
Figure 2.3: Viscosity dependence on temperature, ‘1’- 0.8% (g/mL) agarose, ‘2’- 0.4% (g/mL) agarose, and ‘3’- water [12]. .....	12
Figure 2.4: Acoustic emission released by a localized source monitored by a surface-based transducer [1]. .....	13
Figure 2.5: Principle of acoustic emission signal collection [37]. .....	14
Figure 2.6: Acoustic emission burst or waveform [41]. .....	15
Figure 2.7: Burst and continuous type acoustic emission signals [44]. .....	16
Figure 2.8: (i) Acoustic emission sources in orthogonal cutting, (ii) micrographs of flow-type and serrated chips collected, and (iii) acoustic emission signals corresponding to the chip types [32]. .....	20
Figure 2.9: (a) Schematic of the experiment setup, and (b) a spectrogram from multiple scratches [35]. .....	22
Figure 2.10: Acoustic emission sensor mounted on - (a) cutting tool during turning (rotating workpiece) [32], and (b) workpiece during milling (rotating cutting tool) [77]. .....	23
Figure 2.11: Machining geometry in orthogonal cutting – (a) cutting force diagram, (b) shear place, and (c) tool face [43]. .....	26
Figure 2.12: (a) Cutting mechanisms contributing to acoustic emission generation in orthogonal machining, and (b) a plot of experimental vs. theoretical $AE_{rms}$ showing good correlation [43].	28
Figure 2.13: Plot of model and experimental acoustic emission for tool touch-off detection [79]. .....	29
Figure 2.14: (a) Plot of the calculated and the estimated depth of cut, and (b) the corresponding geometry of the milled specimen [31]. .....	29
Figure 2.15: (a) Micrograph of a longitudinal specimen showing cracks along the microstructures – O- osteon, I-interstitial matrix, and c-cement line, (b) three clusters observed in acoustic emission amplitudes, and (c) total number of acoustic emission hits corresponding to the three clusters [90]. .....	31
Figure 2.16: Wavelet energy ratio of the acoustic emission signal during bone micro-drilling [53]. .....	32
Figure 2.17: Hydrophone signal from a water drop impact [105]. .....	33

Figure 2.18: (a) Hydrophone signal evolution and the video stills corresponding to a droplet splash (top), and bubble formation (bottom), and (b) spectrogram from a droplet study with the high-frequency component corresponding to the bubble resonance [108].	34
Figure 2.19: (i) Ultrasound horn operation, (ii) a metric determined by the load response, showing peaks around the two resonance frequencies, and (iii) gelation curves for two solvent amounts, obtained at peak-1(a) and peak-2 (b) [115].	35
Figure 2.20: Comparison of young's modulus against the ultrasound modulus for different hydrogel concentrations [117].	36
Figure 2.21: (a) Cartoon of the experiment setup showing the locations of the hydrophone inside the gel medium, and (b) shock profiles determined by the hydrophone at different locations [103].	36
Figure 3.1: Cartoon of the orthogonal cutting experiment setup (not to scale) - (a) top view, and (b) front view.	40
Figure 3.2: Force and acoustic emission signals from haversian bone machining.	42
Figure 3.3: Cartoons of failure mechanisms observed in the experiments. [Note: Haversian bone is shown as osteons embedded in the interstitial matrix, and plexiform bone is shown as alternating layers of lamellar and woven regions]	43
Figure 3.4: Dominant failure mechanisms observed in the haversian specimens.	44
Figure 3.5: Dominant failure mechanisms observed in the plexiform specimens.	45
Figure 3.6: Fracture areas measured for different failure mechanisms.	51
Figure 3.7: Normalized (a) cutting energy & cutting force, and (b) acoustic energy for the different failure mechanisms.	53
Figure 4.1: High-speed, linear-cutting fixture [125].	58
Figure 4.2: Example of cutting/thrust forces corresponding to the three identified regions in the bone sample [5].	58
Figure 4.3: Flowchart for the force prediction model [5].	59
Figure 4.4: Plots of (a) cutting force, and (b) thrust force prediction in the transition region [5].	62
Figure 5.1: (a) Bone sample with haversian region on the left and plexiform region on the right, and (b) acoustic emission signal as the tool cuts the bone sample from left to right.	66
Figure 5.2: Experimental acoustic emission signal power, i.e., $(AE_{rms})^2$ , from the haversian and plexiform bones. [Note: Data Sets 1, 2, and 3 correspond to DOCs 1.8 – 3.8 $\mu\text{m}$ , 4.0 – 5.4 $\mu\text{m}$ , and 5.6 – 9.4 $\mu\text{m}$ , respectively]	67
Figure 5.3: Cutting tool geometry - (a) rounded cutting-edge framework for bone sawing, (b) shear cutting sub-problem, and (c) ploughing deformation sub-problem.	69
Figure 5.4: Mapping (FcS), (FtS), and (FfS) to a Merchant's circle applied to the shear-dominated sub-problem.	71

Figure 5.5: (a) Cartoon of the rounded cutting tool edge showing variable edge profiles, (b) height profiles of two cutting tool edge measurements – lowest and highest variations, and (c) corresponding pdfs of the two edge profiles.....	76
Figure 5.6: Microscopy image of osteon on machined workpiece surface after (a) 2.93 $\mu\text{m}$ DOC, and (b) 9.37 $\mu\text{m}$ DOC showing damage around the osteon (Scale: 25 $\mu\text{m}$ ), the surface height profiles and the pdfs in (c) and (d) correspond to the two line-sections marked in (a) and (b), respectively. ....	77
Figure 5.7: (a) Cartoon showing the interaction of the cutting tool edge (baseline A'-B') and the workpiece surface (baseline A-B) for a nominal DOC ( $t_0$ ), showing actual material removal, (b) interaction of the probabilities at $t_0$ 2.93 $\mu\text{m}$ , based on low and high cutting edge variations, (c) interaction of the probabilities at $t_0$ 9.37 $\mu\text{m}$ , based on low and high cutting edge variations, and (d) the resultant $p(t_0)$ plot for the haversian, along with a similarly obtained plot for the plexiform region.....	79
Figure 5.8: ImageJ analysis showing porosity area fraction ( $A_p$ ) values of 0.10 and 0.06 for typical (a) haversian, and (b) plexiform sample, respectively. ....	80
Figure 5.9: Overall model calculations, calibration, and validation process. ....	81
Figure 5.10: Calibration accuracy curves for acoustic emission prediction, in terms of the scatter of the Mean for (a) haversian and (b) plexiform regions, and the overlay of the Range against DOC for (c) haversian and (d) plexiform regions.....	83
Figure 5.11: Transition region characterization map, (a) original image, (b) processed image, and (c) area fractions ( $A_i$ ) across multiple maps. [Refer Conward [5]].....	85
Figure 5.12: Acoustic emission model validation in terms of the overlay of the Range against DOC for the transition region. ....	86
Figure 5.13: (a) Cutting force, and (b) thrust force range predictions based on the modeled force [5]......	87
Figure 5.14: (a) Image showing cancellous bone alongside cortical bone [130], and (b) the AE signal power predicted in the posterior region of the cortical bone, and the cancellous bone. [Note: For the cancellous bone, $n = 0$ in Eq. 5.10] .....	88
Figure 6.1: (a) Photo of the experiment setup, and (b) a schematic of the steps involved in the experiments. ....	91
Figure 6.2: Hydrophone signal for gelation of a 2.5 mm thick sample, showing the multiple bursts caused by the 'air hammer' application. ....	94
Figure 6.3: (a) Typical hydrophone signal burst due to 'air hammer' application, and (b) a scalogram of the signal burst showing dominant frequency components around 400 Hz.....	94
Figure 6.4: Change in attenuation coefficient from the hydrophone signals corresponding to different samples. ....	96
Figure 6.5: Video stills of a 20 mm thick layer at (a) 0 min, and (b) 100 min. [Note: The blue line shows the region where image intensity was calculated] .....	96
Figure 6.6: Flowchart for finding gel-state estimate in the case of a 20 mm sample. ....	98

Figure 6.7: Temperature and image intensity evolution during the gelation of a 20 mm sample. .... 99

Figure 6.8: Comparison of gel-state estimate with stiffness in a 20 mm thick sample. .... 100

Figure 6.9: Estimated gel-states for different sample thicknesses. [Note: validation is done beyond 40 min for the 20 mm thick layer, as shown by the dashed box]..... 101

Figure 7.1: Acoustic emission-monitored fracture study on human femur bone [95]...... 107

Figure 7.2: Sagittal (left), and sternal (right) saws [155]...... 108

## **ACKNOWLEDGEMENT**

The research presented in this thesis has been made possible through funding from the United States National Science Foundation (NSF) research grants - CMMI 13-51275, and CMMI 14-62648. The NSF educational grant DUE 12-45910 and internal funds from Rensselaer Polytechnic Institute (RPI) are also acknowledged for supporting my graduate studies. I am grateful to Prof. Johnson Samuel for his guidance in this research. I am also thankful to my colleagues at RPI's Nano-M3 Design Lab, for discussions with them were helpful in overcoming some research bottlenecks. Lastly, I would like to express my gratitude to Prof. Daniel Walczyk, Prof. Kristen Mills, Prof. Henry Scarton, and Prof. Chang Ryu for serving on my Ph.D. Committee.

## ABSTRACT

The research presented in this thesis deals with exploring the effectiveness of using acoustic sensing modalities to monitor manufacturing processes involving two specific biomaterials, viz. bovine cortical bone, and agarose hydrogel. For bovine cortical bone, the acoustic emission signals collected during fracture and shear-based cutting experiments are investigated and related to the observed failure mechanisms. An acoustic pressure signal-based monitoring approach is proposed for estimating the gel-state in bulk agarose hydrogel samples undergoing gelation.

First, orthogonal cutting experiments are conducted on haversian and plexiform bone specimens harvested from the bovine femur. The specimens are machined at 70  $\mu\text{m}$  depth of cut and 800 mm/min cutting speed, to induce fracture-dominant cutting. With the aid of a high-speed camera, microstructure-specific failure mechanisms in the haversian and plexiform specimens are observed, and their distinct acoustic emission features are studied. Compared to the measured cutting force, the acoustic emission signal is seen to be a more efficient in distinguishing the different failure mechanisms. Differentiating features are derived for each of the specific failure mechanisms using a combination of their specific acoustic emission signals and measured crack lengths.

Next, shear-based cutting of bovine bone is studied using single-tooth bone sawing experiments. More specifically, efforts are undertaken to model the acoustic emission signal power, as a function of the specific cortical bone microstructures and the depth of cut encountered by the sawtooth. First, the acoustic emission signal characteristics from the sawing experiments are related to the haversian and plexiform regions of the cut. The acoustic emission signal power is then modeled based on the energies dissipated in the shearing and ploughing zones encountered

by the rounded cutting edge of the sawtooth. For this calculation, the rounded cutting-edge geometry of the sawtooth is divided into a combination of (i) shear-based cutting from a negative rake cutting tool, and (ii) ploughing deformation from a round-nose indenter. The spread seen in the acoustic emission signal power values is captured by modeling the variations in the sawed surface height profile, tool cutting edge geometry, and porosity of the bone. The acoustic emission model is first calibrated on the pure haversian and plexiform regions of the bovine cortical bone and then validated on the transition region containing both haversian and plexiform microstructures. The model shows a good correlation ( $>0.9$ ) between predicted and experimentally measured acoustic emission signal power values and is useful for process planning purposes.

Finally, a multi-sensor modality involving both acoustic pressure signals and digital images is proposed as an alternative to estimate the gel-state of a bulk agarose hydrogel sample undergoing thermo-reversible gelation at room temperature. Here, a hydrophone is used to monitor the acoustic waves generated in the sample by an external, low-impact energy source. The digital camera is used to monitor the image intensity evolution as the hydrogel changes from a transparent, solution-state to an opaque, gel-state. The two signals are then combined using an empirical relationship to obtain a gel-state estimate. The preliminary findings indicate that this approach holds the promise of being implementable in a 3D printing environment.

# 1. INTRODUCTION

## 1.1 Motivation and Background

Acoustic emission (AE) refers to transient elastic waves generated in a specimen by the rapid release of energy [1]. The source could be a variety of events like plastic deformation or crack formation, due to factors like external forces or temperature gradients [1]–[3]. AE is widely used in the non-destructive evaluation of materials. Applications of AE include manufacturing process control [3]. The studies described in this thesis involve the use of acoustic sensors to monitor manufacturing processes involving two classes of biomaterials, namely hard biomaterial (bovine bone), and soft biomaterial (tissue-mimicking hydrogel).

For the hard biomaterial application, the hypothesis that AE signals can provide insight into the microstructure-specific failure mechanisms seen in the bovine bone will be tested. Bovine cortical bone consists of two distinct regions, viz. haversian and plexiform bone [4], [5]. Haversian bone consists of cylindrical structures called osteons that are surrounded by cement lines and embedded in the interstitial matrix, whereas plexiform bone consists of alternating layers of lamellar and woven regions [4]. During machining, these microstructures can be expected to have different failure modes. Understanding the nature of the AE signals corresponding to the different failure mechanisms will help in establishing a framework for AE-based monitoring of the bone cutting process.

For the soft biomaterial application, tissue-mimicking hydrogel will be studied in an environment compatible with 3D printing. More specifically, agarose hydrogel undergoing thermo-reversible gelation will be studied [6]–[8]. An acoustic sensing -based technique will be explored to monitor the gelation process, i.e., the conversion of hydrogel from a solution state to

a gel state. This will help in developing modalities for effective closed-loop control of bioprinting processes commonly using hydrogels [9]–[12].

## 1.2 Research Objective, Scope, and Tasks

The overall objective of this research is to explore the effectiveness of using acoustic sensing modalities to monitor manufacturing processes involving two classes of biomaterials, viz. hard biomaterials (bovine bone), and soft biomaterials (tissue-mimicking hydrogel). This objective is achieved through research efforts focused in three thrust areas, as outlined in Fig. 1.1.

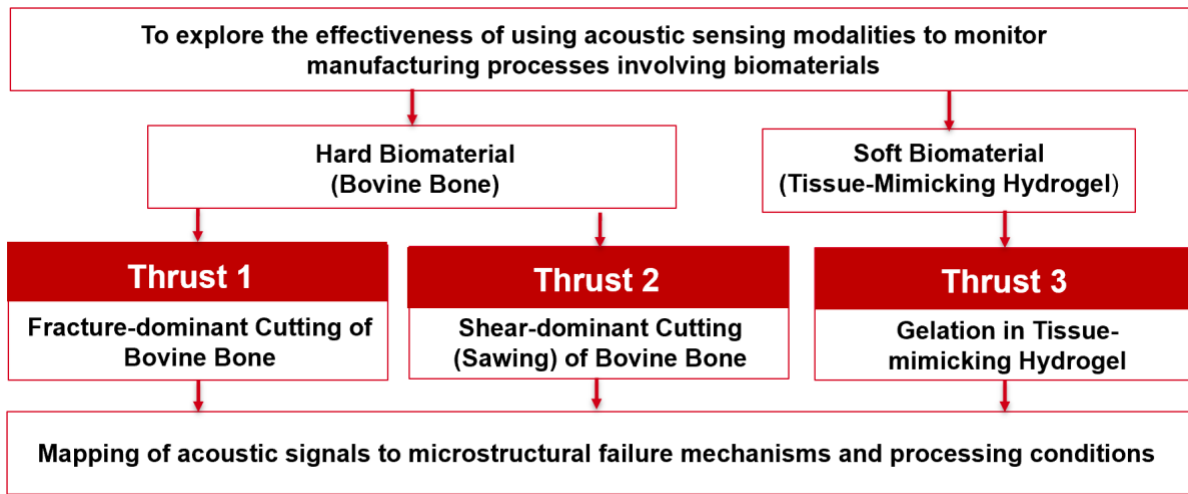


Figure 1.1: Outline of the research objective.

The details of the three research thrusts are as follows:

**Thrust 1- Hard biomaterial: Fracture-dominant cutting of bovine bone:** On this front, the work involves the use of AE signals to distinguish the microstructure-specific failure mechanisms encountered during the fracture-cutting of bone. Machining experiments will be conducted under conditions that induce fracture-dominant failures. Cutting forces and AE signals will be correlated to specific failure mechanisms observed using high-speed imaging. The work

will enable the development of AE signal metrics to identify specific fracture-related failures in the bovine bone.

**Thrust 2- Hard biomaterial: Shear-dominant cutting (sawing) of bovine bone:** This study will involve modeling of the AE signal power trends, as a function of the specific cortical bone microstructures and the depth of cut encountered by the sawtooth. The AE response will be modeled based on the cutting energy dissipation as well as the microstructural features. The model will first be calibrated on the pure haversian and plexiform regions of the bovine cortical bone and then validated on the transition region containing both haversian and plexiform microstructures. The work is aimed at using AE signals for effective process planning in bone sawing.

**Thrust 3- Soft biomaterial: Monitoring gelation in tissue-mimicking hydrogel:** The overarching objective of this thrust is to estimate the gel-state of the hydrogel construct using both acoustic signals and digital images. This work will involve hydrogel constructs that are subjected to thermo-reversible gelation. A hydrophone will be used to measure acoustic waves generated in the sample by an external, low-impact energy source. A digital camera will also be used to get information about the image intensity as the gelation causes the hydrogel to change from being transparent to opaque. The two signals will then be combined to get a gel-state estimate of the hydrogel. This effort is aimed at implementing gelation monitoring modalities during 3D printing of hydrogels.

**Scope:** The orthogonal cutting experiments for Thrust 1 will be conducted on separate haversian and plexiform workpieces harvested from the bovine cortical bone. The cutting conditions will be selected to ensure fracture-based cutting. Forces and AE signals will be collected during the experiments, which will also be monitored by a high-speed camera. The Nano-30 AE

sensor from Physical Acoustics will be used in this study (refer Appendices for sensor details). The sawing experiments for Thrust 2 will be conducted on a high-speed linear sawing apparatus used in the research of James et al. [13] at Tufts University. The sawing experiments will be in the shear-cutting regime. The typical workpiece to be studied in Thrust 2 will be a bone sample containing distinct haversian and plexiform regions, as well as an intermediate ‘transition’ region comprising of a blend of both haversian and plexiform microstructures [5]. Similar to Thrust 1, both force and AE signals will be collected, and the same Nano-30 AE sensor will be employed. In Thrust 3, agarose hydrogel will be studied. The thermo-reversible gelation will take place at room temperature without any thermal constraints. The experiment setup will be built around Aerotech motion stages. During the gelation process, pressure waves will be measured by a hydrophone type 8103 from Bruel & Kjaer (refer Appendices for sensor details). A digital camera will also be employed to monitor the change in the optical nature of the gel during gelation.

### **1.3 Thesis Outline**

The remainder of this thesis is organized as follows: Chapter 2 provides a review of the published literature in relevant areas. This chapter will begin with an overview of the biomaterials under consideration, i.e., bovine cortical bone and agarose hydrogel. Details on the material microstructures and the properties will be presented. This will be followed by a review of the AE signal background and general applications in manufacturing. Specific AE applications in machining and bone characterization will also be reviewed. On the hydrogel front, both hydrophone applications as well as current acoustic monitoring applications in hydrogel characterization will be reviewed. Finally, based on the review of literature, specific gaps in knowledge to be addressed by this thesis will be identified.

Chapter 3 presents the experimental observation of the different fracture-based failure mechanisms in the microstructure of bovine cortical bone during orthogonal cutting. Both cutting forces and AE signals are monitored. Complementary nature of the information from the cutting forces and the AE are described. Distinguishing AE characteristics of the identified failure mechanisms are discussed. The content of this chapter falls under Thrust 1, as identified in Fig. 1.1.

Chapter 4 presents a brief review of a recently-developed microstructure-based cutting force model in bone sawing [5]. This review chapter is presented in this thesis for the sake of continuity, since the cutting force predictions from the aforementioned model feed into the AE model calculations described ahead in Chapter 5.

Chapter 5 focusses on modeling AE signal power generated during sawing or shear-cutting of the bovine bone. The model accounts for different sources of energy-release including shearing, friction, and ploughing. Variation in the experimental data is modeled using factors such as tool/workpiece interaction, and porosity, based on evidence obtained during the experiments. The model is first calibrated on the pure haversian and plexiform regions of the bovine cortical bone and then validated on the transition region containing both haversian and plexiform microstructures. This work falls under Thrust 2, as identified in Fig. 1.1.

Chapter 6 presents a multi-sensor modality involving both acoustic pressure signals and digital images as an alternative to estimate the gel-state of a bulk agarose hydrogel sample undergoing thermo-reversible gelation at room temperature. The preliminary findings indicate that this approach holds the promise of being implementable in a 3D printing environment. This work falls under Thrust 3, as identified in Fig. 1.1.

Finally, Chapter 7 summarizes the findings in light of the studies in Thrusts 1-3. The specific contributions of this work regarding the effectiveness of using acoustic sensing modalities to monitor manufacturing processes involving bovine bone and tissue-mimicking hydrogels will be presented along with suggestions for future research directions.

## **2. LITERATURE REVIEW**

This chapter reviews the application of AE and acoustic-based monitoring techniques in manufacturing processes involving biomaterials. First, a background is provided for the two types of biomaterials being studied, i.e., bovine bone and tissue-mimicking hydrogel. Next, the AE sensing approach and applications in manufacturing processes are described, followed by a section on prior studies involving AE application in machining. Next, AE application to bone characterization is described. The background and general applications of hydrophone-based acoustic monitoring are then described, followed by a section on acoustic-based monitoring and characterization of the tissue-mimicking hydrogel. Lastly, the gaps in knowledge in light of the current state of research are highlighted.

### **2.1 Biomaterials: Microstructures and Properties**

Biomaterials can be broadly classified as hard and soft biomaterials. Under the hard biomaterials category, bone has been studied extensively [5]. In the soft biomaterials category while many candidates exist, tissue-mimicking hydrogels have been studied to obtain insight into the responses of soft tissues and muscles [14]. In this present research, bone and tissue-mimicking hydrogel will be investigated. More specifically, bovine bone and agarose hydrogel are considered as candidates.

#### **2.1.1 Material 1: Bovine Bone**

The bovine bone has microstructures very similar to the human bone, which makes it a suitable candidate for machining studies aimed at understanding bone surgeries [5]. Specifically, bovine bone consists of two distinct, easily identifiable parts – cancellous bone and cortical bone

[5], [15]. The cancellous bone is spongy and highly porous [5], [16]. On the other hand, the cortical bone is hard and dense, and exhibits interesting microstructures [4].

The bovine cortical bone is anisotropic and can be divided into haversian and plexiform regions [4], [5]. The location of these two regions within the bovine femur is dictated by the compressive and tensile forces acting on the bone [17]. As described by Conward and Samuel [4], a circular cross-section on a bovine femur can be divided into 4 quadrants – lateral, anterior, medial, and posterior. Of these quadrants, anterior and posterior are predominantly plexiform and haversian, respectively. Fig. 2.1(a) shows the location of haversian and plexiform regions in the bovine femur. Haversian bone consists of cylindrical structures called osteons in an interstitial matrix. The osteons are surrounded by cement lines. On the other hand, the plexiform bone consists of alternating woven and lamellar layers. Fig. 2.1(b)&(c) show the microscopy images of haversian and plexiform regions, along with the different constituent microstructures.

The constituent microstructures in the bovine cortical bone have very different material properties as well. Conward and Samuel [4] conducted nano-indentation tests on the different haversian and plexiform microstructures to determine the corresponding elastic modulus and hardness values, which are shown in Table 2.1.

It can be seen from Table 2.1 that in haversian bone, the cement line interface has much lower stiffness and hardness than the osteon and interstitial matrix. Thus, the presence of this weak interface will affect the failure mechanisms in haversian bone under external forces and stresses. In plexiform bone, the planar lamellar and woven regions have very different stiffness and hardness values and will thus affect the failure mechanisms in plexiform bone.

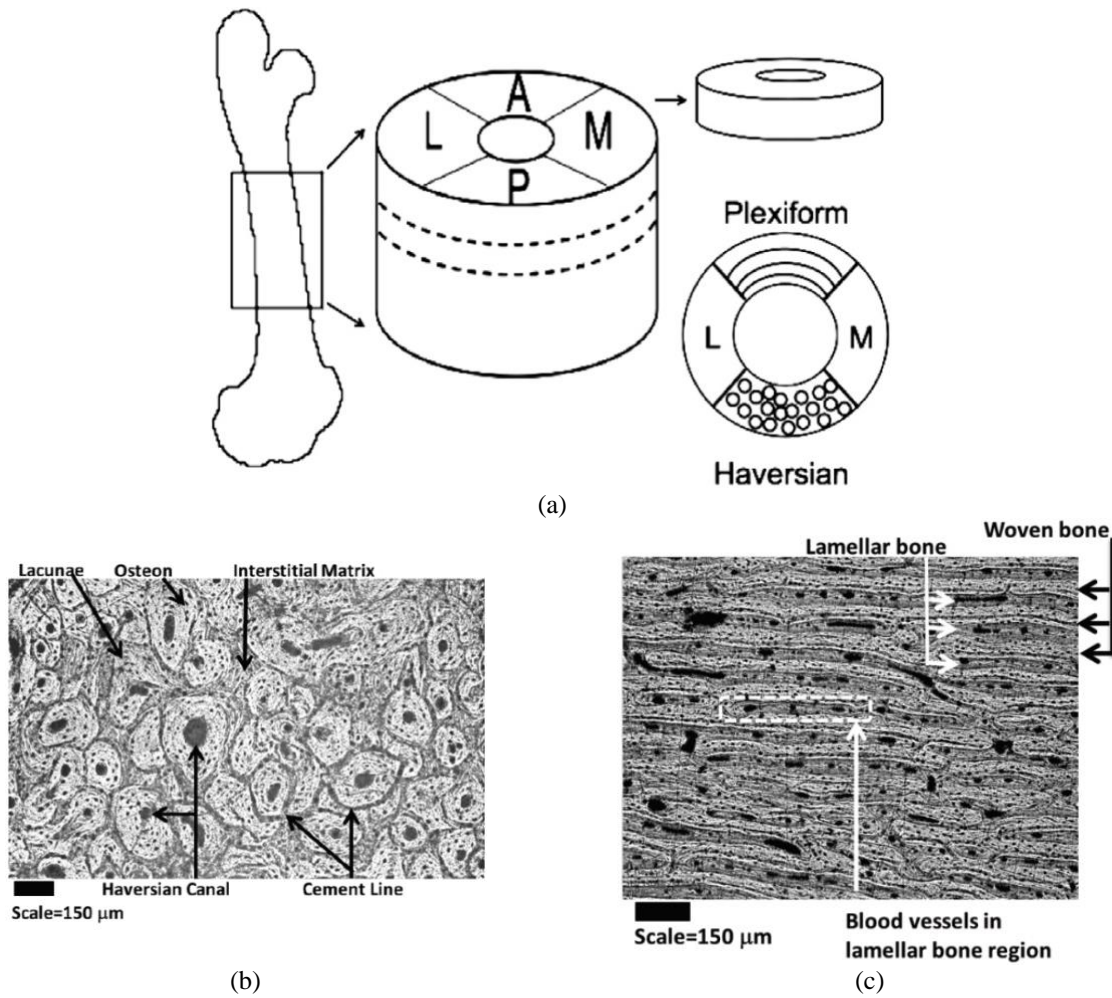


Figure 2.1: (a) Location of haversian and plexiform regions in the bovine femur, and microscopy images of (b) the haversian, and (c) the plexiform regions [4].

Table 2.1: Hardness and stiffness values of the haversian and plexiform microstructures [4].

Elastic modulus	E (GPa)
Haversian bone – Osteon	$35.8 \pm 3.50$
Haversian bone – Interstitial Matrix	$36.4 \pm 3.08$
Haversian bone – Cement Line	$22.0 \pm 0.89$
Plexiform Bone – Woven	$38.9 \pm 1.63$
Plexiform Bone – Lamellar	$30.3 \pm 1.89$
Hardness	H (GPa)
Haversian bone – Osteon	$1.67 \pm 0.21$
Haversian bone – Interstitial Matrix	$1.73 \pm 0.24$
Haversian bone – Cement Line	$0.81 \pm 0.15$
Plexiform Bone – Woven	$1.91 \pm 0.10$
Plexiform Bone – Lamellar	$1.31 \pm 0.18$

It is important to investigate the failure mechanisms in bone microstructures so as to understand their behavior under conditions encountered in bone surgeries, which are essentially variants of different machining processes. As such, machining studies have been conducted on the bovine bone while considering the inherent anisotropy [16], [18]. Most of these studies are in the domain of orthogonal cutting [5], [19]–[22], as the simpler cutting process allows for a clearer understanding of the expected outputs under different cutting conditions. Recently, Conward [5] conducted extensive machining studies on the haversian and plexiform bones, which highlighted the need for monitoring specific microstructural failure mechanisms. Sections 2.2-2.4 will review the literature concerning the application of the suitable sensing approach in this regard, i.e., AE-based monitoring.

### **2.1.2 Material 2: Agarose Hydrogel**

Agarose hydrogel is classified as a tissue-mimicking hydrogel based on the gel properties of stiffness and water retention [6]–[8]. Agarose gel has been widely studied for reasons like the thermo-reversible gelation, and the fast kinetic of the gelation process [23]–[26].

Aqueous solutions of agarose polymer undergo a thermo-reversible gelation process in cooling. At higher temperatures, the agarose chains form random coils. But in cooling, the chains transition into double-helical structures, eventually forming ‘micro aggregates’ [23]. The consequence of this gelation process is the conversion of the agarose solution to a gel state. During this gelation process, the optical nature of the hydrogel also changes from a transparent state to a more opaque state. Fig. 2.2 (i) shows the thermo-reversible change in agarose solution form (a) random coils state to (c) micro-aggregates state. Fig. 2.2(ii) shows the schematic of the gelation process in agarose, in terms of absorbance.

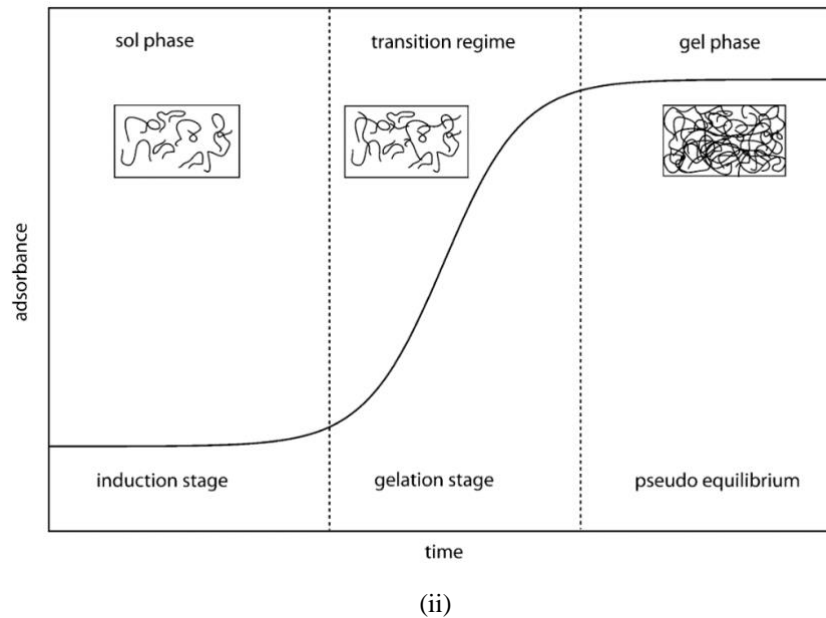
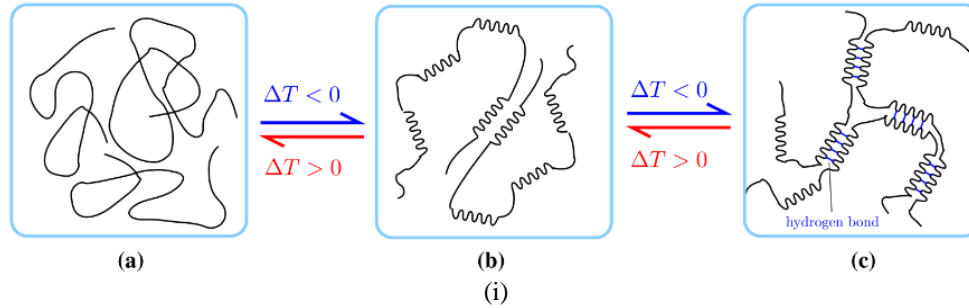


**Figure 2.2: (i) Gelation process in agarose solutions [11], and (ii) evolution of the absorbance with gelation [23].**

It is important to understand the viscoelastic nature of the hydrogel in order to effectively perform bioprinting processes. Also, the evolution of the hydrogel stiffness with temperature needs to be studied to ensure the structural integrity of hydrogel constructs being printed. The change in physical properties of agarose hydrogel with temperature, like storage/relaxation moduli and viscosity, has been well studied [24], [27], [28]. Pokusaev et al. [12] conducted thermokinetics and rheology characterization of agarose hydrogels. Fig. 2.3 shows the plots of temperature-dependent viscosities for agarose solution at two levels of concentrations (0.8% and 0.4% g/mL), as well as the viscosity of water. The plot clearly shows a transition around temperature 35 °C, which points to the transition between the gel and the solution state of the hydrogel.

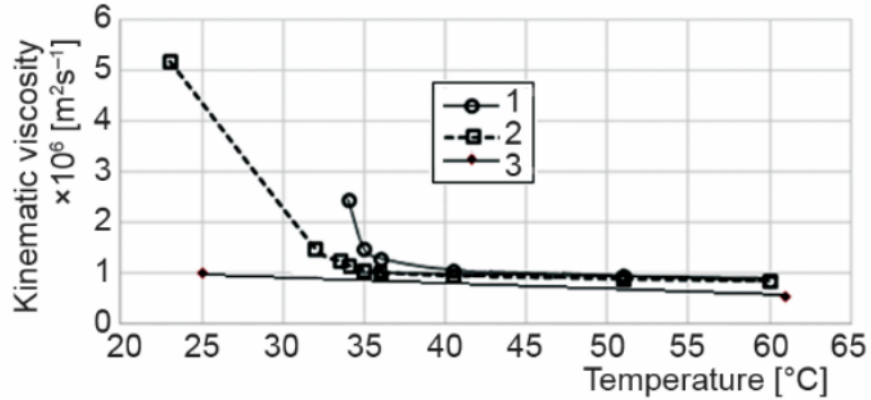


**Figure 2.3:** Viscosity dependence on temperature, ‘1’- 0.8% (g/mL) agarose, ‘2’- 0.4% (g/mL) agarose, and ‘3’- water [12].

Monitoring gelation in agarose is important from a process monitoring standpoint. The typically lower concentrations of aqueous solutions ( $\leq 1\%$ ) dictate that the sensing modality should be capable of working in a fluid environment. As such, a suitable sensing mechanism is that of a hydrophone-based acoustic pressure sensor. Sections 2.5-2.6 will review the literature describing this sensing approach in the context of the hydrogel.

## **2.2 Acoustic Emission Signal: Background and General Applications in Manufacturing**

This section will first describe the basics of the AE signal generation and the metrics derived from the signal. Then, the general application of AE monitoring in manufacturing processes will be discussed.

### **2.2.1 Acoustic Emission Signal Basics**

Acoustic Emission or AE, refers to the phenomena where high-frequency elastic waves are generated in sudden release of energy from sources like fracture and plastic deformation [1]–[3]. As shown in Fig. 2.4, a local source inside a specimen will radiate energy, part of which gets converted into elastic waves [1]. A surface-based transducer will monitor the surface motion due

to these elastic waves. Thus, the AE signal could be used as a means to study and analyze the source-events like fracture and plastic deformation.

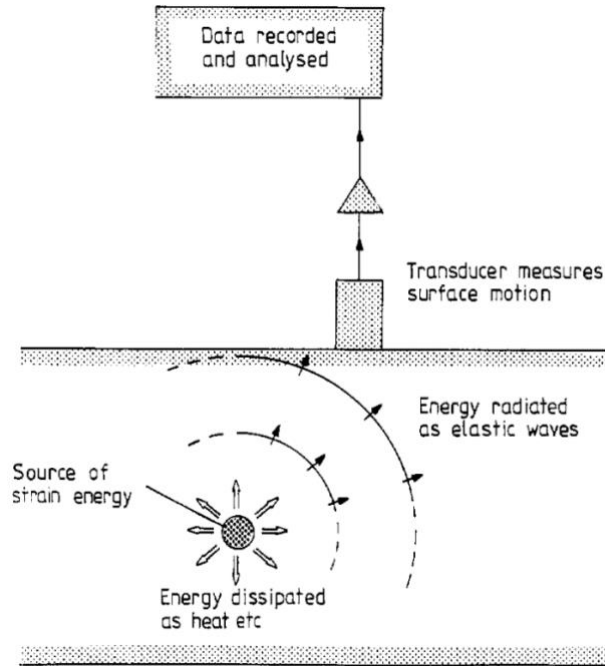


**Figure 2.4: Acoustic emission released by a localized source monitored by a surface-based transducer [1].**

As mentioned by Wadley et al. [2], there is no consensus on the process of AE generation from different sources. A common approach has been to study the AE as analogous to seismology and model the AE source as one generating a dynamic force field. The force field change propagates through the specimen consequently resulting in the mechanical disturbance at the site of the AE sensor [29].

The AE sensors are piezoelectric transducers that convert the small surface displacements into electrical signals. The piezoelectric transducers are usually made from lead zirconate titanate [1], [30]–[32]. The coupling medium between the sensor and the specimen could be any non-attenuating, fluid-like vacuum grease [1], [33]–[36].

Fig. 2.5 shows the principle of the AE technique starting with the AE sensor and ending with the electrical signal generated by the AE events. As mentioned by Michlmayr et al. [37], the

AE sensor can be either resonance or broadband type, which will dictate the frequency sensitivity of the sensor. The vibrations measured by the sensor are transformed into a voltage signal which is further amplified before passing on to the acquisition board, wherein the signal is converted into digital form. Finally, the AE signal is visualized, processed, and analyzed. As seen from the representative AE signal in Fig. 2.5, based on the application of a threshold, the start, and the end of the AE events can be determined.

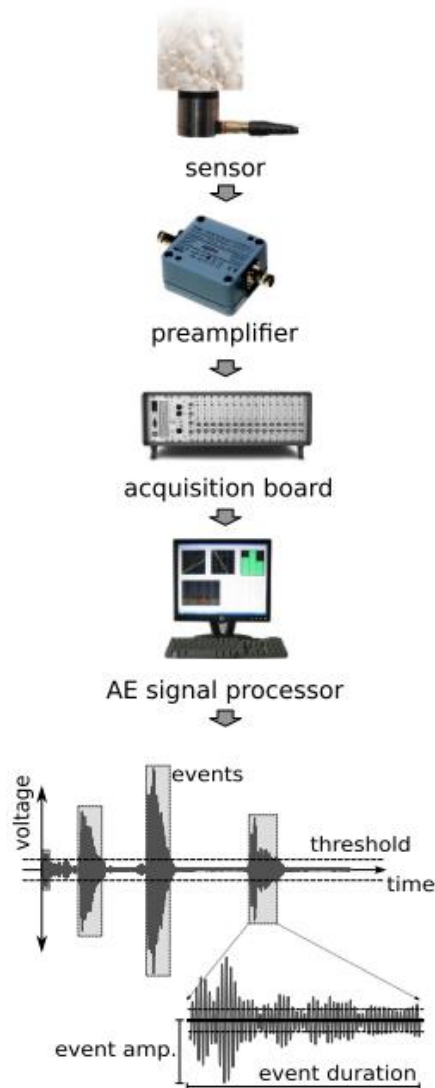


**Figure 2.5: Principle of acoustic emission signal collection [37].**

In general, the signals corresponding to the AE events, are of two types – (i) high-amplitude, discrete ‘burst’ type, and (ii) low-amplitude, continuous type. The nature of the AE

signal is determined by the sources contributing to AE [30]. For instance, ‘burst’ type AE signal is typically associated with fracture [38]–[40]. Depending on the type of the AE signal, different metrics can be derived for process analysis.

As mentioned by Wadley et al. [2], there are different ways for AE signal processing – (i) Counting, (ii) Energy Analysis, (iii) Amplitude Analysis, and (iv) Frequency Analysis. The suitability of these approaches depends on the nature of the measured AE signal. The AE signal could consist of discrete ‘bursts’. In such cases, applying a threshold on the signal allows for counting the times the signal crosses the threshold amplitude. This metric, ‘counts’, is a measure of the strength of the AE signal burst. Fig. 2.6 shows a typical AE burst showing ‘counts’ as well as other features like rise time and peak amplitude.

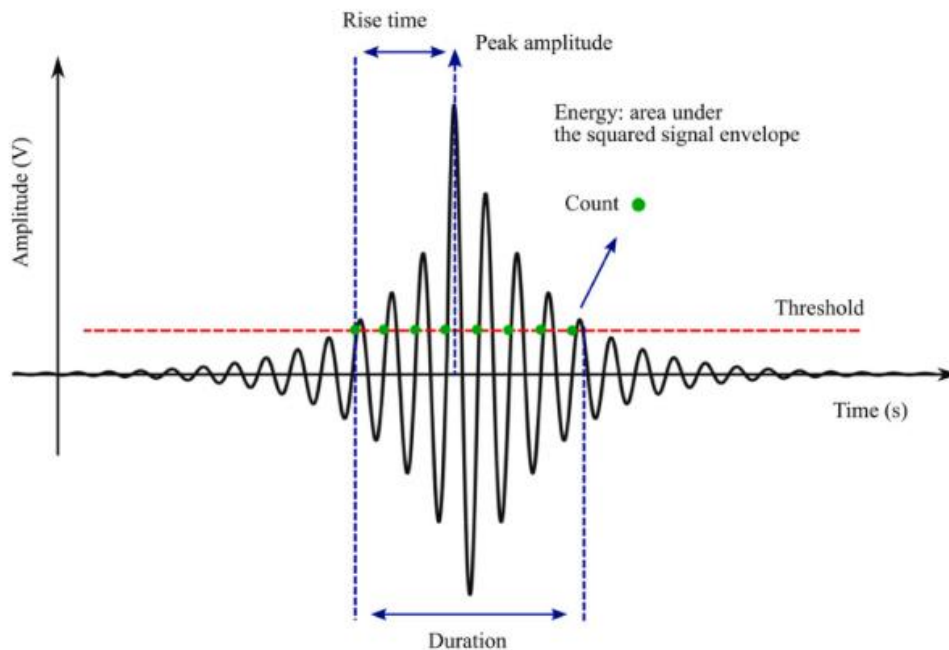


**Figure 2.6: Acoustic emission burst or waveform [41].**

But in instances where the AE signal is more continuous, for example, friction will often generate a continuous AE, unlike fracture which results in AE bursts, it is more beneficial to analyze the AE signal energy. Metrics associated with AE energy analysis are  $AE_{rms}$  (AE signal root mean square) and  $(AE_{rms})^2$  [1], [2].  $(AE_{rms})^2$  is the energy rate or the ‘power’ of the AE signal,

and it allows for an approach to get insight into the energy dissipation rate in a specific process, e.g. orthogonal cutting of metals [42], [43]. Fig. 2.7 shows AE burst and continuous type signals for comparison. The continuous type signal can also be thought of as consisting of multiple bursts or waveforms that are so closely spaced in time that they cannot be isolated.

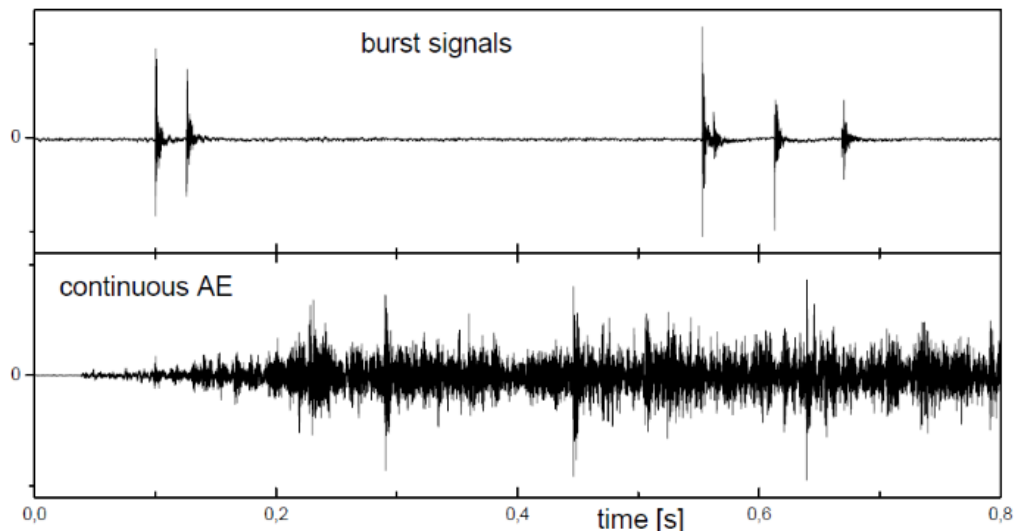


**Figure 2.7: Burst and continuous type acoustic emission signals [44].**

Lastly, amplitude and frequency analyses have been applied to both discrete and continuous AE signals. Both approaches have been used to monitor a wide variety of processes [33], [40], [45]–[50]. Frequency analysis is of particular interest in cases where different sources are expected to generate elastic waves of different frequencies. In composite materials, fractures in different constituents will exhibit different AE frequency ranges [2]. Several studies in composite materials have explored the frequencies associated with the different failure mechanisms [33], [34], [51]–[53]. The phenomena of the existence of multiple frequency bands in an AE signal allow for the implementation of the wavelet analysis approach, particularly in machining processes [53]–[55].

## **2.2.2 Acoustic Emission Applications in Manufacturing**

This section will discuss the particular application of AE in the field of manufacturing.

Table 2.2(a) shows some of the traditional manufacturing processes involving cutting and shearing mechanisms. Table 2.2(b) shows AE monitoring in some non-traditional manufacturing processes. A wide variety of manufacturing process phenomena could be monitored by AE. It should be noted that this table retrieved from Dornfeld [3] is not exhaustive and the traditional manufacturing processes listed here are processes related to machining. The AE monitoring of non-traditional manufacturing processes is intended to present the versatility of the AE monitoring in terms of the different processes and energy sources.

AE monitoring of machining-related processes continues to be explored. Since the 1980s, AE monitoring has been used in metal turning to predict the machining outputs under different cutting conditions. Dornfeld et al. [30] first showed the potential of AE in metal turning by proposing a relationship between the AE generated and the cutting conditions. Some of the early studies on AE generated in machining processes were aimed at understanding the relation of AE with different cutting related phenomena. Jiaa et al. [56] discussed the potential of AE in monitoring friction and wear in metal cutting. Rangwala et al. [42], [57] studied the frequencies and energies associated with the AE generated in metal turning and noticed a strong dependency on the cutting conditions like velocity and feed rate. Section 2.3 discusses the different machining related studies in the context of AE monitoring.

Concerning additive manufacturing processes like 3D printing, Hakiai et al. [58] demonstrated that droplet ejection and landing events can be monitored by AE signal during inkjet printing. While not directly related to AE, acoustic-based monitoring approaches have also been applied to 3D printing involving different types of inks. For instance, Voltaire [59] demonstrated that in printing processes sound emissions from the printing press nip can be used to monitor phenomena like ink film splitting. Acoustic-based monitoring will be further explored in Section

2.5 while addressing hydrophone signal applications.

**Table 2.2: Acoustic emission monitoring in (a) traditional, and (b) non-traditional manufacturing processes [3].**

(a)

Process	Basic deformation mechanism	Acoustic emission related		Possible to detect by AE		AE mechanisms
		Process sources	Zones of deformation	Process changes	Product defects	
Press shearing	Cutting and shearing (non-steady)	Plastic deformation indentation Shearing Fracture Rubbing between blade, part and die	Narrow shear zone	Blade wear Incorrect blade/die clearance	Edge cracks Burr	Fracture Deformation
Piercing and blanking	Cutting and shearing (non-steady)	Plastic deformation indentation Shearing Fracture Rubbing between blade, part and die	Narrow shear zone	Punch and die wear Misalignment	Edge cracks Irregularities from improper clearance Martensitic lines	Fracture Deformation/fracture Metallurgical phase trans.
Machining	Cutting and shearing (steady and non-steady)	Plastic deformation in shear zone Chip/tool friction Chip fracture Chip tangling Tool/work friction Tool fracture	Narrow shear zone Contact zones	Tool fracture Tool wear Lubrication failure Chip form Chatter	Burr Surface finish Dimensional variation	Deformation
Grinding	Cutting and ploughing (steady and non-steady)	Plastic deformation in wheel/work contact zone Grit fracture Contact/sparkout	Wheel/work Contact zone	Wheel wear Contact/sparkout Lubrication failure Chatter Burning	Surface finish Dimensional variation	Deformation

(b)

Process	Basic process energy sources	Acoustic emission related process sources	Possible to detect by AE		
			Process changes	Product defects	AE mechanism
Welding	Electric arc Resistance Plasma Laser Electron beam	Arc/arc variation Metallurgical phase changes Cracking Deformation due to thermal distortion	Arc stability	Inclusions	Fracture
			Shielding gas effectiveness Metal transfer Arc on/off	Cracking Distortion	Deformation
Injection moulding	Material viscosity and flow Friction	Machinery cycle noise Material/die friction	Incomplete mould filling		Friction
			Cycle irregularities		Mechanical impact
Composite material fabrication	Fibre layup Thermal treatment	Fibre/resin fracture Material/die interaction	Cycle irregularities	Incomplete or non-uniform density	Fracture Friction
Casting	Phase change Thermal treatment	Phase change Metallurgical transformation Stresses on cooling	Incomplete mould filling	Internal crack	Fracture
			Cycle irregularities		

## **2.3 Acoustic Emission Applications in Machining**

In the 1990s, it was evident that AE techniques have tremendous potential in manufacturing operations in both machine diagnostics and process monitoring [3]. Since then, several studies have been conducted on AE monitoring of machining processes. This section will first discuss the literature related to experimental machining studies in macro and micro-scale cutting. Next, some AE machining models available in the literature will be discussed.

### **2.3.1 Machining Experiments: Macro and Micro-Scale Cutting**

AE is effective in detecting events associated with the orthogonal machining process like chip formation and tool wear. Barry et al. [60]–[62] investigated the different types of chips formed during the machining of Ti-6Al-4V alloy and hardened steel, and studied the corresponding AE generated. Cedergren et al. [63] investigated the microstructures in titanium alloy and how they affect the chip formation process and the AE generated during machining. Bhuiyan et al. [64] incorporated AE monitoring into understanding the effect of chip formation on the tool condition in metal turning. Arslan et al. [65] investigated the AE monitoring of tool wear and workpiece roughness in high-speed turning of steel.

In a particular study on AE monitoring of orthogonal cutting, Hase et al. [32] correlated the cutting phenomena with the AE generated in steel turning and studied the influence of chip formation and shear angles on the generated AE. The experimental investigation particularly dealt with the changing shear plane angle and the nature of the chip under different cutting conditions. As shown in Fig. 2.8(i), the sources (a)-(e) occur during normal operation and (f)-(h) occur in an abnormal state of operation [32]. The collected AE signal is affected by the nature of the chips

generated by the metal turning process. Fig. 2.8 (ii)&(iii) show the types of chips collected and the corresponding AE signals generated.

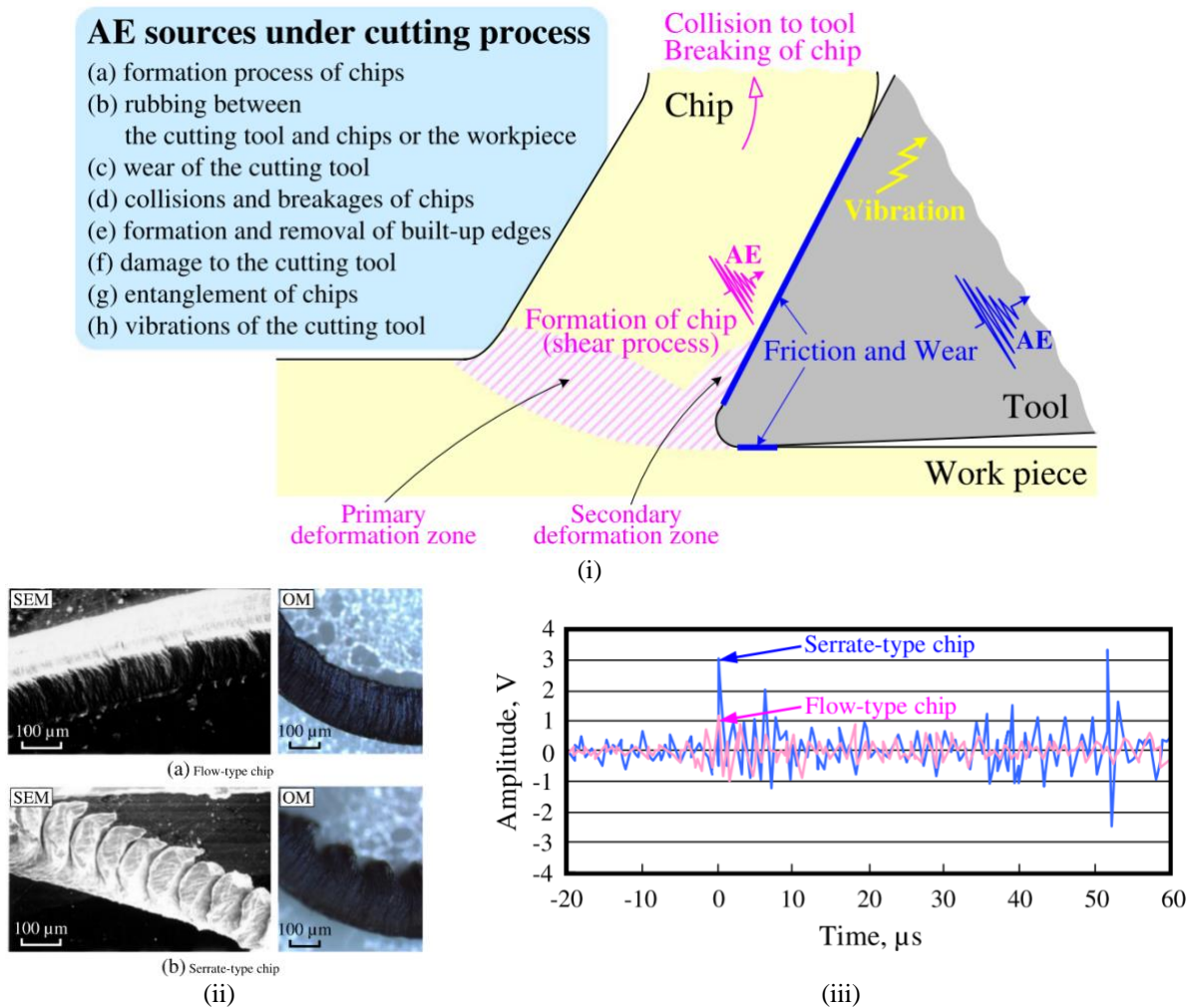


**Figure 2.8:** (i) Acoustic emission sources in orthogonal cutting, (ii) micrographs of flow-type and serrated chips collected, and (iii) acoustic emission signals corresponding to the chip types [32].

In 3D cutting processes such as milling, AE has been used as a sensing approach for monitoring tool conditions.  $AE_{rms}$  is the signal metric of choice in these studies as the AE signal is continuous. Xiqing and Chuangwen [46] used statistical analysis of the measured  $AE_{rms}$  to monitor tool wear in milling. In drilling, Gomez et al. [66] correlated the torques to the AE generated as a way for monitoring tool wear based on the dynamics of the cutting process. Besides  $AE_{rms}$ , they also studied other AE metrics – energy, counts, duration and amplitude. Zhong et al.

[67] proposed that the AE signal could be used as a substitute for the cutting forces in monitoring tool life and surface roughness during milling. Niknam et al. [68] demonstrated an approach to monitoring burr formation in milling operations based on the cutting force and AE signals. AE monitoring of the drilling process has also included composite, carbon-fiber reinforced plastic specimens where the AE signal has been shown to be strongly correlated to the tool wear [69].

In micro-scale cutting, Lee et al. [70] investigated the AE sensitivity to grain orientations and grain boundaries in diamond machining of high-conductivity copper. This study proved that the AE could be used to study the influence of the microstructures of material on the cutting process. Camara et al. [71] studied size effects in micro-milling of different metals and alloys proved the AE was effective in monitoring the ploughing and cutting phenomena in micro-milling.

Another application of AE in machining is tool touch-off detection. Oluwajobi et al. [72] investigated the material removal mechanisms at the nano-scale using molecular dynamics in machining using a diamond tool and discovered that the AE signal was effective in monitoring tool-workpiece interaction.

Micro-scale cutting processes, like grinding studies involving scratch tests, have also benefitted from AE monitoring. Sanchez et al. [73] showed AE is effective in detecting the damages in ceramics under different scratch conditions like load and velocity, specifically the accumulation of damages like microcracks along grain boundaries. Torres et al. [74] investigated the effect of ploughing, cutting, and friction phenomena on the AE during a single-grit scratch test. Perfilyev et al. [40] studied AE dependence on plastic deformation and damage in brittle and ductile metals in scratching.

Specifically related to grinding studies, Griffin et al. [35], [75], [76] have applied neural network analysis to the AE generated in scratch tests, to effectively monitor the cutting

phenomena. Their experimental work on single-grit scratch testing has revealed the potential of precision control through AE. Based on the frequency analysis of the generated AE, phenomena like frictional rubbing, ploughing, and cutting can be traced at submicron levels of depth of cut [35]. Fig. 2.9 shows a schematic of the experiment setup as well as a typical spectrogram from multiple scratches showing changes in the frequency contents in the different scratches.

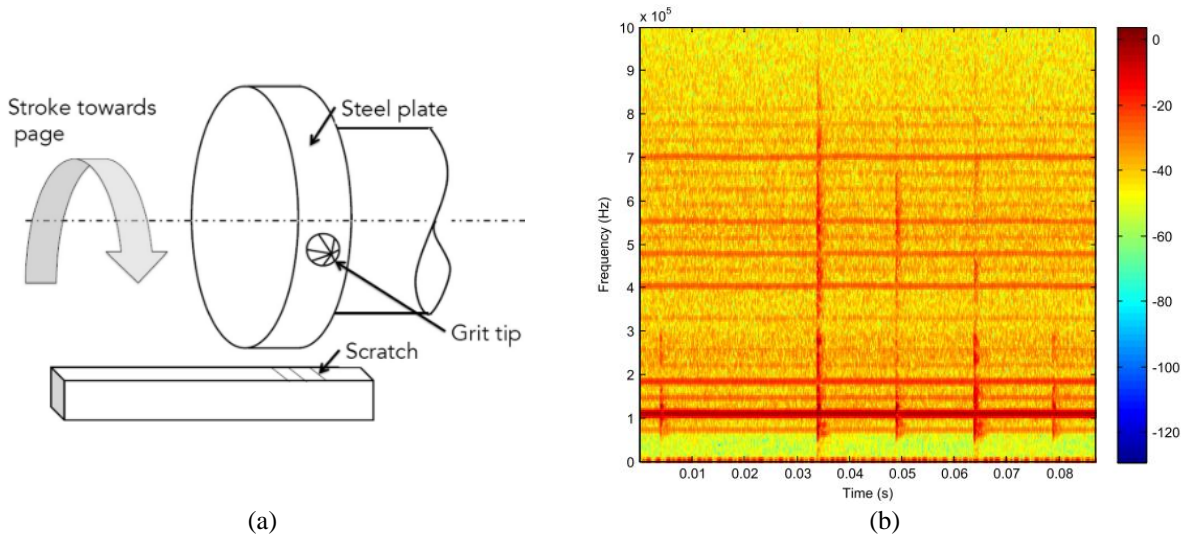


**Figure 2.9:** (a) Schematic of the experiment setup, and (b) a spectrogram from multiple scratches [35].

To benefit from the past studies on AE monitoring of machining processes and plan a new machining study, it is also important to understand the rationale behind the factors like the placement of the AE sensor and the suitable signal metrics to derive from the AE. The following section will address these points in light of the reviewed literature.

### *2.3.1.1 Acoustic Emission Sensor Placement in Machining*

The most common approach for the sensor placement in a machining experiment is on the cutting tool. As most sources of AE will be generated by the cutting phenomena like shear deformation, fracture, or friction, which lie near the cutting tool edge (see Fig. 2.8(i)), a sensor placed on the cutting tool allows for maintaining the relative distance between the AE source and the sensor. Besides, a cutting tool mounted AE sensor also allows for studying different types of

workpieces. As such, most orthogonal cutting or turning studies involve an AE sensor mounted on the cutting tool [32], [42], [43].

In certain machining processes, it is not suitable to attach the AE sensor to the cutting tool, e.g., in drilling or milling processes where the cutting tool is rotating. In such cases, the AE sensor is mounted on the workpiece [53], [77], but data interpretation is limited to AE frequency analysis as other metrics like amplitude or  $AE_{rms}$  cannot be used for comparative study as the relative distance between the AE source and the sensor could not be maintained, so the measured signal strength will be affected.

Fig 2.10(a) shows a photo of a typical experiment setup, involving the AE sensor, where the workpiece is rotating. Fig 2.10(b) shows a photo of an experiment setup where the cutting tool is rotating. The locations of the AE sensors are marked in these photos.

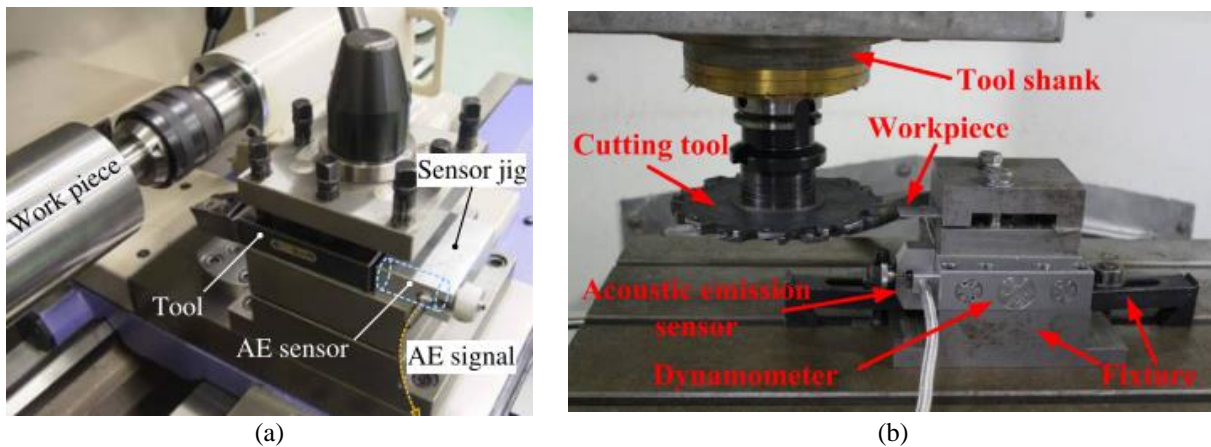


**Figure 2.10: Acoustic emission sensor mounted on - (a) cutting tool during turning (rotating workpiece) [32], and (b) workpiece during milling (rotating cutting tool) [77].**

### *2.3.1.2 Acoustic Emission Signal Metrics in Machining*

As discussed in Section 2.2.1, the AE signal could be either ‘burst’ type or continuous type. The nature of the signal is dictated by the sources generating the AE. In machining processes, under stable cutting conditions, the AE sources are related to the shear deformation in the workpiece, and the friction on the cutting tool surface [32]. As these cutting related phenomena

are continuous, the AE generated is not transient ‘burst’ type but continuous. This makes for a suitable case for AE energy analysis as it allows for the comparison of the AE energy with the cutting related energies.

Also,  $AE_{rms}$  has been the widely studied metric in most machining studies that incorporate a simple cutting process like orthogonal cutting [46], [66], [67], [32]. As mentioned earlier, machining studies involving milling, drilling, or other related processes usually rely on AE frequency analysis instead. The location of the AE sensor on the workpiece allows for understanding the different frequencies associated with cutting different regions of the workpiece [53].

In the context of this thesis, the metric ‘AE signal power’ is of particular interest. It is the  $(AE_{rms})^2$  of the signal and it allows for understanding the different phenomena like shear deformation and friction during an orthogonal cutting, as the AE signal power could be assumed to be proportional to the power or work rate consumed in the cutting due to shear deformation or friction. Based on this relation, orthogonal machining studies employ AE signal power as the metric in developing AE prediction models [43]. The next section will describe such AE machining models.

### **2.3.2 Acoustic Emission Models in Machining**

This section will first describe the AE modeling in orthogonal cutting based on AE signal power. Next, other strategies for mechanistic and empirical models will be described with examples from literature.

#### *2.3.2.1 Acoustic Emission Signal Power Modeling in Orthogonal Cutting*

The seminal work of Dornfeld et al. [30] in AE monitoring of orthogonal cutting of metal

proposed an AE model based on the forces and velocities derived from the cutting force diagram of the Merchant's circle [78]. The model was based on the assumption that the AE signal power is proportional to the sum of powers or work rates from different deformation mechanisms accompanying the cutting – shear deformation along the shear plane, and friction on the cutting tool faces.

Fig. 2.11 shows the schematic of the cutting process in orthogonal machining, showing the different force and velocity components. Fig. 2.11(a) shows how the cutting forces are resolved onto a 2D framework, while cutting workpieces that are thin enough so that the thickness does not play an important factor in the resultant forces. Fig. 2.11(b) shows the force components along the shear plane. The shear deformation is the dominant mechanism in orthogonal machining and is defined by a shear plane, which in turn affects the chip formation mechanism. Fig. 2.11(c) shows the forces along a continuous chip that moves along the rake face of the cutting tool.

Building upon the work of Dornfeld et al. [30], Park [43] proposed multiple mathematical, analytical models for the AE based on different cutting process parameters. These models were also based on the identification of different primary deformation processes accompanying the cutting – plastic deformation in the shear plane, and friction and wear along the rake and flank faces of the cutting tool. The theoretical work rates in the different deformation zones were established by multiplying the corresponding force components and the velocity components in the deformation zones. This is shown in Eq. 2.1:

$$P_i = F_i * V_i, i = 1,2,3, \quad (2.1)$$

where  $F_i$  and  $V_i$  are the force and velocity components, respectively, for a deformation zone  $i$ , and  $P_i$  is the theoretical power or work rate.

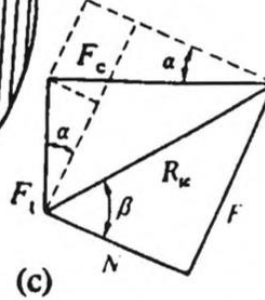
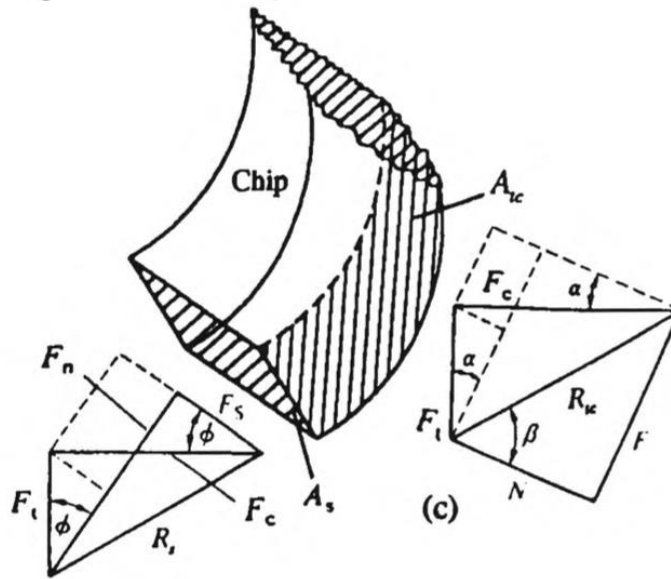
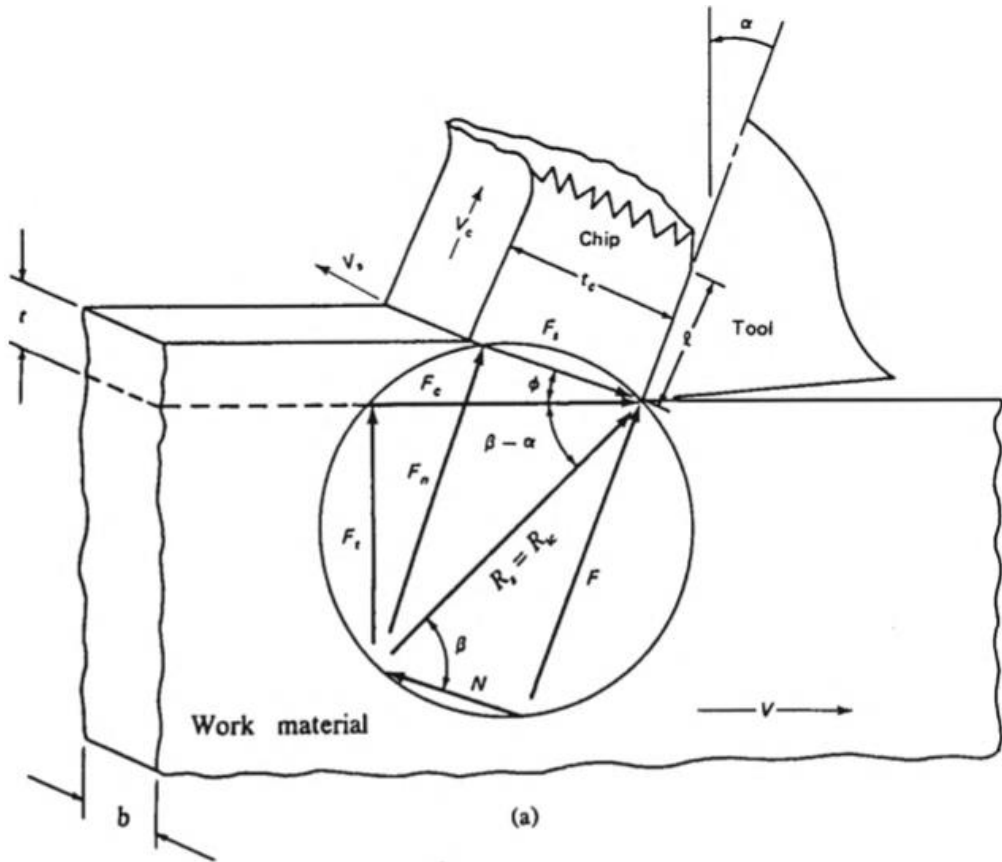


Figure 2.11: Machining geometry in orthogonal cutting – (a) cutting force diagram, (b) shear plane, and (c) tool face [43].

Using some proportionality and attenuation constants, these theoretical work rates were equated with the measured AE signal power ( $AE_{rms}$ )<sup>2</sup>. This is shown in Eq. 2.2:

$$AE_{rms} = C * (C_1 * P_1 + C_2 * P_2 + C_3 * P_3)^{\frac{1}{2}}, \quad (2.2)$$

where  $AE_{rms}$  is the measured AE signal root mean square, C is the proportionality constant, and  $C_1, C_2, C_3$  are the attenuation constants.

The proportionality constant allows for the conversion of the theoretical cutting power (or work rate) into the AE signal power. The unit of work rate is Watt, but the unit for AE signal power is Volt<sup>2</sup>. On the other hand, the attenuation constants are non-dimensional with a value between 0-1. The attenuation constant corresponding to a particular deformation zone is dependent on the transmission losses that are encountered as the dissipated energy transmits to the cutting tool, eventually contributing to the AE signal measured by the sensor attached to the cutting tool. For instance, the transmission losses in the deformation along the shear plane will be more than the transmission losses corresponding to friction on a tool face. As the shear plane is located a little farther from the cutting tool, the generated elastic waves attenuate as they travel the distance. On the other hand, the friction along the tool face will result in little attenuation as the source of AE lies near the cutting tool surface. Thus, both proportionality constant and the attenuation constants are unknown factors that need to be calibrated for a particular cutting setup.

Fig. 2.12(a) shows the schematic of the cutting tool in orthogonal machining, showing three deformation zones – the primary (along shear plane), secondary (friction and wear on rake face), and tertiary (friction and wear on flank face). Fig. 2.12(b) shows a plot of experimental and theoretical  $AE_{rms}$  for different cutting tools, showing a strong agreement.

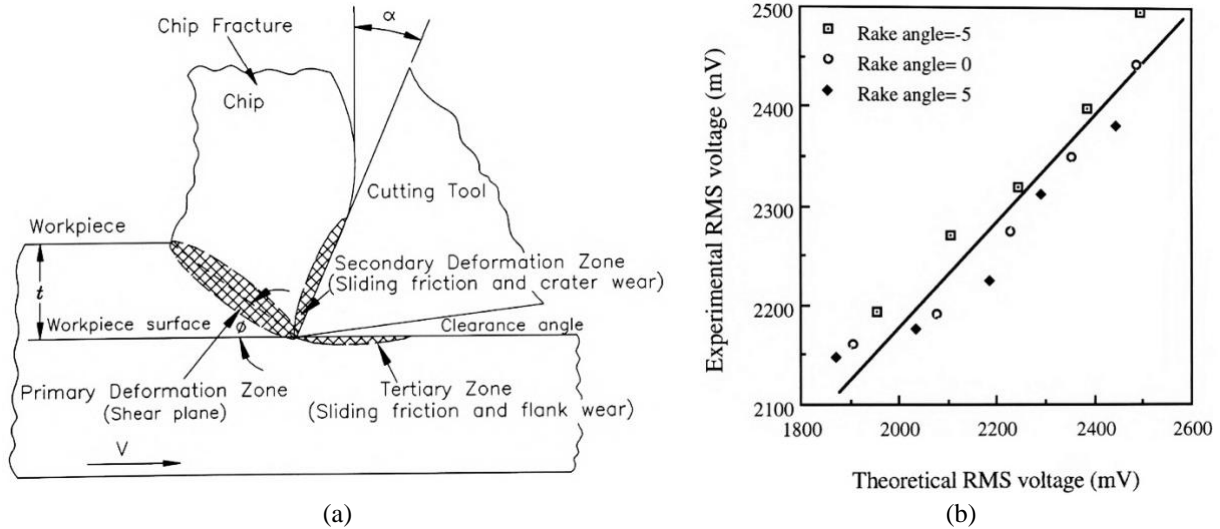


**Figure 2.12: (a) Cutting mechanisms contributing to acoustic emission generation in orthogonal machining, and (b) a plot of experimental vs. theoretical  $AE_{rms}$  showing good correlation [43].**

### 2.3.2.2 Other Acoustic Emission Modeling Strategies

In terms of mechanistic modeling, Bourne et al. [79] developed an AE-based technique to detect the tool-workpiece contact during micro-milling. The objective was to detect tool touch-off during micro-milling to determine the plane of operation based on contact points. The AE signal power  $(AE_{rms})^2$  was compared to the amount of material removed during the end-mill rotation. The material removal was estimated using a probability factor determined from the probability density functions of the workpiece surface roughness and the location of the cutting tool edge from the mean workpiece surface. Fig. 2.13 shows the experimental AE bursts from tool touch-off along with the AE prediction from the mechanistic model. An experimentally determined threshold allowed for detecting the tool touch-off.

Empirical, regression-based AE models are also available in the literature. In a particular study involving the AE generated in milling, Gaja [31] explored the application of AE to monitor the depth of cut in the milling process. The depth of cut was predicted from a function that included the measured  $AE_{rms}$ , as well as the cutting conditions like spindle speed, feed rate, and tool status. Separately,  $(AE_{rms})^2$  was also predicted based on the cutting conditions. Experimental slot milling

tests were conducted to test the prediction accuracy. Fig. 2.14(a) shows the plot of the predicted depth of cut along with the measured depth of cut, showing good correlation, for a geometry shown in Fig. 2.14 (b).

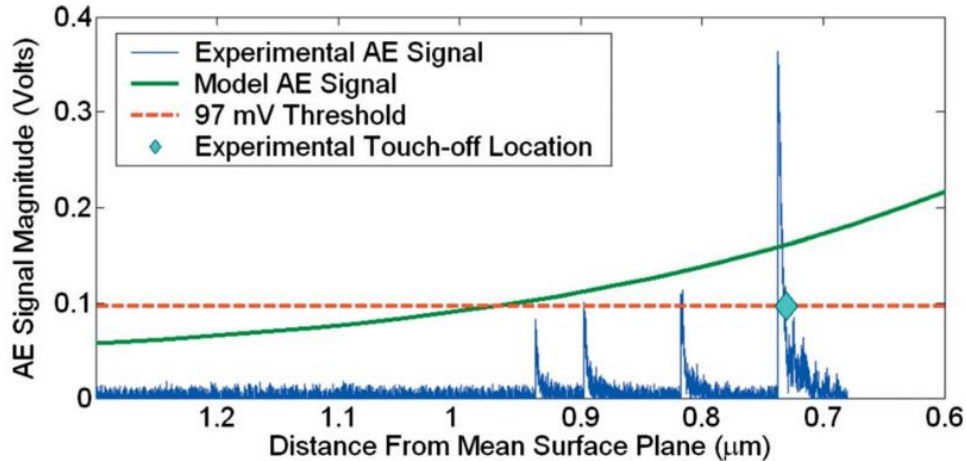


Figure 2.13: Plot of model and experimental acoustic emission for tool touch-off detection [79].

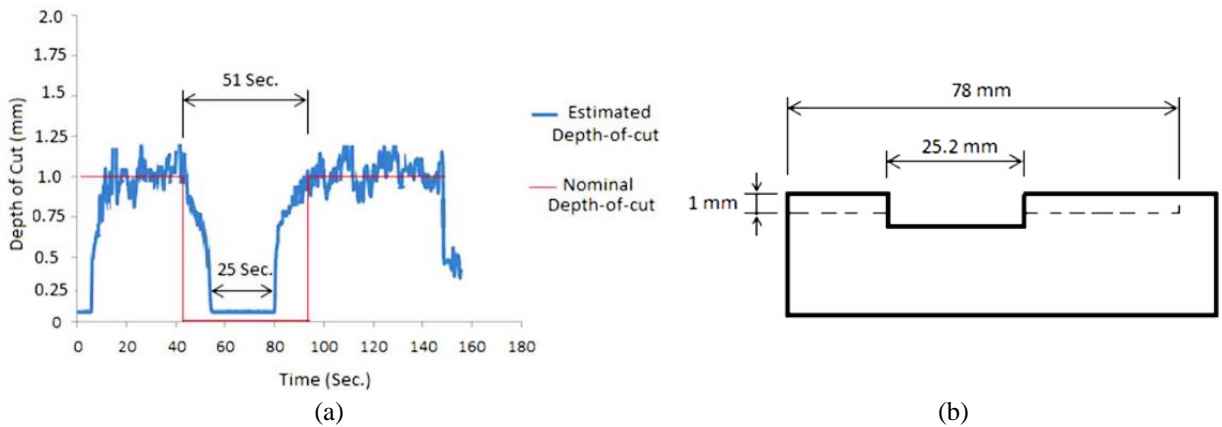


Figure 2.14: (a) Plot of the calculated and the estimated depth of cut, and (b) the corresponding geometry of the milled specimen [31].

## 2.4 Acoustic Emission Applications in Bone Characterization

While discussing AE applications in bone characterization, it is necessary to understand the context of different AE applications in material testing and characterization. The nature of the AE allows us to get insight into phenomena occurring inside a specimen by external application of forces and stresses. Such analysis also helps in studying the responses of the materials in manufacturing processes.

AE has proven to be highly effective in the characterization of composite materials, particularly relating to the fracture process. As mentioned in Section 2.2.1, amplitude and frequency analysis of the AE signal have been used to characterize the different fracture-based failure mechanisms in composite specimens in fatigue testing or tensile testing [33], [52], [80]. For instance, AE monitoring has also been widely applied in understanding the fracture behaviors of different concretes [81]–[84]. These studies reveal a strong relationship between the concrete fracture energy and the AE energy. In addition to AE energy, metrics like AE hits or counts could be used to effectively monitor crack evolution, and accumulation of microcracks in concrete and reinforced concrete specimens under different loading conditions [85]–[87].

As bone is also a composite material, it benefits from the different AE monitoring techniques. There have been many studies on material testing and characterization involving different bones [39], [88], [97], [98], [89]–[96]. The bone specimens have been studied in tension [88], [90], [91], torsion [91], [95], bending [39], [95]–[97], [99], and cyclic loading [89].

In a particular bone fracture-toughness study, Akkus et al. [90] conducted tests on specimens made from the human femoral cortical bone. The specimens were harvested along both longitudinal and transverse directions to the osteonal orientation. The AE signal collected during the fracture tests was discrete, consisting of separate bursts or waveforms which were associated with the cracks and micro-cracks in the bone specimens. Using data-clustering techniques it was observed that the AE hits (bursts or waveforms) and energies fell into three clusters which corresponded to the main crack propagation, microcracks, and diffuse damage. Fig. 2.15(a) shows the micrograph of a longitudinal specimen, showing evidence of cracks. Fig. 2.15(b)&(c) show the plots associated with the AE amplitudes and hits.

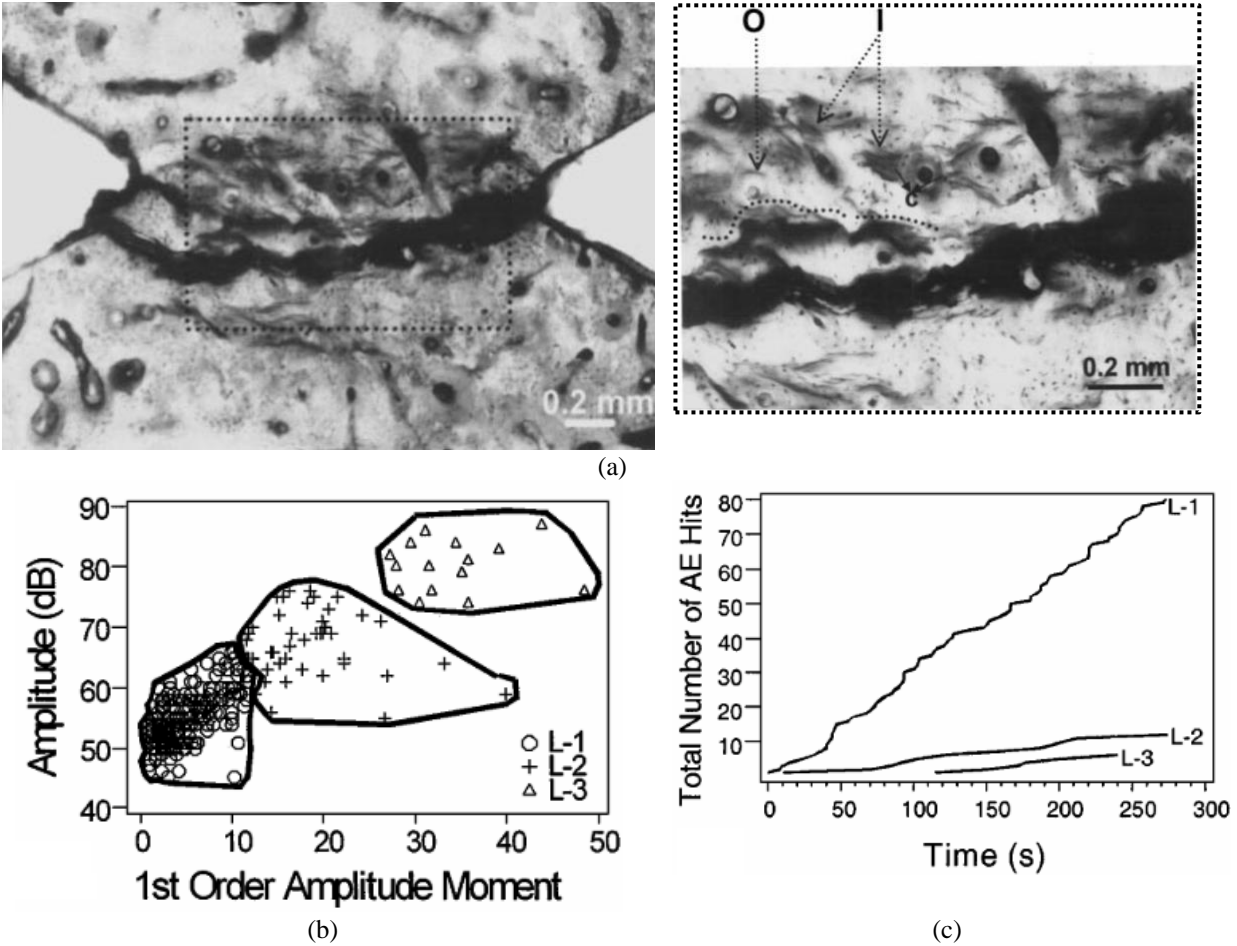


**Figure 2.15: (a) Micrograph of a longitudinal specimen showing cracks along the microstructures – O-osteon, I-interstitial matrix, and c-cement line, (b) three clusters observed in acoustic emission amplitudes, and (c) total number of acoustic emission hits corresponding to the three clusters [90].**

A logical step in the AE monitoring of deformations and fractures in material testing studies is the translation into AE monitoring of these sources in machining applications. While machining studies on biological materials like bone are not uncommon [4], [5], [13], [20], [21], [100], AE-based monitoring is rare. Liao et al. [53] have recently explored AE application in bone micro-drilling. Their experimental investigation into chip formation mechanisms at different penetration depths in bone micro-drilling involved frequency analysis of the AE signal from a sensor mounted on the bone workpiece. A wavelet energy-based method revealed different dominant frequencies in the AE signal at different penetration depths corresponding to changing

material properties at those penetration depths. Fig. 2.16 shows the plots of the wavelet energy ratios in different frequency bands as the drill cuts through different regions in the bovine bone.

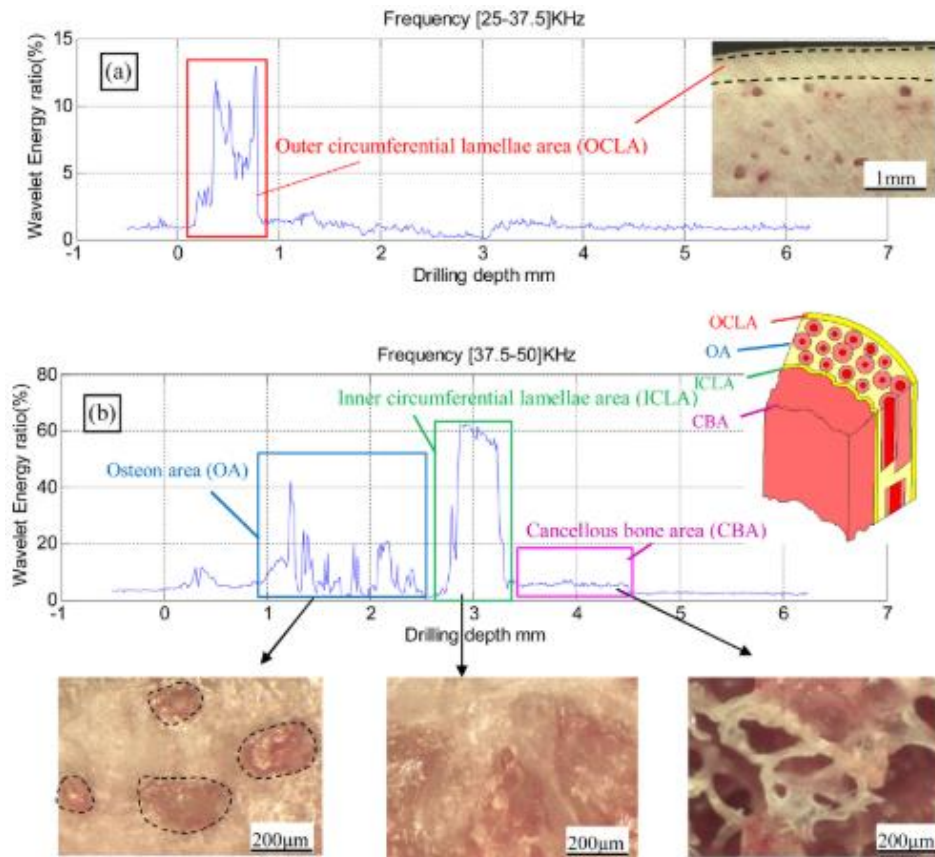


**Figure 2.16: Wavelet energy ratio of the acoustic emission signal during bone micro-drilling [53].**

Another study concerning AE application in bone drilling involved a novel frequency-based analysis to detect the transition between the hard cortical bone and the soft cancellous bone during drilling [98]. Like Liao et al. [53], this study also discovered the dominant frequency ranges are different in the cortical and cancellous regions of the bone.

## 2.5 Hydrophone Signal: Background and General Applications

Hydrophone sensors are used to study sound in different underwater applications. The measurement capabilities of piezoelectric hydrophones include a wide range of acoustic pressures and frequencies [101].

Hydrophone applications in fluids extend to media like tissues and gels often, involving high ultrasonic frequencies [102], [103]. It is beneficial to study the general applications of the hydrophone sensor to design experiments based around it. The versatility of hydrophones is demonstrated in the study involving droplet impacts on a fluid. Chashechkin and Prokhorov [104]–[107] have conducted many studies involving droplet impact on water surfaces, where they employ a hydrophone to monitor the hydrodynamics and the acoustic response in the fluid. The nature of the hydrophone signal, which has a pressure unit such as Pascal, becomes clear when looking at an example from Chashechkin et al. [105]. Fig. 2.17 shows the hydrophone signal corresponding to a droplet impact that results in two high-frequency sound packets. In this particular hydrophone signal the peak I is from the impact pulse, and the peaks II and III are the high-frequency sound packets corresponding to the formation of air cavities in the water caused by the droplet impact. The frequency spectra ‘b’ and ‘c’ correspond to the signals ‘a’ and ‘d’, respectively. ‘a’ and ‘d’ are signals around the vicinity of the peaks II and III, respectively.

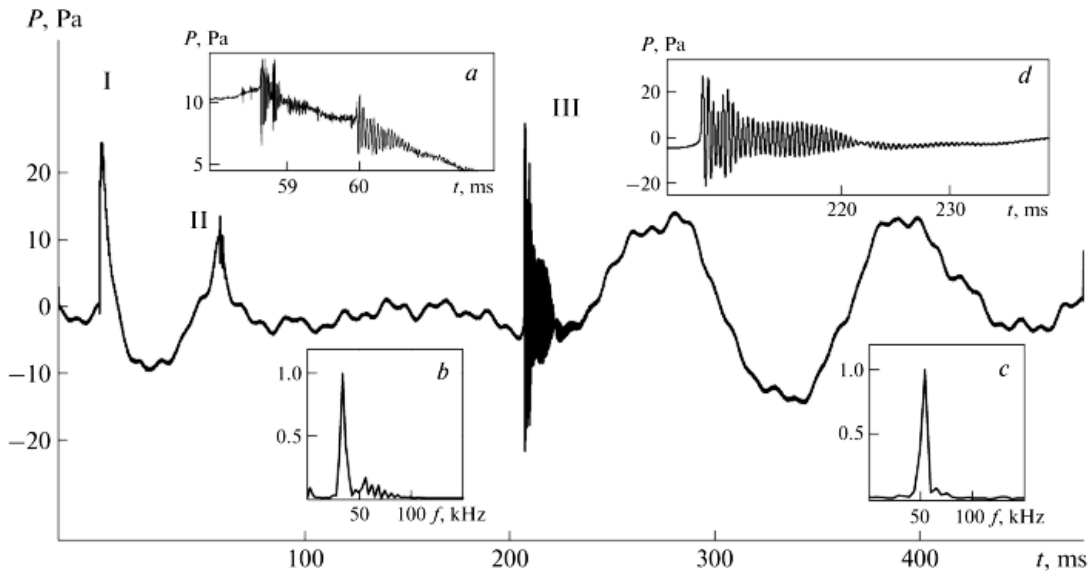


**Figure 2.17: Hydrophone signal from a water drop impact [105].**

Other studies on droplet impacts also use hydrophones to monitor the high-frequency pressure waves which are characterized as acoustic emission [108], [109]. Fig. 2.18 shows the

results from a droplet-impact study by Frommhold et al. [108], where the frequency analysis of the hydrophone signal allowed for monitoring the bubble formation that accompanied a droplet impact.

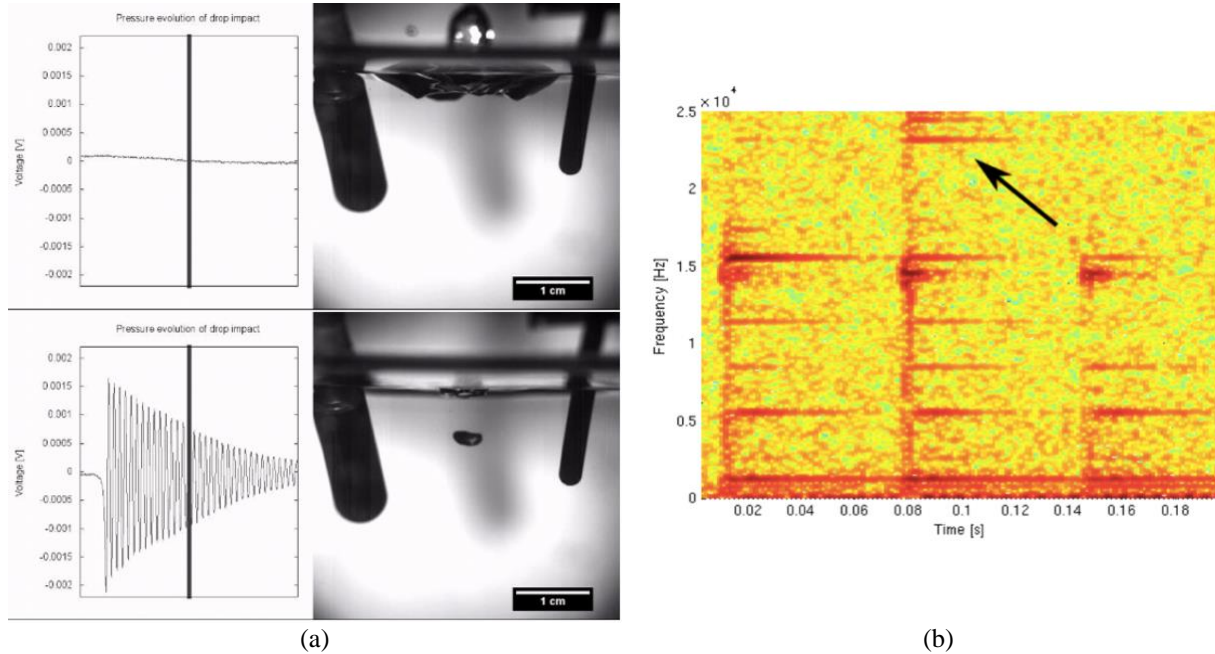
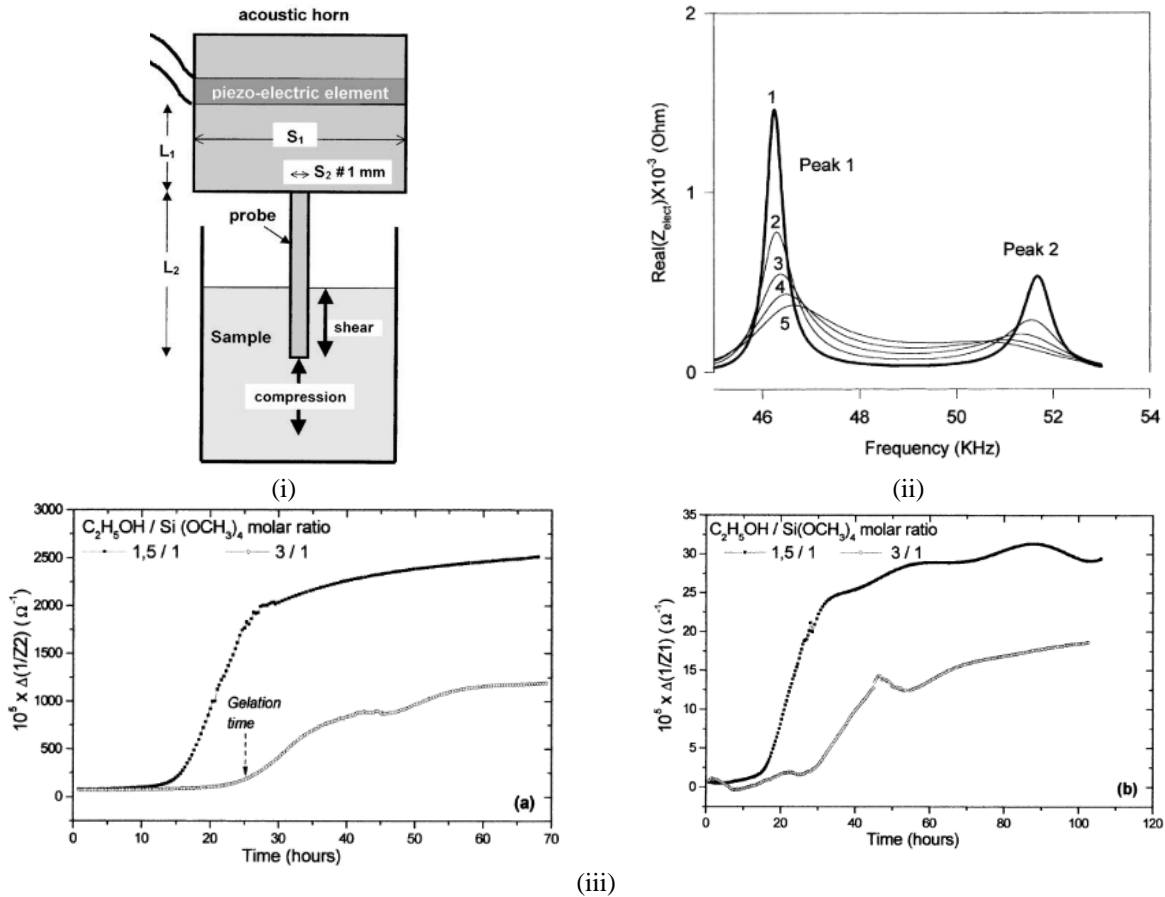


**Figure 2.18: (a) Hydrophone signal evolution and the video stills corresponding to a droplet splash (top), and bubble formation (bottom), and (b) spectrogram from a droplet study with the high-frequency component corresponding to the bubble resonance [108].**

## 2.6 Acoustic-based Characterization of Hydrogels

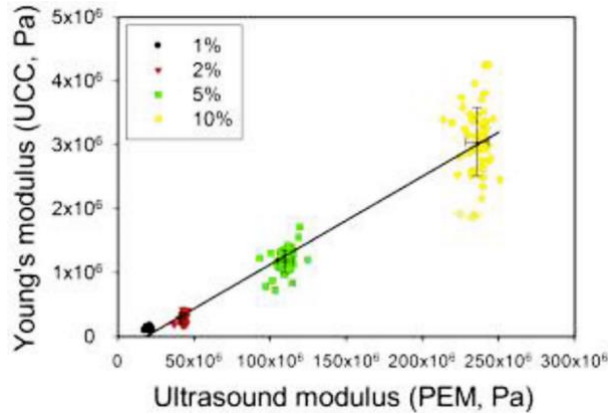
The hydrogel belongs to a class of materials that undergo the sol-gel (solution to gel) transition. For understanding the acoustic characterization of the hydrogel, it is beneficial to visit acoustic-based monitoring approaches to testing and characterization for materials that undergo the gelation process [110]. A most common method involves acoustic spectroscopy, typically in the ultrasonic range [111]–[116]. In a particular study on sol-gel monitoring, Cros et al. [115] proposed an approach to monitor gelation in silica gels by using the resonance of an acoustic horn. The study involved a metric derived from the load response at the two resonance frequencies in the experiment. This metric effectively allows for monitoring the gelation process in silica gels.

Fig. 2.19(i) shows a schematic of the experiment involving acoustic horn. Fig. 2.19(ii) shows the resonance curves altering with loads. Fig. 2.19(iii) shows the gelation curves for the two resonance frequencies ((a), (b)).



**Figure 2.19: (i) Ultrasound horn operation, (ii) a metric determined by the load response, showing peaks around the two resonance frequencies, and (iii) gelation curves for two solvent amounts, obtained at peak-1(a) and peak-2 (b) [115].**

There have been studies involving acoustic monitoring of tissues and hydrogels [6], [117]–[122]. The acoustic approach provides an alternative to mechanical characterization. For instance, Walker et al. [117] characterized hydrogels at different concentrations and described an approach for estimating the gel stiffness from the ultrasound. This ultrasound modulus was found to compare well with the young’s modulus of the hydrogel (Fig. 2.20).



**Figure 2.20: Comparison of young's modulus against the ultrasound modulus for different hydrogel concentrations [117].**

Exploring hydrogel characterization using a hydrophone, a study conducted by Anderson et al. [103] demonstrated the effectiveness of the hydrophone even in extreme conditions. Anderson et al. [103] characterized a hydrogel sample using shockwaves that were monitored by high-speed imaging and a hydrophone. Fig. 2.21(a) shows the cartoon showing the changing locations of the hydrophone tip in the hydrogel medium (G). Also shown are the support platform and the aluminum disk (A) which imparts the shock waves through the hydrogel medium. Fig. 2.21(b) shows the pressure measurements from the hydrophone at different locations, providing insight into the nature of shock wave propagation through the medium. The application of hydrophone allowed for finding the pressure and density associated with the shockwaves.

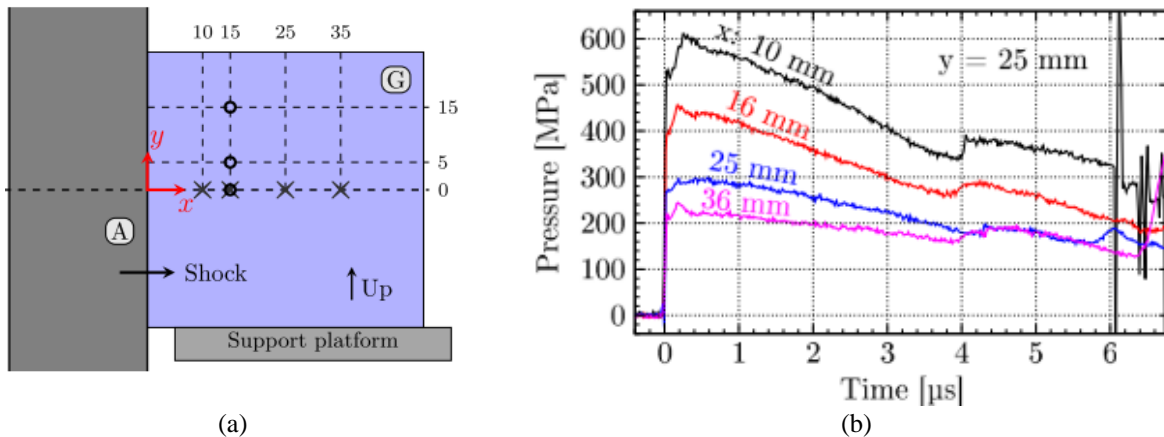


**Figure 2.21: (a) Cartoon of the experiment setup showing the locations of the hydrophone inside the gel medium, and (b) shock profiles determined by the hydrophone at different locations [103].**

## 2.7 Gaps in Knowledge

In light of the review of the current state of literature, the following specific gaps in knowledge have been identified in relation to the effectiveness of using acoustic sensing modalities to monitor the bone cutting and hydrogel gelation processes:

1. There are many studies on AE-based characterization of bone that investigate the generation of cracks under different loading conditions. However, microstructure-specific, AE-based process monitoring has not been attempted in bone machining. More specifically, such a monitoring has not been implemented for fracture-based cutting of bovine bone.
2. There have been many implementations of AE models for orthogonal machining, however such models have not been applied to bone machining. In particular, modeling of the AE signal power in bone sawing, which is also a shear-based cutting process, has not been attempted.
3. While studies on acoustic-based monitoring and characterization of gels, including tissue-mimicking hydrogels exist in literature, they all involve high, ultrasonic frequencies that cannot be economically implemented in a bioprinting platform. There is a lack of studies investigating acoustic-based monitoring of gelation of hydrogels in environments compatible with bioprinting applications.

The research efforts described in Chapters 3-6 are aimed to specifically address these gaps in knowledge.

### **3. ACOUSTIC EMISSION ANALYSIS OF FAILURE MECHANISMS ENCOUNTERED IN FRACTURE-CUTTING OF BOVINE BONE**

This chapter deals with research Thrust 1 involving fracture-dominant cutting of the bovine cortical bone. For this study, orthogonal cuts were made on haversian and plexiform bone specimens at 70  $\mu\text{m}$  depth of cut, to induce different failure modes. This depth of cut was chosen as it has been shown to result in fracture-dominated cutting [20]. Cutting force and AE signals were collected and related to specific failure modes identified using high-speed camera images and microscopy techniques. Relating AE signatures to different bone failure mechanisms is intended to help in in-situ acoustic monitoring of damage during bone surgeries.

The remainder of this chapter is divided into the following sections: Section 3.1 describes the microstructures in the bovine cortical bone. Section 3.2 presents the orthogonal machining tests conducted in this study. Section 3.3 discusses the failure mechanisms encountered and their AE responses. Section 3.4 presents a discussion of the AE and cutting energies. Finally, Section 3.5 presents the conclusions that can be derived from this work.

#### **3.1 Bone Microstructure**

As mentioned in Chapter 2 (Literature Review), bovine cortical bone consists of haversian and plexiform regions which are easily distinguishable by their microstructures. Haversian bone comprises cylindrical osteons embedded in the interstitial matrix. Osteons consist of concentric lamellae surrounding haversian canals. In aged bone, the osteons are called secondary osteons which are surrounded by an interface of cement line [5]. In terms of mechanical properties, the interstitial matrix has a slightly higher elastic modulus and hardness than the osteon, while the cement line has lower modulus and hardness than both the osteon and the interstitial matrix [4].

### 3.2 Machining Experiment

A 30-month-old bovine femur bone was used in this study. The femur bone was cut and sectioned using a Mar-Med™ bone saw under constant water irrigation, and specimens of size 10mm X 10mm X 10mm, approximately, were obtained. 4 specimens of haversian bone and 8 specimens of plexiform bone were prepared. For storage, the specimens were covered with phosphate-buffered saline (PBS)-soaked gauze and frozen at -20°C. Before the orthogonal cutting experiments were conducted, frozen bone specimens were thawed and placed in a saline solution to retain the moisture content. The haversian and plexiform components of the bone were easily identified by their distinguishable microstructures.

The experiments were conducted on a three-axis hybrid micro-machining center (Mikrotool™ DT-110, Singapore). A Kistler 9256C1 dynamometer was attached to the stationary tool mount attached to the Y stage [123]. The workpiece holder was attached to the X-Z stage of the micro-machining center. Nano-30 AE sensor (Physical Acoustics Inc.), with response frequency 150 KHz - 750 KHz, was attached to the shank of the tool using a magnetic sensor mount. A Phantom v.7.3 high-speed camera was set up to record the cutting process. Fig. 3.1 shows the schematic of the experiment setup.

The orthogonal cutting experiments were conducted on the haversian and plexiform bone specimens. Plexiform bone specimens were cut in two directions - 0° and 90° to the woven/lamellar orientation - as they were expected to result in different failure modes to study. Thus, in the present study, the plexiform specimens will be called ‘Plexiform-0° bone’ and ‘Plexiform-90° bone’, depending on the cutting directions.

The cutting specimen width was  $500 \pm 100 \mu\text{m}$ . The tungsten carbide cutting tool had 1  $\mu\text{m}$  edge radius, 10° clearance angle, and 20° rake angle. The cutting edge of the tool was 7 mm,

considerably larger than the specimen width. This allows for conducting multiple cutting experiments without accumulating the effects of tool wear. The cutting experiments were conducted at depth of cut of  $70\ \mu\text{m}$ , and a constant feed rate of  $800\ \text{mm/min}$ . For each experimental condition, four replicate experiments were conducted. Data acquisition cards (National Instruments) were used to collect the force signal at a sampling rate of  $30\ \text{KHz}$  and the AE signal at a sampling rate of  $4\ \text{MHz}$ . The high-speed camera images were collected at  $4000$  frames per second. Table 3.1 shows the cutting conditions used in this study.

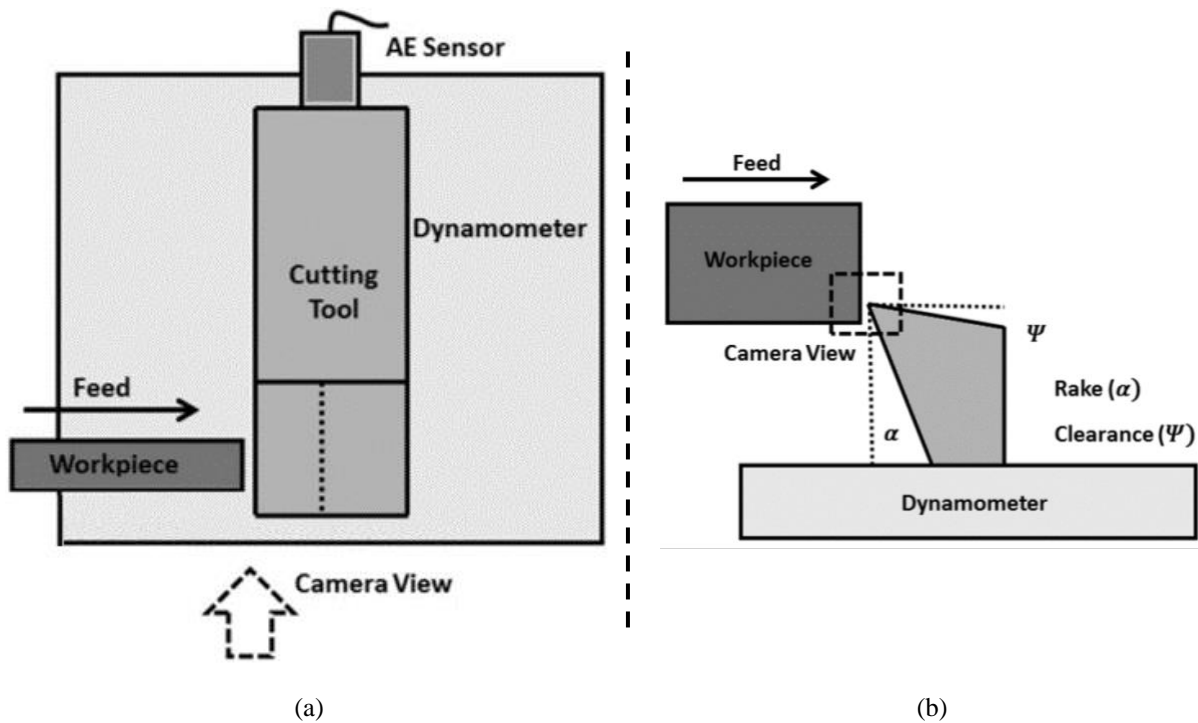


Figure 3.1: Cartoon of the orthogonal cutting experiment setup (not to scale) - (a) top view, and (b) front view.

It should be noted that the AE sensor was attached to the shank of the tool, opposite the cutting side (Fig. 3.1). The failure mechanisms in the workpiece during the cutting process will result in cutting force fluctuations experienced by the tool. This is expected to result in elastic deformations in the cutting tool that will generate the AE measured by the sensor attached to the tool.

**Table 3.1: Machining conditions.**

<b>Workpiece</b>	<ul style="list-style-type: none"><li>• Haversian bone</li><li>• Plexiform 0° bone (plexiform bone machined at 0° to lamellar orientation)</li><li>• Plexiform 90° bone (plexiform bone machined at 90° to lamellar orientation)</li><li>• Specimen thickness (<math>500 \pm 100 \mu\text{m}</math>)</li></ul>
<b>Tool</b>	<ul style="list-style-type: none"><li>• High-precision ground tungsten carbide</li><li>• <math>1 \mu\text{m}</math> edge radius</li><li>• 10° clearance angle</li><li>• 20° rake angle</li></ul>
<b>Cutting Speed</b>	<ul style="list-style-type: none"><li>• 800 mm/min</li></ul>
<b>Depth of Cut</b>	<ul style="list-style-type: none"><li>• <math>70 \mu\text{m}</math></li></ul>

### 3.3 Experimental Findings

As mentioned earlier, the depth of cut of  $70 \mu\text{m}$  was chosen, based on previous studies that have shown that at depths of cut  $\geq 70 \mu\text{m}$  the cutting mechanism is fracture-based [20].

Four cuts were made for each cutting condition (haversian, plexiform-0°, and plexiform-90°). This allowed for observing multiple instances of the failure modes in the different bone specimens. The use of force and AE signals, along with high-speed camera images and post-cut microscopy, allowed for a clear understanding of different failure mechanisms encountered during orthogonal cutting of the bone specimens.

Fig. 3.2 shows the force and AE signals of the failures in a haversian bone specimen. It could be seen that the ‘drops’ in the force signal corresponded with the ‘bursts’ in the AE signal. It can be deduced that force and AE signals provide complementary information regarding a failure process. Force signal contained information about the cutting force and energy that lead up to a failure or crack, while the AE signal provided information about the nature of the crack generated. It is also worth noting that thrust force is considerably lower than the cutting force, implying the external work is generally imparted in the cutting direction during machining.

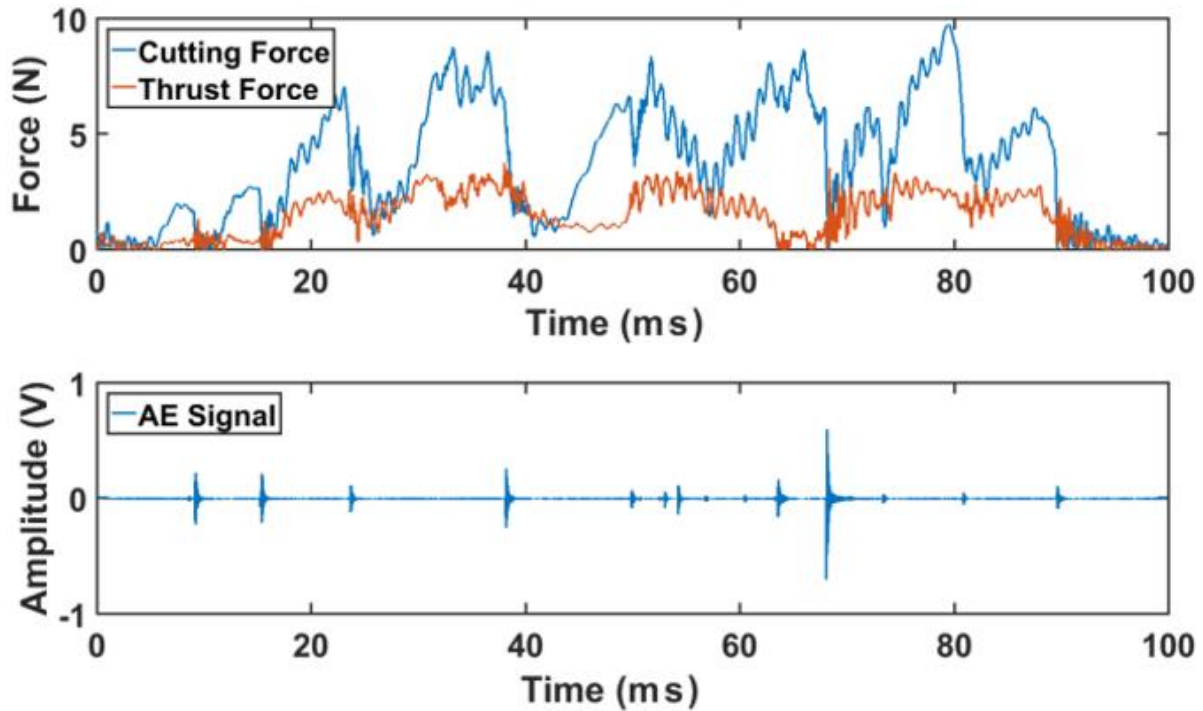


**Figure 3.2: Force and acoustic emission signals from haversian bone machining.**

Certain dominant failure mechanisms were observed in the three bone types (Fig. 3.3). In haversian bone, the common failure mechanisms were fractures in osteon, cement line, and interstitial matrix fracture. In the case of plexiform bone, the dominant failure mechanisms were lamellar and woven fractures. In the specific case of plexiform-90°, transverse lamellar failure was observed, that often propagated through multiple woven/lamellar regions in the cutting direction.

In the following sections, these failure mechanisms are discussed in detail. Fig. 3.4 & Fig. 3.5 show the typical fracture-induced failure mechanisms observed in the haversian and plexiform specimens, respectively, along with the typical AE signals collected. The red arrows in the post-cut microscopy images correspond to positions of the crack-tip at the instances of the bursts (marked by red circles) in the AE signals. These bursts in the AE signals correspond to the video frames from the high-speed camera which was focussed on the cutting tool during the cutting process.

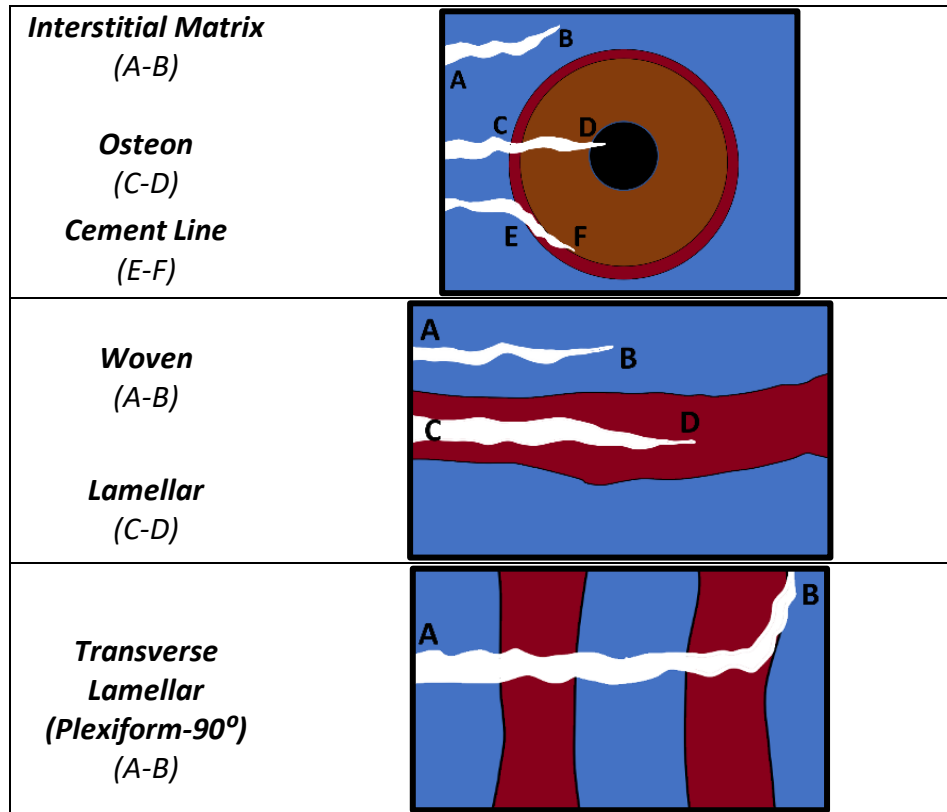


**Figure 3.3: Cartoons of failure mechanisms observed in the experiments. [Note: Haversian bone is shown as osteons embedded in the interstitial matrix, and plexiform bone is shown as alternating layers of lamellar and woven regions]**

### 3.3.1 Failure Mechanisms in Haversian Bone

Most of the volume in the haversian bone is occupied by osteons. As such, the dominant failure mechanisms observed involved the osteon and the cement line around the osteon. Osteon fracture occurred by the tool cutting through the cement line, engaging with the circumferential lamellae, and initiating a crack through the concentric lamellae in the cutting direction. On the other hand, cement line fracture occurred by rapid crack propagation along the cement line initiated by the tooltip

Damage Mechanisms in Haversian Specimens			
	Post-cut Microscopy (Scale = 150 $\mu\text{m}$ )	AE Signal	Video Frames of Damage Progression (Scale = 150 $\mu\text{m}$ )
(a)			
(b)			
(c)			

Figure 3.4: Dominant failure mechanisms observed in the haversian specimens.

Damage Mechanisms in Plexiform-0° and Plexiform-90° Specimens			
	Post-cut Microscopy (Scale = 150 μm)	AE Signal	Video Frames of Damage Progression (Scale = 150 μm)
(a)			
(b)			
(c)			

Figure 3.5: Dominant failure mechanisms observed in the plexiform specimens.

Post-cut microscopy images, AE signals, and high-speed camera images corresponding to cement line and osteon failures are shown in Fig. 3.4(a)&(b), respectively. Cement line fracture (Fig. 3.4(a)) mainly resulted in a single AE burst corresponding to the fracture in the cement line region surrounding the osteon. In osteon fracture (Fig. 3.4(b)), it was observed that a crack was initiated by the tooltip in the outer circumferential lamellae of an osteon, resulting in an AE burst. The crack then propagated through the lamellae, removing a part of the osteon and resulting in a bigger AE burst. Thus, 2 AE bursts were generally observed accompanying the osteon fracture. In some cases, based on the relative placement of the osteon to the cutting tool, the crack may propagate through the haversian canal. In such a case, it was seen that the AE signal would consist of 2 smaller bursts for fracture leading up to the haversian canal, and 1 bigger burst for fracture from the haversian canal to the outer lamellae resulting in the removal of a part of the osteon, thus, resulting in 3 AE bursts. While the haversian bone specimens mainly consisted of osteons, small regions of the interstitial matrix are also present, resulting in the observation of another failure mechanism, namely the interstitial matrix fracture (Fig. 3.4(c)). 1 or more AE bursts were observed in the case of interstitial matrix failure, with no particular trend in the relative sizes of the bursts. This is in contrast to the failure mechanisms in the osteon and cement line which exhibited very distinguishing features both in terms of the number of bursts and the relative sizes of the bursts. It is speculated that the isotropic nature of the interstitial matrix could be the reason for such a difference in the failure mechanisms and the resultant AE signature.

### **3.3.2 Failure Mechanisms in Plexiform-0° Bone**

Like the interstitial matrix in haversian bone, the woven region in plexiform bone could also be considered isotropic. As such, woven fracture (Fig. 3.5(a)) was also observed to result in 1 or more AE bursts with no particular trend in the burst amplitudes.

The dominant failure mechanism encountered in plexiform-0° bone was the lamellar fracture, where a large crack propagated ahead of the cutting tool in the planar lamellae and failed in bending. The AE signal was able to capture the crack initiation and propagation, and the final chip breakage. A typical lamellar fracture signal is shown in Fig. 3.5(b). The fracture was initiated by the tooltip in the lamellae, resulting in an AE burst. The fracture then propagated progressively through the lamellar region, ahead of the tool, resulting in multiple bursts and finally failed in bending, resulting in chip breakage accompanied by a final burst in AE. It was observed that most often, the intermediate AE bursts, i.e., AE accompanying the crack propagation phase, were larger than the AE burst due to crack initiation or the final chip breakage. As such, the AE signatures of lamellar fracture were observed to be very different from the woven fracture.

### **3.3.3 Failure Mechanisms in Plexiform-90° Bone**

Due to the orientation of the woven/lamellar layers transverse to the cutting direction, the fractures in plexiform-90° often propagated through both regions in a cut. The dominant failure mechanism is named trans-lamellar fracture where a crack generated in the woven or the lamellar region propagated through multiple woven/lamellar layers in the cutting direction, ahead of the tool.

Fig. 3.5(c) shows a typical trans-lamellar failure. It is seen that the fracture often results in 3 or more AE bursts corresponding to crack initiation and propagation and chip breakage. It is speculated that the number of bursts is related to the number of the woven/lamellar layers the crack propagates through.

### **3.3.4 Distinguishing Features in Acoustic Emission Signals**

Observing the AE signals corresponding to the different fracture-related failure

mechanisms, certain specific features in the AE signals could be readily identified. The categorization of features is very helpful, as evident from Fig. 3.4 & Fig. 3.5. Fig. 3.4(a)&(b) show the failure mechanisms related to osteon. Fig. 3.4(c) & Fig. 3.5(a) show the failure mechanisms in the interstitial matrix and woven regions, respectively, both of which are assumed to be isotropic. And finally, Fig. 3.5(b)&(c) show the dominant failure mechanisms in the plexiform bone that often result in larger crack areas and multiple AE bursts.

Building up from Fig. 3.4 & Fig. 3.5, a couple of metrics were used to characterize the 6 observed failure mechanisms in terms of their AE responses. Table 3.2 presents the distinguishable features observed in the AE signals accompanying these failure mechanisms.

**Table 3.2: Differentiating features in the Acoustic emission signals.**

		<b>Cement Line</b>	<b>Osteon</b>	<b>Interstitial Matrix</b>
<b>Haversian</b>	<b>No. of AE ‘bursts’</b>	<i>1</i>	<i>2-3</i>	$\geq 1$
	<b>Ratio of max/min amplitude</b>	<i>1</i>	<i>10-24</i>	<i>NA</i>
		<b>Woven</b>	<b>Lamellar</b>	<b>Trans- Lamellar</b>
<b>Plexiform</b>	<b>No. of AE ‘bursts’</b>	$\geq 1$	$\geq 4$	$\geq 3$
	<b>Ratio of max/min amplitude</b>	<i>NA</i>	<i>1-6</i>	<i>5-8</i>

In the previous sections, the typical AE signals of the different failure mechanisms were presented. These signals differed from each other in several ways. The most important difference was observed in the number of AE bursts in a signal. Cement line fracture (Fig. 3.4(a)) resulted in single bursts corresponding to the fracture of the cement-line. Osteon fracture (Fig. 3.4(b)) often resulted in 2-3 bursts. In the context of Table 3.2, the interstitial matrix (Fig. 3.4(c)) and woven (Fig. 3.5(a)) fractures did not exhibit specific patterns in terms of the nature of the AE bursts. On

the other hand, lamellar fracture (Fig. 3.5(b)) in plexiform-0° bone often resulted in more than 4 bursts as the fracture propagated ahead of the tool through the planar lamellar region before the chip breakage. In lamellar fracture, one of the intermediate bursts had the maximum amplitude. The trans-lamellar fracture (Fig. 3.5(c)) in plexiform-90° bone often resulted in more than 3 bursts as the fracture propagated through multiple woven/lamellar regions in the cutting direction. The final burst, which resulted from chip removal, often had the maximum amplitude.

The nature of AE signals in lamellar and trans-lamellar fractures could be attributed to the nature of crack propagation through the microstructures. In the lamellar region, the crack length is typically higher, and fracture energy release is dispersed over a longer path. The final fracture leading to chip removal does not necessarily result in the highest fracture energy release as it is easier for chips to be removed. This is unlike trans-lamellar fracture, where relatively smaller crack lengths were observed and the final fracture leading to chip removal typically resulted in high energy release to the resistance to crack propagation offered by the lamellar layers which are orthogonal to the crack path.

The difference in the relative sizes of the AE bursts allowed for quantifying the difference as a metric ‘Ratio of max/min amplitude’ as shown in Table 3.2. Osteon fracture resulted in very high ratios as the final burst that corresponded to breaking off and removal of osteon often had much higher amplitude than the prior bursts that corresponded to crack initiation and propagation. Lamellar fracture in the plexiform-0° bone had much lower ratios due to the nature of progressive crack propagation in the lamellar region leading up to chip breakage. Trans-lamellar fracture in plexiform-90° bone resulted in intermediate ratios as the final burst with the highest amplitude is not much higher than the prior bursts corresponding to the fracture propagating through the woven/lamellar layers.

### 3.4 Discussion

Based on the cutting force and AE signals collected on the different bone specimens, the identified failure mechanisms were further analyzed. After imposing a threshold of 1.5 mV to account for the noise in the signal, the start and end of the signal were identified and the AE signals corresponding to the failure mechanisms were isolated. As such, the signals obtained were of different lengths in time. Similarly, the corresponding force signals were also of different time lengths since, unlike the AE, the force signal also considers the rise in the force leading up to fracture.

After isolating the AE and the corresponding cutting force signals, acoustic and cutting energies were calculated. In orthogonal machining, the product of the average cutting force and the cutting speed is the external power consumed in the cutting process. For this study, the cutting force ( $F_c$ ) was integrated over the distance traversed by the tool during the fracture to get the cutting energy - or the external energy consumed in the cutting process. For each failure mechanism under consideration, the cutting energy thus calculated was normalized by dividing by the crack area generated in the workpiece. The crack lengths were obtained from the post-cut microscopy images using ImageJ™.

This approach allowed for knowing the energy consumed in the creation of a unit fracture surface ( $W_C$ ). It should be noted that the distance traversed by the tool during a fracture and the actual crack length were often different as the crack propagated ahead of the tool. The expression for normalized cutting energy is:

$$W_C = \frac{V_c \int_0^t F_c dt}{w \int_C ds}, \quad (3.1)$$

where  $V_c$  is the cutting speed,  $t$  is the time corresponding to the fracture surface generation,  $w$  is the width of the specimen and,  $\int_C ds$  is the line integral of the crack length.

The denominator in Eq. 3.1 is the fracture area corresponding to a fracture event. Fig. 3.6 shows the plot of the measured fracture areas corresponding to different failure mechanisms observed in this study.

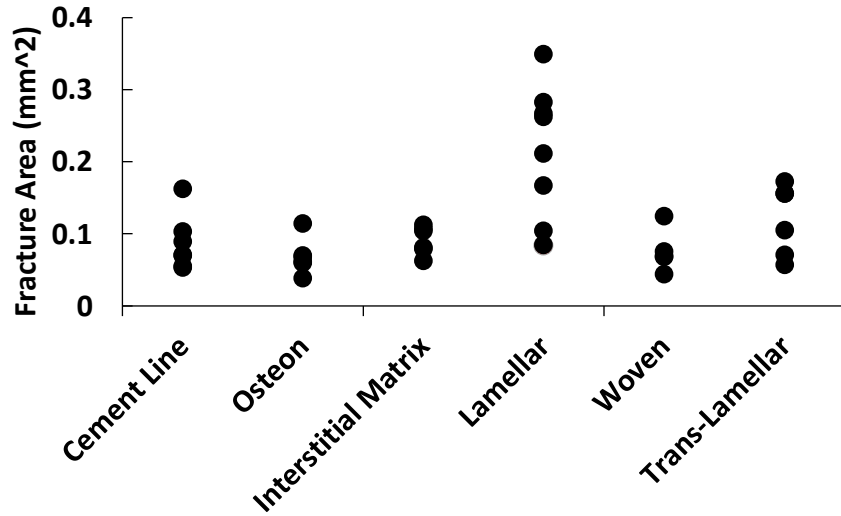


Figure 3.6: Fracture areas measured for different failure mechanisms.

Similarly, acoustic energy generated per unit fracture surface ( $W_A$ ) was found by dividing the acoustic signal energy by the crack area. The signal energy is found by the summation of the square of the signal amplitudes. The expression for normalized AE energy is:

$$W_A = \frac{\sum_{i=1}^n x_i^2}{w \int_C ds}, \quad (3.2)$$

where  $n$  is the number of samples (data points) in the AE signal and  $x_i$  is the amplitude of the  $i$ th sample (datum point).

The external energy consumed in the cutting process is translated into different forms like fracture energy of the new surface, friction energy at the tool-chip interface, and chip-fracture energy. Thus, the cutting energies calculated in this study ( $W_C$ ) are speculated to include these

phenomena. As mentioned earlier (Section 3.3), the AE signal effectively captures the fracture phenomenon during the cutting process. Thus, the acoustic energies calculated in this study ( $W_A$ ) were interpreted to be directly related to the fracture energies in the creation of new surfaces during machining.

While the normalized cutting/acoustic energies are insightful for understanding the energy spent in generating fracture surface, from a point-of-view of force monitoring it is also important to study the cutting forces observed when the specific microstructures fail during the cutting process. To this end, the normalized cutting force was also calculated, which is the average cutting force leading up-to fracture, divided by the crack area generated:

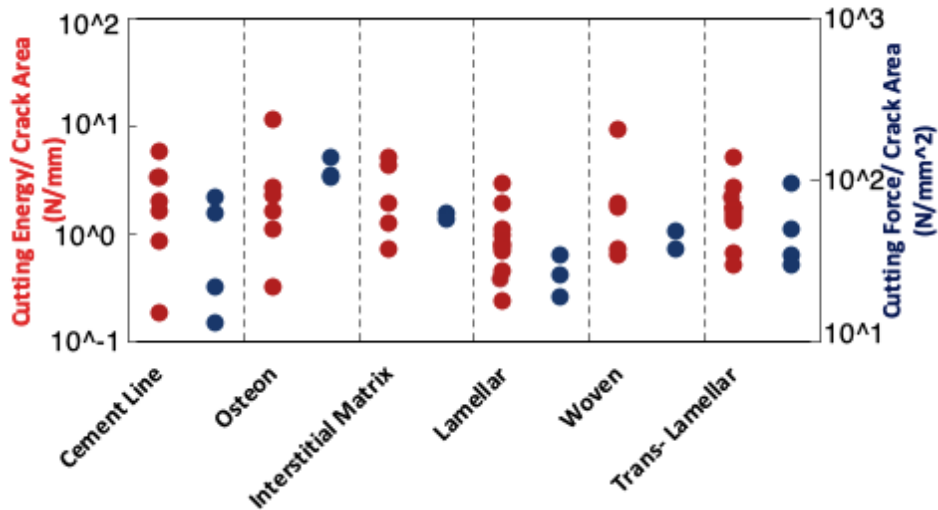
$$F_C(\text{normalized}) = \frac{\sum_{i=1}^n F_{C,i}}{nw \int_C ds}, \quad (3.3)$$

where  $n$  is the number of samples (data points) in the cutting force signal, and  $F_{C,i}$  is the cutting force corresponding to the  $i^{\text{th}}$  sample (datum point).

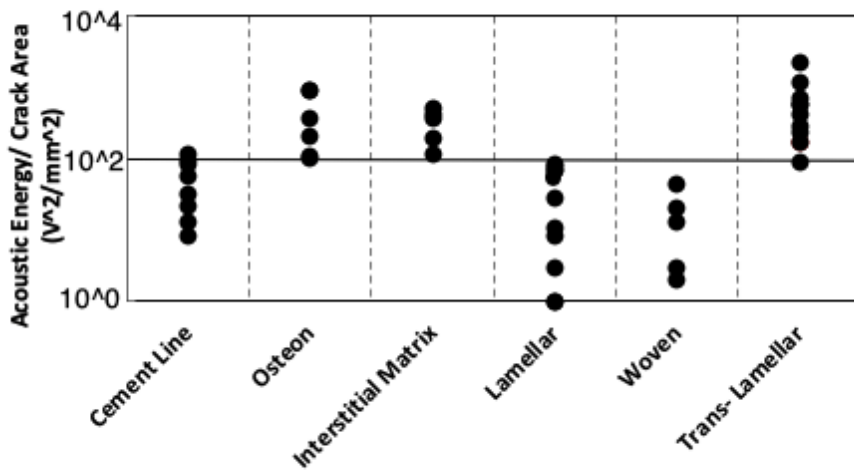
Fig. 3.7(a) shows the plot of normalized cutting energy (Eq. 3.1), as well as the normalized cutting force (Eq. 3.3) for the different failure mechanisms. It can be seen that within haversian bone, the cement line exhibits lower normalized cutting energies and forces, whereas, in plexiform bone, trans-lamellar failure exhibits higher cutting energies and forces. These trends are helpful in the general understanding of the cutting process.

While the cutting force related numbers can be calculated for the different failure mechanisms, as can be seen in Fig. 3.7(a), these are not distinct. However, the acoustic energies calculated from the AE showed more sensitivity in this regard and deserved further analysis. Fig. 3.7(b) shows the plot of normalized acoustic energies (Eq. 3.2) calculated for the different failure mechanisms. The figure shows that the general patterns in the failure mechanisms of a particular

bone type are similar to Fig. 3.7(a). It could also be seen that the osteon failure mechanism in haversian bone results in acoustic energies higher than lamellar failure in plexiform-0° bone, but comparable to transverse lamellar failure in the plexiform-90° bone. This could be explained by the resistance to fracture provided by the presence of concentric lamella in the osteons in haversian bone and planar lamella, transverse to the cutting direction, in the plexiform-90° bone.



(a)



(b)

Figure 3.7: Normalized (a) cutting energy & cutting force, and (b) acoustic energy for the different failure mechanisms.

Within haversian bone, the cement line fracture resulted in lower acoustic energies implying the osteons easily fail at the cement line interface. This can be attributed to the lower hardness of the cement line in comparison to the osteon and interstitial matrix. The similarity in response between osteon and interstitial matrix failures within the haversian bone, and woven and lamellar failures in the plexiform bone) could be attributed to their respective material properties which are not considerably different [4].

It could also be easily seen from Fig. 3.7(b) that unlike cutting energies and forces (Fig. 3.7(a)), by using AE energies the failure mechanisms within haversian and plexiform bones could be better differentiated into 2 bins, in general. Bin-1 ( $10^0 - 10^2$  V<sub>2</sub>/mm<sup>2</sup>) corresponded to cement line, lamellar and woven fracture mechanisms, whereas bin-2 ( $10^2 - 10^4$  V<sub>2</sub>/mm<sup>2</sup>) corresponded to osteon, interstitial matrix, and trans- lamellar fracture mechanisms.

The failure mechanisms considered in this study were mixed-mode fractures (mode I + mode II). The cutting energies obtained in this analysis generally exceeded the critical fracture energies ( $G_c$ ) for mode I and mode II fracture of cortical bone in longitudinal (mode I-  $0.64 \pm 0.10$  N/mm, mode II-  $2.43 \pm 0.83$ ) and transverse directions (mode I-  $1.37 \pm 0.18$  N/mm, mode II-  $4.71 \pm 1.28$ ) [124]. This indicates that while the cutting energy helps in understanding the overall cutting process, only a portion of it is caused by the fracture during the cutting process. As such, it is not an efficient metric for the fracture energies encountered during the cutting process. The better distinguishing nature of the acoustic energy makes it more suitable for monitoring the fracture phenomena in the cutting process.

### **3.5 Conclusions**

Haversian and plexiform components of bovine bone were orthogonally machined at a depth of cut of 70  $\mu$ m to induce fracture-based cutting, and the force and AE responses of the

failure mechanisms were studied. The following specific conclusions can be drawn from this work:

1. With the aid of high-speed camera images, the dominant failure mechanisms in haversian and plexiform components of bone have been correlated with their corresponding AE signatures. In haversian bone, the dominant failure mechanisms are cement line, osteon, and interstitial matrix fractures. In plexiform bone, the dominant mechanisms are lamellar, woven, and transverse-lamellar fractures.
2. The AE signal was transient and consisted of multiple ‘bursts’. These ‘bursts’ or waveforms were helpful in tracking the fracture process as the crack initiation and propagation, and the chip breakage were observed to result in AE waveforms.
3. Typical AE signatures of the different mechanisms were established. Two metrics – (i) the number of AE bursts, and (ii) the ratio of maximum-to-minimum amplitude were used to effectively distinguish the AE responses of the different failure mechanisms.
4. Acoustic energies were calculated, and it was observed that the failures in the haversian bone resulted in much higher energies than in the plexiform-0° bone. However, the trans-lamellar fracture in plexiform-90° bone results in acoustic energies comparable to haversian failure mechanisms. In haversian bone, the cement line results in lower acoustic energies than both osteon and interstitial matrix fractures, which have comparable acoustic energies.
5. AE appears to be more sensitive than the cutting force in capturing the microstructure-specific failure modes observed during fracture cutting of bovine bone.

## 4. REVIEW OF A RELEVANT MICROSTRUCTURE-BASED CUTTING FORCE MODEL FOR BONE SAWING

This chapter presents a brief review of a microstructure-specific cutting force model for bone sawing, proposed by Conward [5]. This cutting force model is reviewed here for the purposes of continuity, since the model predictions feed into the calculations of the AE prediction model developed under research Thrust 2 of this thesis (refer Chapter 5 ahead). Furthermore, the bone sawing experiments conducted for both the calibration and validation of this cutting force model are the same experiments that are to be used for the AE model calibration/validation described in Chapter 5.

The remainder of this chapter is organized as follows: Section 4.1 presents the nomenclature helpful in understanding the model flowchart and the equations presented in this chapter. Section 4.2 describes the bone sawing experiments conducted for the cutting force model calibration and validation. Section 4.3 presents the modeling approach. Section 4.4 describes the cutting force equations and the prediction outcomes. Finally, Section 4.5 presents a summary of the cutting force model.

### 4.1 Nomenclature

$r_E$	Cutting Edge Radius
$\alpha_{nom}$	Nominal Rake Angle
$\Psi$	Clearance Angle
$V$	Cutting Velocity
$w, dw$	Tool Width, Elemental Tool Width
$t_O$	Total Depth of Cut
$t_p$	Penetration Depth
$\theta$	Stagnation Angle
$\alpha_{eff}$	Effective Rake Angle
$\tau_i$	Microstructure-Specific Shear Stress

$A_i$	Microstructure-Specific Area Fraction
$G_n$	Normal Coefficient (shear)
$G_f$	Friction Coefficient (shear)
$H_n$	Normal Coefficient (plough)
$H_f$	Friction Coefficient (plough)
$a_0, a_1, b_0, b_1$	Calibrated Shearing Parameters
$c_0, c_1, d_0, d_1$	Calibrated Ploughing Parameters
$dA_s$	Elemental Shearing Area
$dA_p$	Elemental Ploughing Area
$dF_{ns}$	Elemental Normal Force (shear)
$dF_{fs}$	Elemental Friction Force (shear)
$dF_{np}$	Elemental Normal Force (plough)
$dF_{fp}$	Elemental Friction Force (plough)
$dF_{cs}$	Elemental Cutting Force (shear)
$dF_{ts}$	Elemental Thrust Force (shear)
$dF_{cp}$	Elemental Cutting Force (plough)
$dF_{tp}$	Elemental Thrust Force (plough)
$dF_{CTotal}$	Elemental Total Cutting Force
$dF_{TTotal}$	Elemental Total Thrust Force

## 4.2 Model-related Bone Sawing Experiments

The sawing experiments were conducted on a high-speed, linear-cutting fixture developed by James et al. [125] at Tufts University. Fig. 4.1 shows a photo of the experiment setup. The cutting tool, which is a single sawtooth, was mounted on the cutting tool holder attached to the dynamometer. In addition, the AE sensor (used in the studies reported in Chapter 3) was also attached to the cutting tool holder. Though the Conward cutting force model was based only on the forces measured by the dynamometer, the AE signals collected during these experiments enabled the work reported in this Chapter 5 of this thesis.

The principle of operation of this high-speed, linear-cutting fixture was described by Conward [5]. An important feature of this setup was that three ranges of depths of cut were possible in the cutting experiments. As such, three workpieces were used, corresponding to the three ranges of depths of cut.

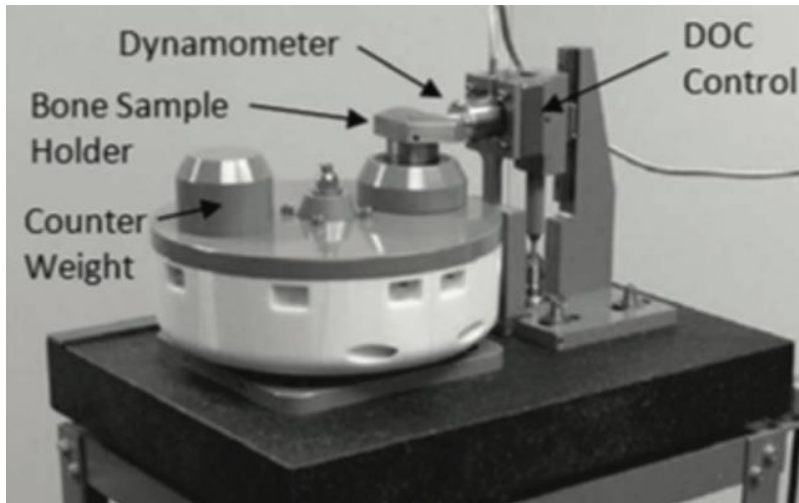


Figure 4.1: High-speed, linear-cutting fixture [125].

Bone samples harvested from the bovine femur bone were used as workpieces. The bone samples selected for this machining study contained easily identifiable haversian, and plexiform regions, as well as an intermediate ‘transition’ region as shown in Fig. 4.2. The cutting/thrust forces collected during a cut were divided into haversian, transition, and plexiform parts based on the engagement with the workpiece.

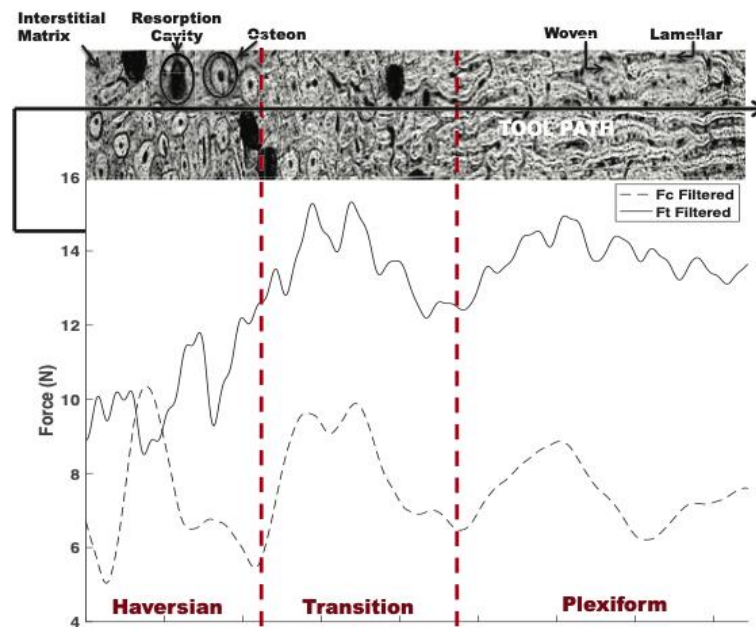


Figure 4.2: Example of cutting/thrust forces corresponding to the three identified regions in the bone sample [5].

### 4.3 Modeling Strategy

Fig. 4.3 shows the approach for force prediction, based on the proposed mechanistic cutting force model. The details of the implementation are provided in [5].

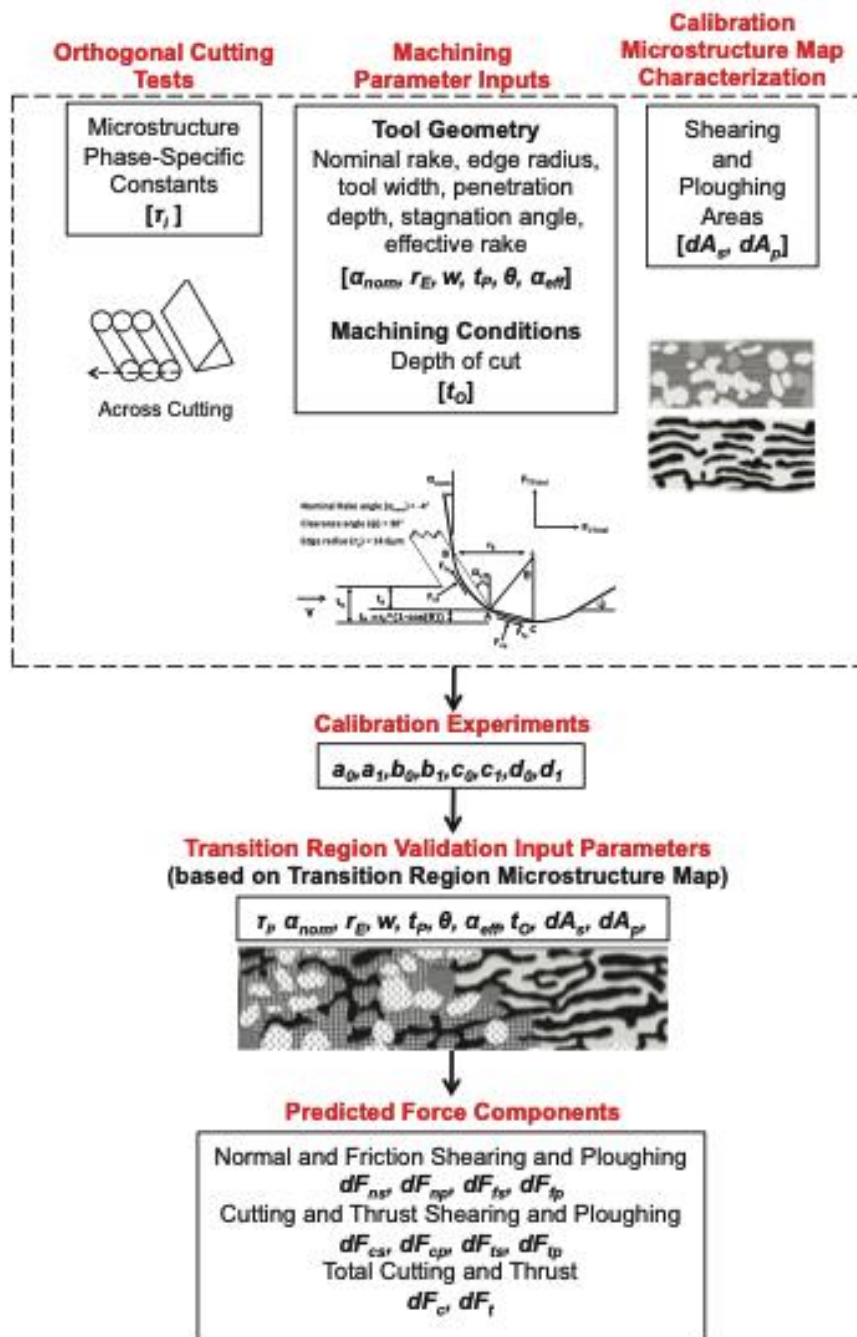


Figure 4.3: Flowchart for the force prediction model [5].

As seen in the flowchart in Fig. 4.3, the building blocks of the proposed model are – (i) microstructure-specific shear stress constants, which were determined from a separate set of orthogonal cutting experiments (see Table 4.1), (ii) cutting tool geometry parameters, considering the rounded cutting edge of the sawtooth, and (iii) identification of the area fractions of the constituent microstructures in the workpiece, based on micrographs.

It should be noted that the rounded cutting edge was divided into ‘shearing’ and ‘ploughing’ regions based on a stagnation angle ( $\theta$ ). The final predicted force components are the normal and frictional forces in the ‘shearing’ and ‘ploughing’ regions of the rounded cutting tool edge. These force components can then be resolved and added to calculate the effective cutting and thrust forces. The experimentally measured cutting and thrust forces were used to calibrate and validate this force prediction model.

The calibration of the model was based on the cutting/thrust forces from the pure haversian and plexiform regions of the workpiece, and the calibration coefficients were determined (Table 4.2 ahead). The validation was done on the transition region of the bone, which consisted of both haversian and plexiform microstructures.

**Table 4.1: Microstructure-specific shear stress values [5].**

<b>Material (<i>i</i>)</b>	<b>Volume Fraction</b>	<b><math>\tau_i</math> (MPa)</b>
Osteon	0.7	305
Interstitial Matrix	0.3	121
Lamellar	0.4	469
Woven	0.6	146

#### **4.4 Cutting Force Equations and Predictions**

The expressions for the normal and frictional force in the ‘shearing’ region, i.e.,  $\hat{F}_{ns}$  and  $\hat{F}_{fs}$ , and the normal and frictional force in the ‘ploughing’ region, i.e.,  $\hat{F}_{np}$  and  $\hat{F}_{fp}$ , are given as:

$$\hat{F}_{nS} = \sum_w d\hat{F}_{nS} = \sum_w ([a_0(t_0)^{a_1} \sum_i \tau_i A_i] t_S dw), \quad (4.1)$$

$$\hat{F}_{fS} = \sum_w d\hat{F}_{fS} = \sum_w ([b_0(t_0)^{b_1} \sum_i \tau_i A_i] t_S dw), \quad (4.2)$$

$$\hat{F}_{nP} = \sum_w d\hat{F}_{nP} = \sum_w ([c_0(t_0)^{c_1} \sum_i \tau_i A_i] t_P dw), \text{ and} \quad (4.3)$$

$$\hat{F}_{fP} = \sum_w d\hat{F}_{fP} = \sum_w ([d_0(t_0)^{d_1} \sum_i \tau_i A_i] t_P dw), \quad (4.4)$$

where the subscript  $i$  refers to the specific microstructure component, viz. osteon, interstitial matrix, woven, or lamellar bone, and  $A_i$  and  $\tau_i$  are the area fraction and shear stress, respectively, of the  $i$ th microstructural component,  $\alpha_{eff}$  is the effective rake angle, ( $a_0, a_1, b_0, b_1, c_0, c_1, d_0, d_1$ ) are the calibrated constants,  $t_S$  is the shear depth of cut,  $t_P$  is the penetration depth,  $dw$  is the elemental tool width, and  $\theta$  is the stagnation angle.

The expression for the effective rake angle  $\alpha_{eff}$ , to be used in Eq 4.1-4.4, is given as:

$$\alpha_{eff} = \tan^{-1} \frac{(c \frac{t_O}{r_E} - 1) \tan(\alpha_{nom}) - \sec(\alpha_{nom}) + \sin \theta}{c \frac{t_O}{r_E} - 1 + \cos \theta} \text{ when } \dots c * \frac{t_O}{r_E} > 1 + \sin \alpha_{nom}, \text{ and} \quad (4.5)$$

$$\alpha_{eff} = \tan^{-1} - \frac{\sqrt{(2 - c \frac{t_O}{r_E}) c \frac{t_O}{r_E} - \sin \theta}}{c \frac{t_O}{r_E} - 1 + \cos \theta} \text{ when } \dots c * \frac{t_O}{r_E} \leq 1 + \sin \alpha_{nom}, \quad (4.6)$$

where  $\theta$  is the stagnation angle, and ( $\alpha_{nom}$ ) is the nominal rake angle. The variables  $t_O$  and  $r_E$  are the uncut chip thickness and tool edge radius, respectively. The constant  $c$  is assumed to be 2 [5].

As mentioned earlier, microstructure-specific shear stress values ( $\tau_i$ ) are also required for calculating the force components in Eq. 4.1-4.4 These shear stress values are listed in Table 4.1. The approach for estimating these values from a separate set of experiments are described in [5].

The model was calibrated on the cutting and thrust forces from the pure haversian and plexiform regions of the bone. The calibration constants thus obtained are shown in Table 4.2.

**Table 4.2: Calibration constants [5].**

Haversian Bone							
Shearing				Ploughing			
$a_0$	$a_1$	$b_0$	$b_1$	$c_0$	$c_1$	$d_0$	$d_1$
1.69	-0.45	1.34	-3.36	0.53	-0.61	3.16	-1.92
		E-7	E-14			E-8	E-12
Plexiform Bone							
Shearing				Ploughing			
$a_0$	$a_1$	$b_0$	$b_1$	$c_0$	$c_1$	$d_0$	$d_1$
8.63	-0.10	2.98	-0.08	3.44	-0.35	0.35	-9.52

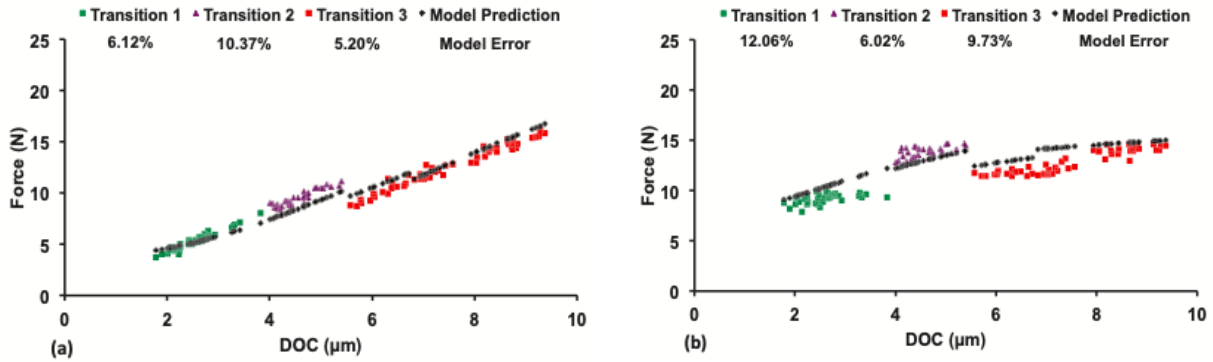


**Figure 4.4: Plots of (a) cutting force, and (b) thrust force prediction in the transition region [5].**

Using Eq. 4.1-4.4, the normal and frictional forces are predicted. Consequently, the total cutting and thrust forces can be predicted. Fig. 4.4 shows the plots of the cutting and thrust force predictions in the transition region of the bone. It can be seen that the model exhibits high accuracy and the errors are less than 10 % on average. It should be noted here that ‘Transition 1,2,3’ refer to the three datasets corresponding to three different workpieces that were cut at the three ranges of depths of cut as shown in these plots.

## 4.5 Summary

A microstructure-based mechanistic cutting force model in bone sawing was proposed by Conward [5]. This model was calibrated on the haversian and plexiform regions of the bovine cortical bone and successfully validated on the transition region. The model allowed for predicting

the cutting force components from the cutting-related shearing and ploughing phenomena along the rounded cutting tool edge. These cutting force components are helpful in calculating the energy dissipation from the shearing and ploughing effects. Chapter 5 of this thesis deals with an AE signal power prediction model, where the underlying premise is the relationship between the AE signal power and the work rates from the cutting-related shearing and ploughing. As such, the cutting force predictions described in this chapter will feed into the calculations described in Chapter 5. Also, the bone sawing experiments described in this chapter are the same experiments used in the calibration and validation of the AE model in Chapter 5.

## **5. MICROSTRUCTURE-BASED MECHANISTIC MODEL FOR BONE SAWING: ACOUSTIC EMISSION SIGNAL POWER PREDICTIONS**

This chapter presents the research dealing with research Thrust 2, which involves AE analysis of the shear-cutting of bovine cortical bone. Building upon the mechanistic cutting force model described in Chapter 4, an AE prediction model was developed. The objective of this work is focused on modeling the AE signal power, i.e.,  $(AE_{rms})^2$ , as a function of the specific cortical bone microstructures and depth of cut encountered by the bone-saw tooth. First, the AE signal characteristics from the sawing experiments are correlated with the haversian and plexiform regions of the cut. Using the cutting force predictions from Conward [5], the AE signal power is modeled based on the energies dissipated in the shearing and ploughing zones encountered by the rounded cutting edge. The spread seen in the AE signal power is captured by modeling the variations in sawed surface height profile, tool cutting edge geometry, and porosity of the bone. The AE model is first calibrated on pure haversian and pure plexiform regions of the bovine cortical bone and then validated on the transition region containing mixed haversian and plexiform microstructures. The validated AE model is then used to predict the AE signal power trends and the cutting force variations, based on the differences in the underlying bone microstructures.

The remainder of this chapter is organized as follows. Section 5.1 presents the nature of the AE signal collected while sawing through the different underlying microstructural compositions. Section 5.2 describes the basic model assumptions and the different energy dissipation components. Section 5.3 describes key model modifications needed for this model development, and Section 5.4 presents the calibration and validation of the proposed model.

Section 5.5 presents two process-planning applications of this model. Finally, Section 5.6 presents the specific conclusions that can be drawn from this work.

## 5.1 Acoustic Emission in Bone Sawing

For continuity, Table 5.1 provides a summary of the experimental conditions to generate both the cutting forces and acoustic emission signatures. These are the same experimental conditions from the bone sawing experiments involved in the cutting force model described in Chapter 4.

**Table 5.1: Summary of the experimental conditions [5].**

<b>Workpiece</b>	<ul style="list-style-type: none"> <li>• Bovine cortical bone sample polished perpendicular to osteon orientation</li> </ul>
<b>Cutting Tool</b>	<ul style="list-style-type: none"> <li>• Bone Saw tooth- Stainless steel</li> <li>• 14.6 <math>\mu\text{m}</math> edge radius</li> <li>• <math>-4^\circ</math> rake angle</li> <li>• <math>30^\circ</math> clearance angle</li> <li>• 740 <math>\mu\text{m}</math> wide</li> </ul>
<b>Cutting Speed</b>	<ul style="list-style-type: none"> <li>• 3700 mm/s</li> </ul>
<b>Depth of cut (DOC)</b>	<ul style="list-style-type: none"> <li>• Data Set 1 (Low): 1.8-3.8 <math>\mu\text{m}</math></li> <li>• Data Set 2 (Medium): 4.0-5.4 <math>\mu\text{m}</math></li> <li>• Data Set 3 (High): 5.6-9.4 <math>\mu\text{m}</math></li> </ul>

The haversian bone consists of osteons held together by the interstitial matrix, whereas the plexiform bone consists of lamellar and woven regions that are interconnected. Due to these distinct microstructures and their associated properties, it is expected that the bone types will behave differently in terms of the AE generated during sawing. Fig. 5.1 shows a typical AE signal from the bone sawing tests at a depth of cut of 4.7  $\mu\text{m}$ . In this figure, the haversian region is on the extreme left and the plexiform region is on the extreme right. Fig. 5.1(b) shows that the nature of this continuous signal changes visibly both in terms of its magnitude and relative burst cycles as microstructure changes from haversian to plexiform. Differences between the two bone types

are best captured while considering the AE signal power, i.e.,  $(AE_{rms})^2$ , which is directly related to energy dissipation mechanisms during the cutting process [126].

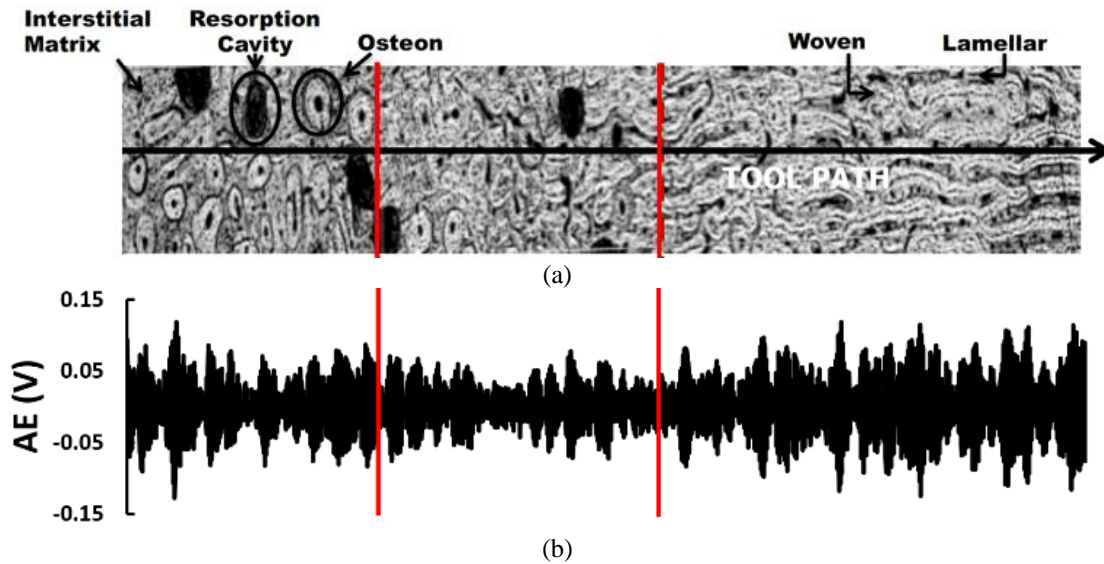


**Figure 5.1:** (a) Bone sample with haversian region on the left and plexiform region on the right, and (b) acoustic emission signal as the tool cuts the bone sample from left to right.

Fig. 5.2 shows the plot of the AE signal power ( $\text{Volt}^2$ ) as a function of the depth of cut (DOC) during the sawing process. As seen, plexiform samples have a distinctly higher value over haversian samples, at  $\text{DOC} > 3 \mu\text{m}$ . Furthermore, it is also clear that there is a non-linear trend in the AE signal power as a function of the DOC, with a specific drop seen after a DOC of  $7.3 \mu\text{m}$ .

On an average, the correlation coefficients between the resultant cutting force values (Conward [5], and Fig. 4.4 in Chapter 4) and the AE signal power across the three DOC ranges are found to be 0.9, 0.7 and 0.1, respectively, across the low DOC ( $1.8\text{-}3.8 \mu\text{m}$ ), medium DOC ( $4.0\text{-}5.4 \mu\text{m}$ ) and high DOC ( $5.6\text{-}9.4 \mu\text{m}$ ). This decrease in correlation between the AE signal power and the cutting force, with increasing DOC, is due to the shift from a ploughing-dominated to a shearing-dominated failure during the sawing process.

However, at higher DOCs when shear failure is dominant, the AE signal appears to be more sensitive to the variations in the microstructures, including the presence of cavities. This results in

a decreased correlation between the AE signal and the cutting force. Thus, for effectively modeling the AE signal power in bone sawing, in addition to the prevalent ploughing and shear mechanisms, the variations in microstructures such as porosity and cavities, and the likelihood of damage through the interfacial micro-cracks, will also need to be considered. Section 5.2 details the basic modeling approach.

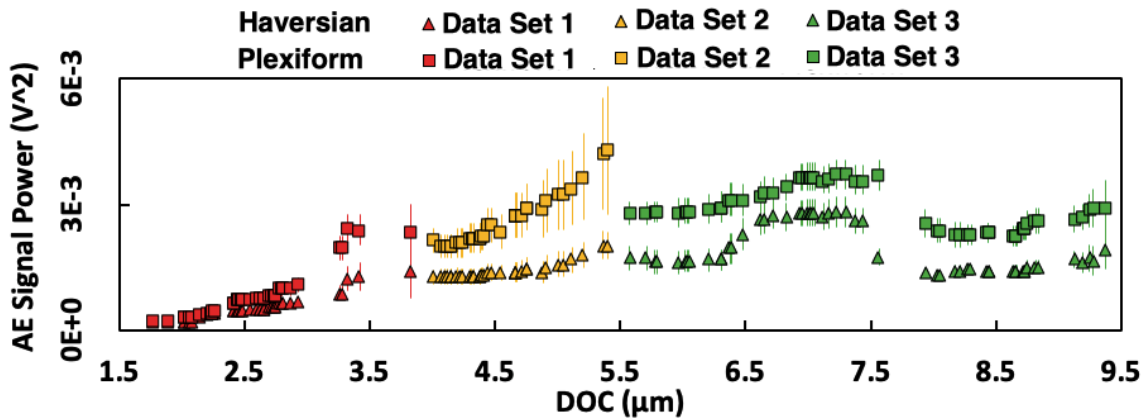


Figure 5.2: Experimental acoustic emission signal power, i.e.,  $(AE_{rms})_2$ , from the haversian and plexiform bones. [Note: Data Sets 1, 2, and 3 correspond to DOCs 1.8 – 3.8  $\mu\text{m}$ , 4.0 – 5.4  $\mu\text{m}$ , and 5.6 – 9.4  $\mu\text{m}$ , respectively]

## 5.2 Basic Model Assumptions and Energy Dissipation Components

The model presented in this Chapter will focus on predicting the AE signal power, i.e.,  $(AE_{rms})_2$ , as a function of the specific cortical bone microstructures and depth of cut encountered by the bone-saw tooth. It will use the cutting force predictions from the microstructure-based cutting force model described in Chapter 4, to compute key contributions to the AE signal power that are related to the cutting mechanisms at play. Besides, specific modifications related to the workpiece-tool interaction and the effect of the interfaces will also be introduced. The model coefficients will be calibrated using the experimental data (Fig. 5.2). The model will be calibrated first on the haversian and the plexiform regions and then validated for the gradient microstructures present in the transition region (Fig. 5.1).

### 5.2.1 Model Assumptions

The following three assumptions are made in modeling the AE signal power:

**Assumption 1:** The total AE signal power encountered for the rounded edge geometry of the sawtooth (Fig. 5.3(a)) can be modeled as a combination of two independent processes, viz. (i) shear-based cutting from a negative rake cutting tool, and (ii) ploughing deformation from a round-nose indenter. This assumption, which is in line with the prior modeling work of Liu et al. [127], results in two independent sub-problems as shown in Fig. 5.3(b)&(c). The location of the stagnation-point A (Fig. 5.3(a)), will be used for separating these two sub-problems. The effective rake angle,  $\alpha_{\text{eff}}$  (see Eq. 4.5 in Chapter 4) will be the rake angle of the shear cutting sub-problem, while the stagnation depth will be used for the ploughing deformation sub-problem. Given this framework, the shearing components calculated for the rounded saw-tooth profile can now be transferred to the shear cutting sub-problem in Fig. 5.3(b). Similarly, the ploughing components calculated for the rounded saw-tooth profile can now be transferred to the ploughing deformation sub-problem in Fig. 5.3(c). It should be noted here as shown in Fig. 5.3(b), the shear cutting sub-problem also assumes 2D, orthogonal cutting. This assumption of orthogonal cutting in the sawing process is based on the saw blade width being more than 70 times larger than the depths of cuts considered, which effectively results in negligible side shear forces as compared to the cutting/thrust forces from shearing and ploughing [125].

**Assumption 2:** Cutting velocity components in the shear-based cutting problem (Fig. 5.3(b)) are assumed to not influence the ploughing deformation problem (Fig. 5.3(c)). This assumption is rooted in the high hardness and low elastic recovery of the bovine cortical bone, both of which result in minimal plastic side-flow in the ploughing zone.

**Assumption 3:** Under comparable machining conditions of DOC, tool geometry and cutting velocity, the shear-plane angle is assumed to be the same for the haversian and the plexiform bone-types. This is based on the experimental observations from Conward [5] that indicate that the maximum variation seen in the shear-plane angles as a function of microstructural variations was limited to only 20.

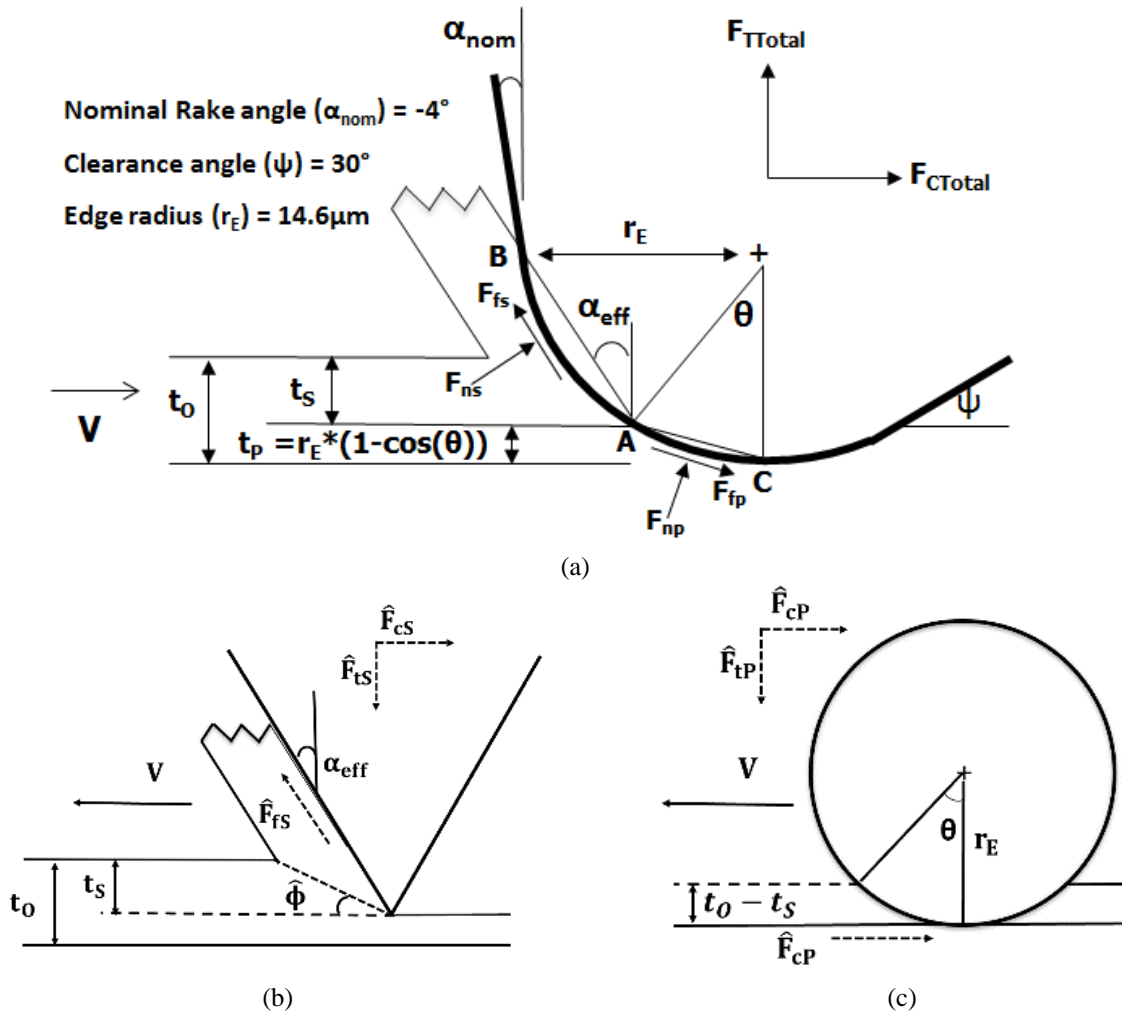


Figure 5.3: Cutting tool geometry - (a) rounded cutting-edge framework for bone sawing, (b) shear cutting sub-problem, and (c) ploughing deformation sub-problem.

In addition to these assumptions, it should be noted that in this study the notation  $(\hat{\quad})$  is used to indicate model prediction estimates. Furthermore, the subscript  $i$  refers to the four key microstructural components, viz. osteon, interstitial matrix, woven bone, and lamellar bone. For

each of the three distinct regions in Fig. 5.1, viz. pure haversian region, transition region, and plexiform region, the summation of their respective area fractions ( $A_i$ ) is always equal to 1 (i.e.,  $\sum_i A_i = 1$ ). However, it is only in the transition region that all four of the microstructural components are present. The pure haversian region is only comprised of two components, viz. osteon, and interstitial matrix. Similarly, the pure plexiform region is comprised only of two components, viz. woven and lamellar bone. Given this distribution of the microstructural components, the model coefficients of the AE model are calibrated first on the pure haversian and the pure plexiform regions. The model predictions are then validated on the transition region that has varying area-fractions of all four of the microstructural components.

### 5.2.2 Shearing and Ploughing Contributions

In the 2D shear-cutting sub-problem (Fig. 5.3(b)), energy dissipation that occurs through primary shear and rake friction are the major contributors towards the AE signal power, whereas, in the ploughing region (Fig. 5.3(c)) energy dissipation occurs primarily through the plastic side-flow of the material. From the thesis of Conward [5], ( $\hat{F}_{CS}$ ), ( $\hat{F}_{TS}$ ), and ( $\hat{F}_{FS}$ ) were identified, respectively, as the cutting force, thrust force and the rake-face friction-force estimates, all originating from the shear-cutting mechanism. Similarly, ( $\hat{F}_{CP}$ ) was identified as the cutting force component that originates from the ploughing mechanism. These force estimates are calculated using the expressions below [5]:

$$\hat{F}_{CS} = \sum_w d\hat{F}_{CS} = \sum_w(\cos \alpha_{eff}[G_n \sum_i \tau_i A_i]t_S dw) + \sum_w(\sin \alpha_{eff}[G_f \sum_i \tau_i A_i]t_S dw), \quad (5.1)$$

$$\hat{F}_{TS} = \sum_w d\hat{F}_{TS} = \sum_w(-\sin \alpha_{eff}[G_n \sum_i \tau_i A_i]t_S dw) + \sum_w(\cos \alpha_{eff}[G_f \sum_i \tau_i A_i]t_S dw), \quad (5.2)$$

$$\hat{F}_{FS} = \sum_w d\hat{F}_{FS} = \sum_w([G_f \sum_i \tau_i A_i]t_S dw), \text{ and} \quad (5.3)$$

$$\hat{F}_{CP} = \sum_w d\hat{F}_{CP} = \sum_w(\sin \theta [H_n \sum_i \tau_i A_i]t_P dw) + \sum_w(\cos \theta [H_f \sum_i \tau_i A_i]t_P dw), \quad (5.4)$$



independent of the underlying microstructure. Therefore,

$$\dot{E}_1 = [\hat{F}_{cS} \cos(\hat{\Phi}) - \hat{F}_{tS} \sin(\hat{\Phi})] * V \frac{\cos(\alpha_{eff})}{\cos(\hat{\Phi} - \alpha_{eff})}, \text{ and} \quad (5.5)$$

$$\dot{E}_2 = \hat{F}_{fs} * V \frac{\sin \hat{\Phi}}{\cos(\hat{\Phi} - \alpha_{eff})}, \quad (5.6)$$

where  $V$  is the cutting speed,  $\alpha_{eff}$  is the effective rake angle, and  $\hat{\Phi}$  is the estimated shear angle.  $\hat{\Phi}$  is estimated from the chip thickness measurements as:

$$\hat{\Phi} = \text{Tan}^{-1} \left( \frac{\frac{t_c}{t_0 - r_E(1 - \cos \theta)} \cos \alpha_{eff}}{1 - \frac{t_c}{t - r_E(1 - \cos \theta)} \sin \alpha_{eff}} \right), \quad (5.7)$$

where  $t_c$  is the experimentally estimated chip thickness,  $t_0$  is the total depth of cut (Fig. 5.3(b)),  $\alpha_{eff}$  is the effective rake angle, and  $\theta$  is the stagnation angle (Fig. 5.3(a)). Given the nature of the experimental tests, chips could only be collected intermittently in the three DOC ranges. Table 5.2 provides these average chip thickness values that were measured along with the estimated shear angle. For other DOC values relevant to the study, the shear angles were obtained by interpolating between these three values across the DOCs.

**Table 5.2: Observed chip thickness values.**

Average DOC ( $t_0$ ) in $\mu\text{m}$	Average Chip Thickness ( $t_c$ ) in $\mu\text{m}$	Estimated Shear Angle ( $\hat{\Phi}$ ) in radians
2.8	4.61±0.88	0.43
4.7	5.46±1.99	0.54
7.5	10.41±2.17	0.62

In the ploughing sub-problem (Fig. 4.6(c)), energy dissipation can be captured as the product of the cutting force component that originates from the ploughing mechanism ( $\hat{F}_{cP}$ ) and the cutting velocity ( $V$ ). This is expressed as  $\dot{E}_3$  and is calculated as:

$$\dot{E}_3 = \hat{F}_{cP} * V, \quad (5.8)$$

The total AE signal power considering the three deformation regions can now be expressed as:

$$\dot{E}_{\text{Total}} = \Psi_{\text{tool} | \text{DOC}} \sum_{k=1}^3 C_k E_k, \quad (5.9)$$

where  $\Psi_{\text{tool} | \text{DOC}}$  is a constant of proportionality signifying the conversion of energy dissipation as experienced by the cutting tool, into energy of the acoustic signal collected by the AE sensor attached to the cutting tool holder.

It should be noted here that the experiments consisted of using three different wedges in the sawing experiment setup to obtain the three ranges of low, medium and high DOCs (refer Chapter 4). This also resulted in reclamping the cutting tool and reattaching the AE sensor each time the wedge is changed. As such the proportionality constant  $\Psi_{\text{tool} | \text{DOC}}$  is expected to change for the three different ranges of DOCs. Thus, three values of  $\Psi_{\text{tool} | \text{DOC}}$  are obtained by calibration, corresponding to the low, medium, and high range of DOCs.

The signal attenuation constants ( $C_1, C_2, C_3$ ) correspond to the transmission losses in the three regions of deformation zones – primary (primary shear), secondary (rake-friction) and tertiary (friction in ploughing) [43]. The values of  $\Psi_{\text{tool} | \text{DOC}}, C_1, C_2, C_3$  are calibrated using the experimental data.

It should be noted that Eq. 5.9 is valid under ideal sawing conditions where the AE energy is seen to increase with DOC. However, the high variance in the AE data and its non-linear relationship with DOC, especially at high values, requires that the Eq. 5.9 be modified to account for these issues.

### **5.3 Model Modifications**

Three key model modifications are introduced in this section to account for the effects of

(i) interface-dominant micro-cracking; (ii) realistic tool-workpiece interaction; and (iii) porosity. It should be noted here that the trends in the experimental data show that the AE data are more sensitive to these factors than the cutting forces reported by Conward [5]. Therefore, while these factors are considered here for the AE model, these were not critical to the cutting force model (Chapter 4).

### 5.3.1 Effect of Microstructure Interfaces

This modification for the AE signal power calculation is required to account for the drop in the AE signal power at DOCs greater than 7.3  $\mu\text{m}$ . It is captured using an empirical relationship between the drop in the signal power and the number of interfaces in the workpiece material. For the haversian bone, the cement lines serve as these interfaces, whereas for plexiform bone, the interface between the lamellar and woven bone serves this purpose. This premise of microstructural interfaces serving as ‘fault lines’ for damage is based on prior literature that has observed this effect at higher depths of cut [20]. The AE signal power, based on the evidence of damage in interfaces, is captured as:

$$\dot{E}_{\text{Total}}' = \dot{E}_{\text{Total}} - \delta Mnt_0, \text{ where} \quad (5.10)$$

$$\delta = \begin{cases} 0 & t_0 < 7.3 \mu\text{m} \\ 1 & t_0 \geq 7.3 \mu\text{m} \end{cases}$$

and  $M$  is an experimentally determined calibration factor,  $t_0$  is DOC, and  $n$  is the number of interfaces per unit area. Using microscopy images, the value of  $n$  was determined to be  $26 \pm 4$  and  $30 \pm 3$  interfaces/ $\text{mm}^2$ , respectively, for haversian and plexiform bone. For the transition region, this value came out as  $29 \pm 3$  interfaces/ $\text{mm}^2$ . The empirical relation in Eq. 5.10 hypothesizes that the debonding damage across these interfaces seen during shearing-dominated conditions generates less AE when compared to that seen in ploughing-dominated traversal of the tool across

these interfaces. This drop is related to the debonding events during the cutting process, which will be dictated by the number of interfaces in the workpiece. Hence, the term  $n$ , which is the number of interfaces per unit area, was incorporated into the calculations.

### **5.3.2 Realistic Tool-Workpiece Intersection**

The probability of encountering the workpiece material at a specified DOC is both a function of the tool edge profile variation as well as the variations in the height of the bone surface.

#### *5.3.2.1 Tool Edge Variation*

The tool edge profile variation was quantified using surface scans with an optical profilometer. About 8 surface scans were taken along the width of the cutting tool edge.

Fig. 5.5(b) shows two extreme cutting tool edge profiles measured from the round nose of the cutting tool that corresponds to the lowest and the highest variations in the surface height of the cutting tool edge with standard deviations being  $1.05 \mu\text{m}$  and  $2.56 \mu\text{m}$ , respectively. These variations are significant given that the sawing experiments are being conducted at DOCs  $< 10 \mu\text{m}$  and the edge radius is  $\sim 15 \mu\text{m}$ . As bone sawing is a sub-radius cutting process, these variations imply that as the tool cuts through the workpiece multiple times, the cutting edge cannot be assumed to be the same for all of these cuts. Assuming the height variation to be normally distributed with a mean of zero,

Fig. 5.5(c) shows the corresponding probability density functions (PDFs) of the two cutting edge profiles. The PDFs will be helpful in estimating the probability of the material being cut in this study.

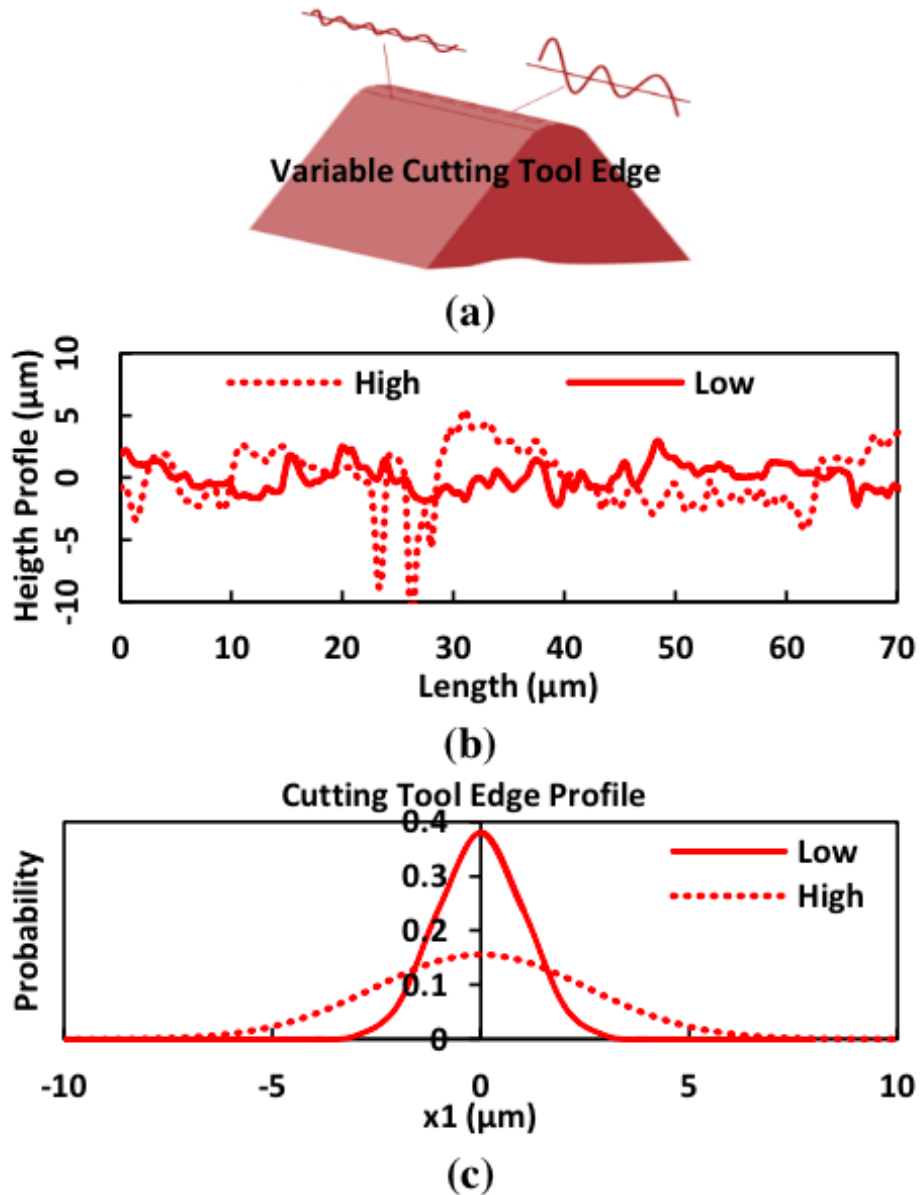


Figure 5.5: (a) Cartoon of the rounded cutting tool edge showing variable edge profiles, (b) height profiles of two cutting tool edge measurements – lowest and highest variations, and (c) corresponding pdfs of the two edge profiles.

### 5.3.2.2 Workpiece Surface Height Variation

The bone sawing experiments involve multiple passes of the sawtooth with increasing DOC. This mode of cutting implies that the height variations on the workpiece surface play a key role in dictating the probability of the material being cut at a particular DOC. To understand how

the workpiece surface profile changes during the sawing process, about 8 optical microscopy images of the surface were taken.

Fig. 5.6(a)&(b) show two osteon-rich workpiece regions from the sawing passes corresponding to 2.93  $\mu\text{m}$  and 9.37  $\mu\text{m}$ , DOC, respectively. The data from multiple specimens reveals that the surface height profiles change for both DOC and bone type (i.e., haversian or plexiform). For haversian bone with osteon and interstitial matrix as its microstructural constituents, the standard deviation of the surface height profiles to the datum surface was seen to increase from 1.66  $\mu\text{m}$  to 5.76  $\mu\text{m}$  as the average DOC increases from 2.93  $\mu\text{m}$  and 9.37  $\mu\text{m}$ . For

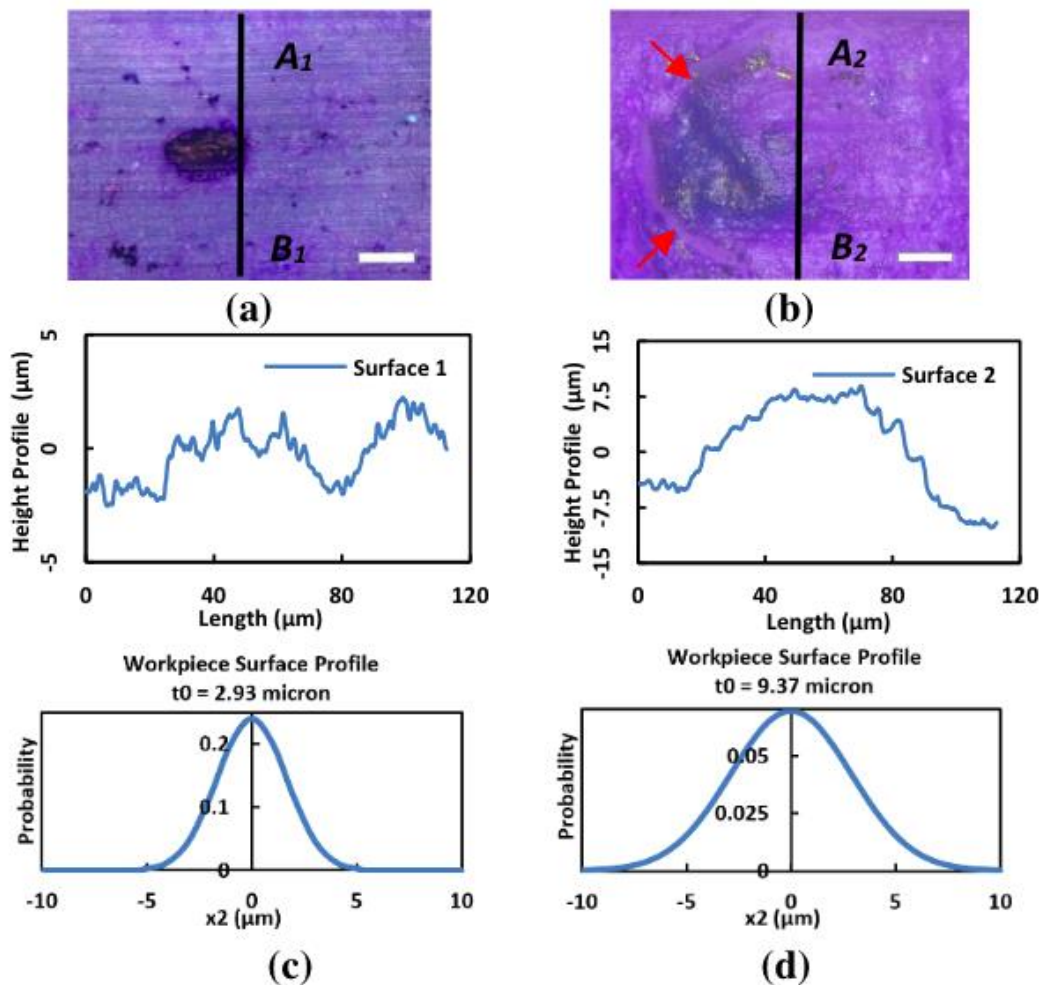


**Figure 5.6: Microscopy image of osteon on machined workpiece surface after (a) 2.93  $\mu\text{m}$  DOC, and (b) 9.37  $\mu\text{m}$  DOC showing damage around the osteon (Scale: 25  $\mu\text{m}$ ), the surface height profiles and the pdfs in (c) and (d) correspond to the two line-sections marked in (a) and (b), respectively.**

the corresponding cases of plexiform bone with lamellar and woven bone as its constituents, the standard deviation of the surface height profiles is seen to increase from 1.63  $\mu\text{m}$  to 2.16  $\mu\text{m}$  over the same DOC range. Assuming the surface heights to be normally distributed around a mean of zero (datum surface), PDFs similar to those in Fig. 5.6(c)&(d) can be generated.

### 5.3.2.3 Evaluating the Probability of Cutting Material

The evidence of the variations in the workpiece surface height and the cutting tool edge profiles points to a variation in the probability of the material being cut at a particular DOC. Fig. 5.7 (a) depicts how realistic material removal appears at a programmed DOC ( $t_0$ ) while taking into consideration the cutting tool edge and workpiece surface height variations.

To effectively determine the cutting tool edge and workpiece surface interaction, all distributions are fitted along the mean of 0 with the corresponding standard deviation. If the cutting edge profile,  $X_1$ , follows a normal distribution  $N(0 \mu\text{m}, \sigma_1 \mu\text{m})$  and the surface height profile,  $X_2$ , follows a normal distribution  $N(0 \mu\text{m}, \sigma_2 \mu\text{m})$  then as the tool moves *into the workpiece*, the difference between tool edge and workpiece profile ( $X_1 - X_2$ ) will be a normal distribution with a mean ( $\mu_1 - \mu_2$ ) equal to  $-t_0 \mu\text{m}$ , and a standard deviation of  $\sqrt{\sigma_1^2 + \sigma_2^2}$ . The area under the corresponding PDF curve for negative values of ( $X_1 - X_2$ ) signifies the probability of material being cut, as  $(X_1 - X_2) < 0$  indicates material is being removed. Fig. 5.7(b)&(c) show the PDF of ( $X_1 - X_2$ ) at depth of cuts of 2.93  $\mu\text{m}$  and 9.37  $\mu\text{m}$  taking into consideration the lowest and the highest variation seen in the data. Finally, Fig. 5.7(d) shows the  $p(t_0)$  values interpolated for all DOCs. This is used as an estimate of the probability of material being cut at the given DOC. The nature of the  $p(t_0)$  plot is suggestive of the variation in experimental data observed in Fig. 5.2. It should be noted here that  $p(t_0)$  values for the transition regions are required for the validation of

the model. In the transition region, the constituent microstructures of both haversian and plexiform regions are present. The  $p(t_0)$  in those cases was estimated based on a weighted average of the haversian and plexiform values, with the weights being the area fractions  $A_i$  of the microstructures.

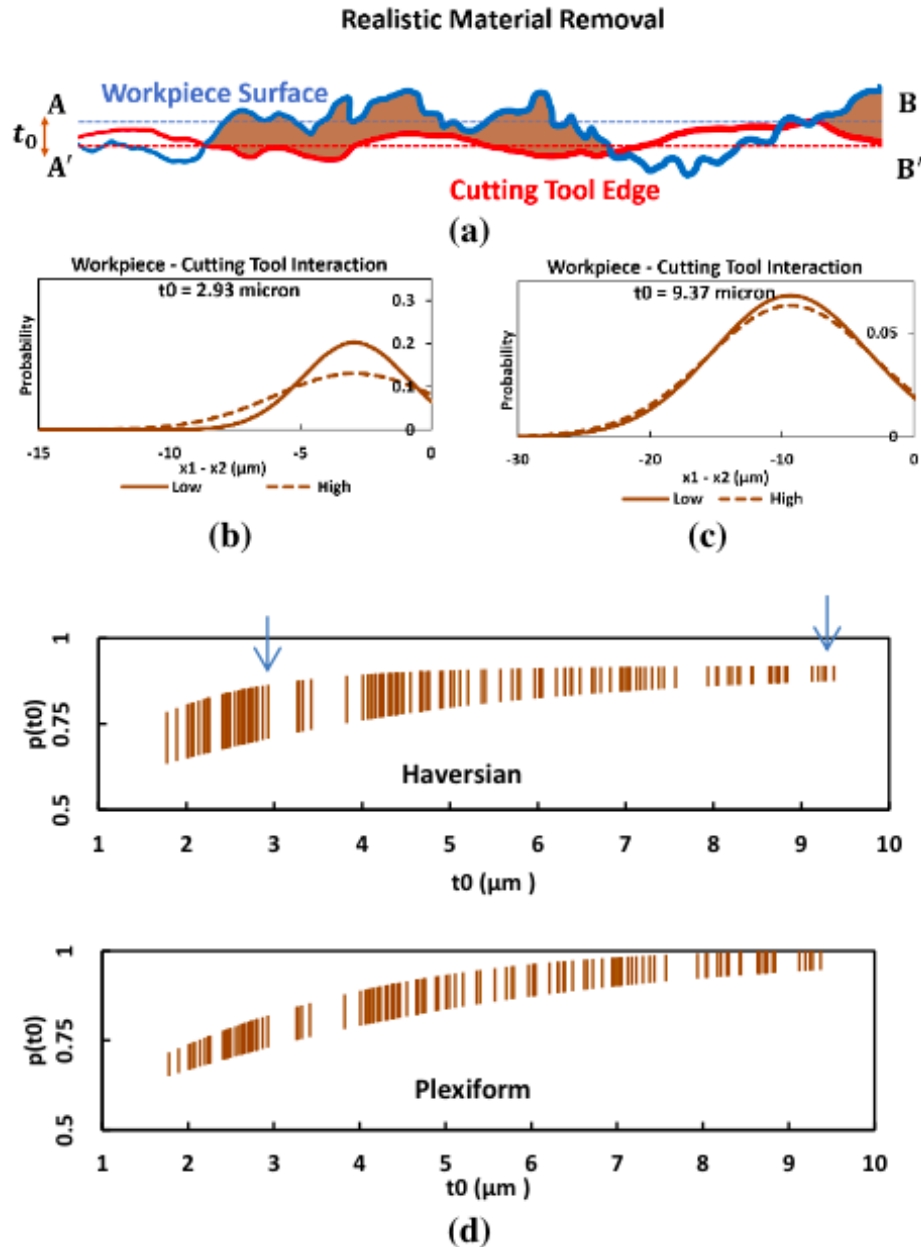


**Figure 5.7:** (a) Cartoon showing the interaction of the cutting tool edge (baseline A'-B') and the workpiece surface (baseline A-B) for a nominal DOC ( $t_0$ ), showing actual material removal, (b) interaction of the probabilities at  $t_0$  2.93  $\mu\text{m}$ , based on low and high cutting edge variations, (c) interaction of the probabilities at  $t_0$  9.37  $\mu\text{m}$ , based on low and high cutting edge variations, and (d) the resultant  $p(t_0)$  plot for the haversian, along with a similarly obtained plot for the plexiform region.

### 5.3.3 Porosity Effect

The probability of encountering material at a given DOC needs to be adjusted taking into consideration the porosity in the material. This is done using the area fraction of resorption cavities and porosity ( $A_{\text{Porosity}}$ ) that is estimated using microscopy images of the haversian and plexiform bones (Fig. 5.8). The digital image analysis reveals that for the haversian bone comprised of the osteon and interstitial matrix constituents, this porous area fraction is around  $11\pm3\%$ . The corresponding value for plexiform bone comprised of woven and lamellar constituents is  $8\pm3\%$ . Similar analysis of the transition region containing a mix of the microstructures associated with haversian and plexiform regions, revealed a porous area of about  $10\pm2\%$ .

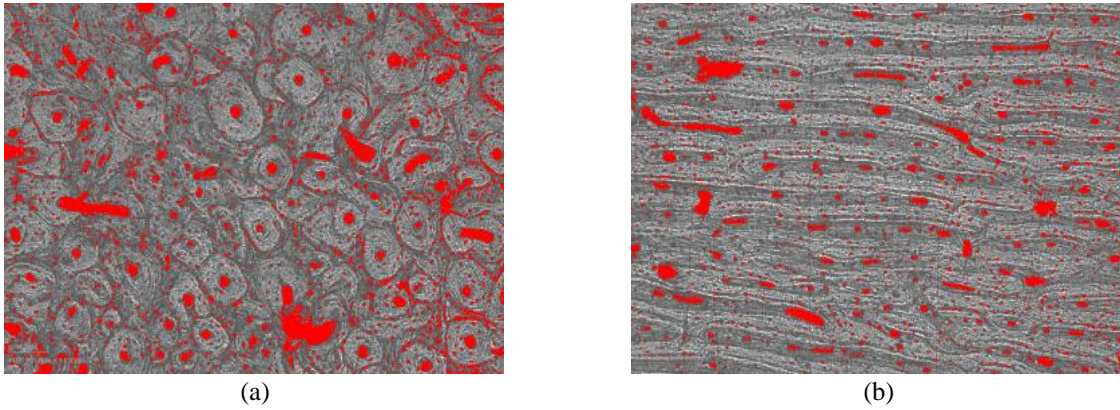


**Figure 5.8: ImageJ analysis showing porosity area fraction ( $A_p$ ) values of 0.10 and 0.06 for typical (a) haversian, and (b) plexiform sample, respectively.**

To realistically account for the volume of material being removed during a cut, a modified probability factor ( $p'(t_0)$ ) that is defined as:

$$p'(t_0) = (1 - A_{\text{Porosity}}) * p(t_0), \quad (5.11)$$

where  $p(t_0)$  is the probability of encountering the workpiece material, based on the variations in the surface height and tool cutting edge. The lower and upper limits of  $(1 - A_{\text{Porosity}})$  based on the digital analysis data are chosen while multiplying with lower and upper limits of  $p(t_0)$  to

provide the lower and upper bounds for the modified probability factor  $p'(t_0)$ . Thus, after considering the microstructure interfaces, realistic tool-workpiece intersection, and the porosity, the final expression for the modified total AE signal power is written as:

$$\dot{E}_{\text{Modified}} = p'(t_0) * \dot{E}_{\text{Total}}', \quad (5.12)$$

where  $p'(t_0)$  is the modified probability factor, and  $\dot{E}_{\text{Total}}'$  is the total AE signal power considering the microstructure effects.

### 5.4 Model Calibration and Validation

Fig. 5.9 depicts the overall model calculation, calibration, and validation process involving Eq. 5.1-5.12. As seen, the AE model has coefficients ( $C_1, C_2, C_3$ ),  $\Psi_{\text{tool|DOC}}$ , and  $M$ , that need to be calibrated using experimental data.

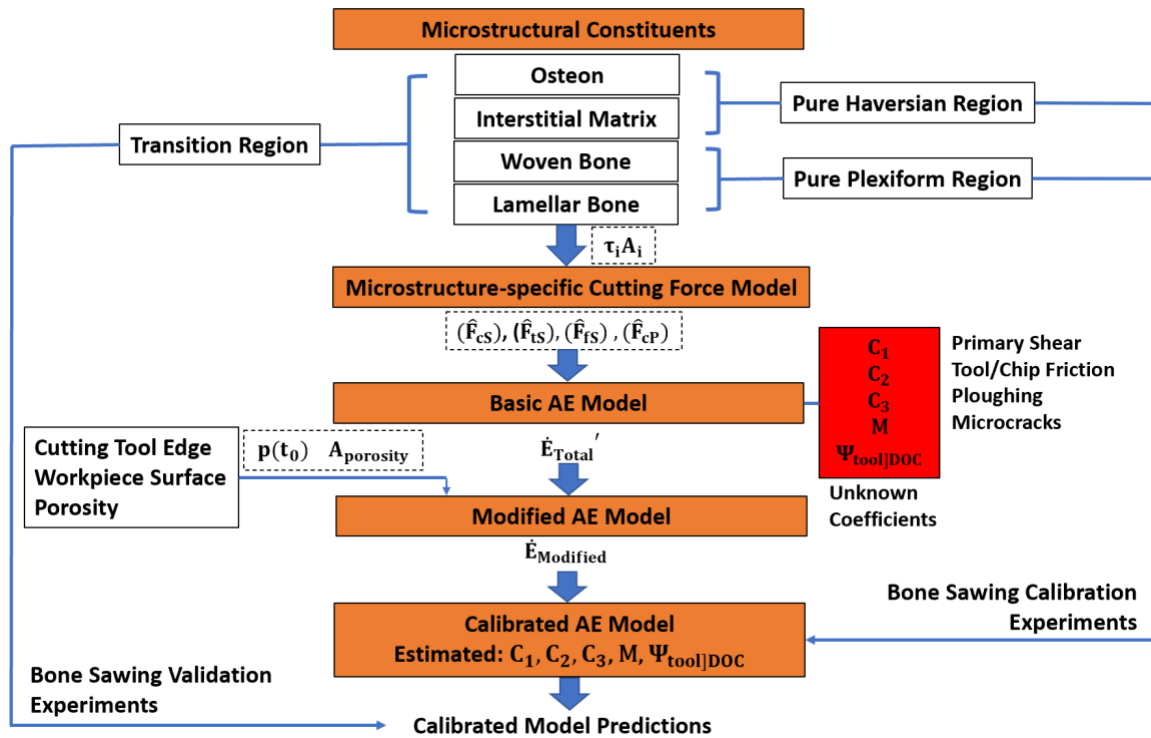


Figure 5.9: Overall model calculations, calibration, and validation process.

### 5.4.1 Estimation of Calibration Coefficients

Sawing studies from the pure haversian region (comprising of only osteons and interstitial matrix) and the pure plexiform region (comprising of only woven and lamellar bone) are used to calibrate for these coefficients. Based on the non-linear regression analysis of the experimental AE signal power and the calculated work rates, the calibration coefficients found as depicted in Table 5.3. It should be noted that  $\Psi_{\text{tool}|\text{DOC}}$  has three specific values each corresponding to the three wedges used.

**Table 5.3: Acoustic emission model calibration coefficients.**

$C_1$	0.47
$C_2$	0.89
$C_3$	0.22
$\Psi_{\text{tool} \text{DOC}}$	1.97E-4 at Low DOC
	2.00E-4 at Medium DOC
	0.77E-4 at High DOC
$M$	7.0E-6

### 5.4.2 Calibration Accuracy

As is the accepted practice in AE literature related to machining [30], [42], [43], [70], correlation is used as an approach for assessing the model predictions. Fig. 5.10(a)&(b) show the correlation plots indicating the accuracy of the calibration performed over the pure haversian and pure plexiform regions. Fig. 5.10(c)&(d) show the corresponding overlays of the calibrated model predictions (in black) over the experimental AE data (in red). Fig. 5.10(c)&(d) specifically show the lower and the upper limits of the spread seen in the experimental data and the model predictions.

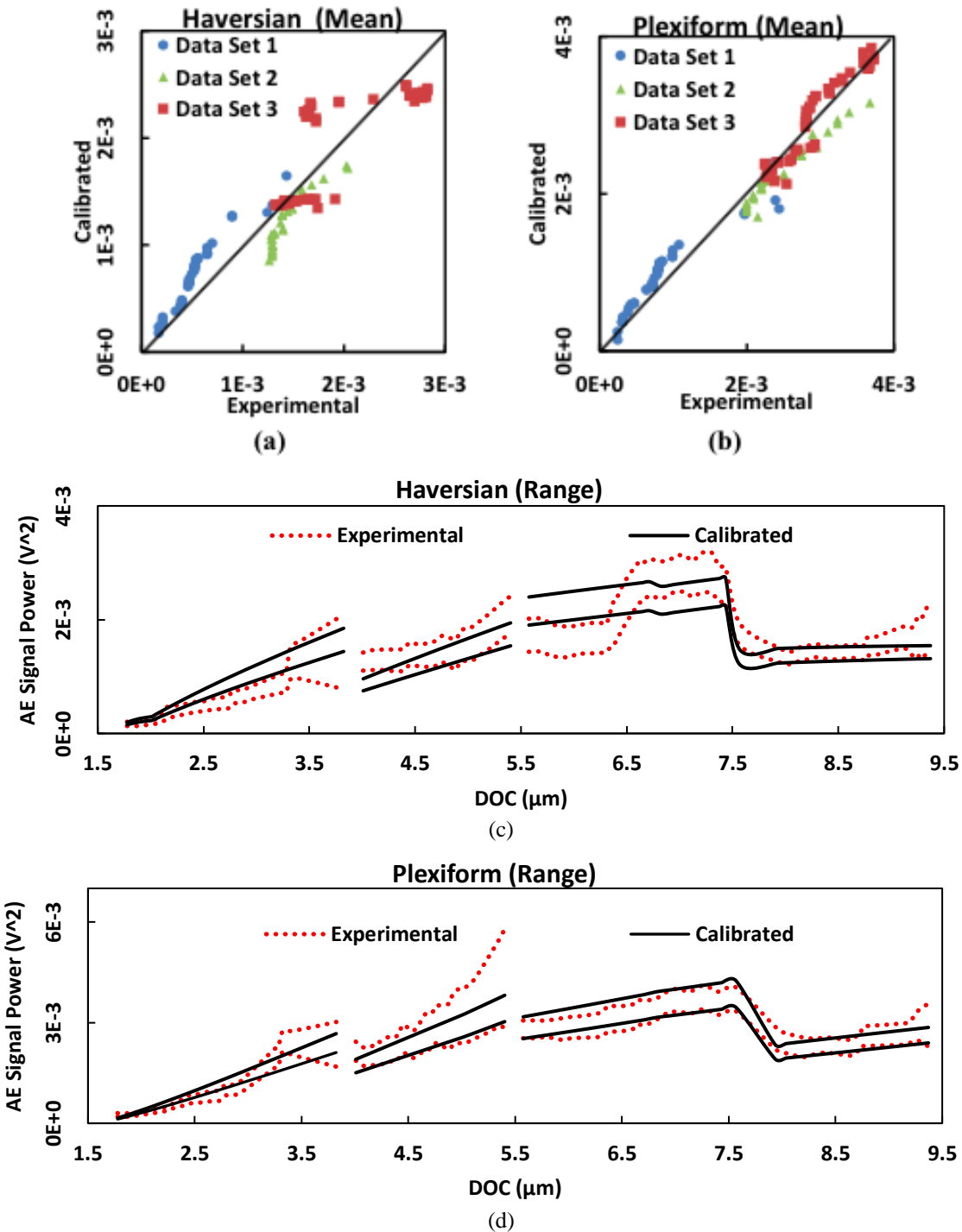


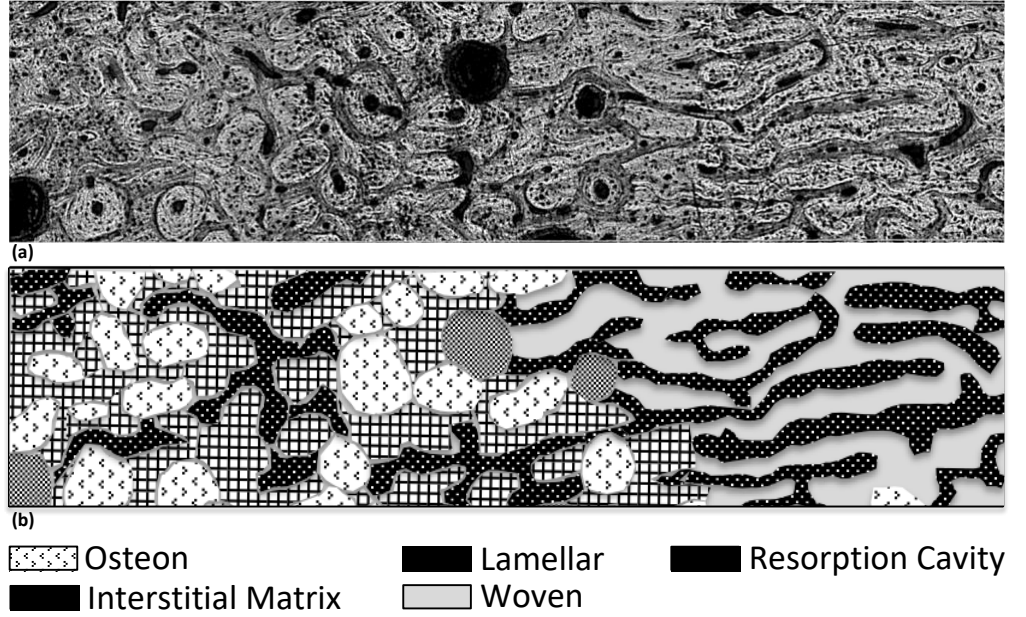
Figure 5.10: Calibration accuracy curves for acoustic emission prediction, in terms of the scatter of the Mean for (a) haversian and (b) plexiform regions, and the overlay of the Range against DOC for (c) haversian and (d) plexiform regions.

The correlation coefficients in the case of plexiform bone are 0.94, 0.98, and 0.96 for low, medium, and high DOCs, respectively. On the other hand, the correlation coefficients for the

haversian region are 0.95, 0.90, and 0.7 for low, medium, and high DOCs. In general, the correlation between the calibrated and the experimental AE signal power is lower for pure haversian region, especially at higher DOCs. This is seen in Fig. 5.10(c)&(d) that show the spread in the experimental data overlaid over the spread in the model predictions. For the pure haversian region, the AE model underperforms for the DOC values between 5.6. and 7.5  $\mu\text{m}$ , because of the non-linear hump seen in the AE experimental data that is not captured by the model. This hump is absent in the corresponding regions for the pure plexiform data (Fig. 5.10(d)). This difference in the performance of the model between the pure haversian and plexiform regions can be explained by the possibility of more localized microstructural property variations in the haversian region that affects the AE signal. For instance, Conward and Samuel [4] showed that the osteon and interstitial matrix regions in pure haversian regions exhibit higher variations in elastic moduli and hardness than the woven and lamellar regions in plexiform. The same research also showed that the osteons in the haversian region also exhibit a wider range of dimensions than the planar woven/lamellar layers in the pure plexiform region. It is possible that while these variations are not affecting the cutting force predictions, they affect the AE generation and subsequent transmission efficiencies to the tool-mounted sensor.

### **5.4.3 Model Validation**

As shown in Fig. 5.11, the experimental AE data from the transition region containing all four of the microstructural constituents, osteon, matrix, lamellar bone, and woven bone, is used for validating the model. Fig. 5.11 shows a map of the transition region, including the constituent area fractions  $A_i$  of the microstructures.



Data Set	DOC	Osteon	Matrix	Lamellar	Woven
1	Low	0.17	0.19	0.30	0.34
2	Medium	0.18	0.27	0.30	0.25
3	High	0.17	0.39	0.22	0.22

(c) **Figure 5.11: Transition region characterization map, (a) original image, (b) processed image, and (c) area fractions ( $A_i$ ) across multiple maps. [Refer Conward [5]]**

The calibration coefficients from Table 5.3 ( $\Psi_{\text{tool|DOC}}, C_1, C_2, C_3$ ) combined with the cutting force and shear stress predictions from the prior cutting force model [5], were used to predict the AE signal power in the transition region. Fig. 5.12 depicts the prediction accuracy curve for the three transition regions at various DOCs. It can be seen that there is a strong correlation at lower DOCs, but similar to the haversian region, the model underperforms in the regions of 5.6  $\mu\text{m}$ -7.5  $\mu\text{m}$  DOC. From Fig. 5.11, it can be seen that the percentage of osteon and matrix component is higher (56%) in the data set 3, which also corresponds to the high DOC. As such, the prediction response of the transition region in that data set is more in line with the calibration accuracy of the haversian region. The correlation coefficients thus obtained are 0.92, 0.95, and 0.8 for low, medium, and high DOCs, showing the model can capture the trend in the underlying data.

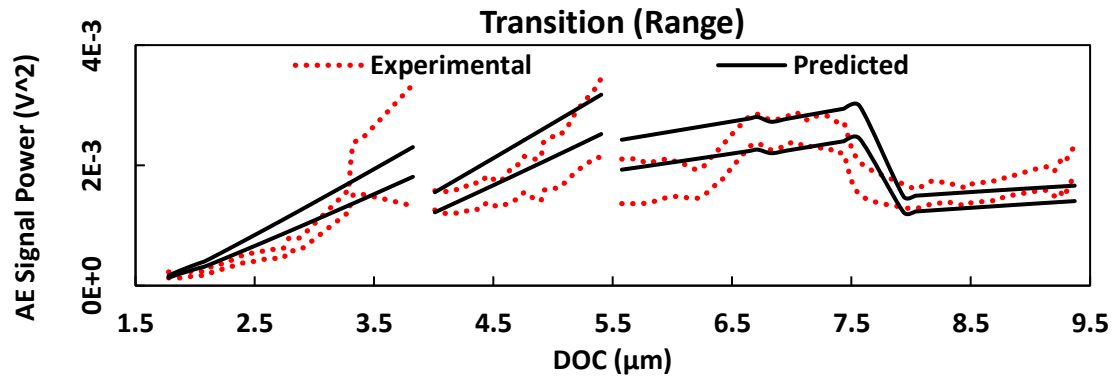


Figure 5.12: Acoustic emission model validation in terms of the overlay of the Range against DOC for the transition region.

One limitation of this model is that prior knowledge of all the microstructural components and their mechanical properties is needed as input to the model. As shown by Conward [5], these properties may be specific to the cross-section being investigated.

## 5.5 Model Uses for Process Planning

The AE model in its current form has application in process planning related to bone sawing. Two examples are considered here: (i) predicting the cutting force variations and (ii) predicting AE trends based on the microstructural components across various regions of the bone.

### 5.5.1 Predicting Cutting Force Variation

The force model by Conward [5] only predicted the mean value of the cutting force and the thrust force and did not consider the spread in the experimental data. The approach for estimating the probability of material being cut, which helped in predicting the spread in the AE data could also be applied to the cutting/thrust forces predictions from Conward [5].

Fig. 5.13 shows the measured cutting and thrust forces in the haversian region along with the predicted range based on the modeled forces. This predicted range was obtained by multiplying the range-to-mean ratio of  $p'(t_0)$  (from Eq. 5.11) to the predicted force value. It can be seen from

Fig. 5.13 that most measured cutting/thrust force values lie within the predicted range, showing the effectiveness of modeling the variation in the data.

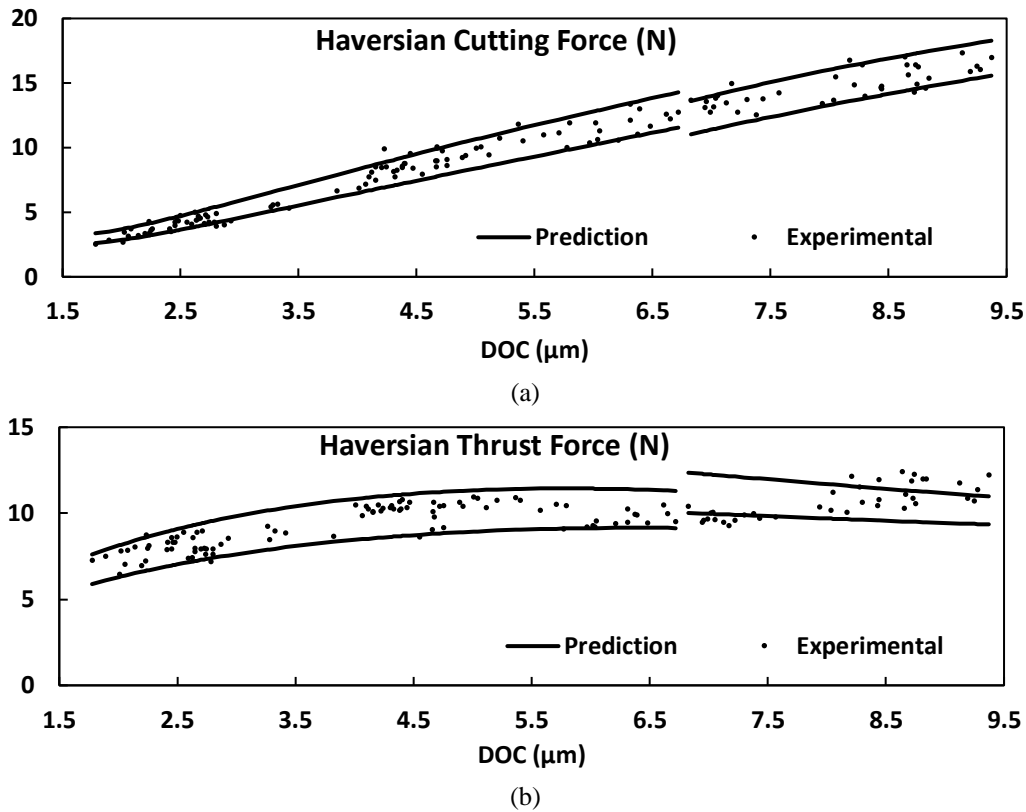


Figure 5.13: (a) Cutting force, and (b) thrust force range predictions based on the modeled force [5].

### 5.5.2 Predicting Region-specific Variations

The bovine cortical bone in the mid-diaphysis can be divided into four quadrants [5]. These regions vary by the fractions of haversian and plexiform bone within them. From a process planning standpoint, the model can be used to study the differences in the average AE signal power across these different regions. The cortical bone regions used in this experimental study were harvested from the medial and lateral regions of this quadrant due to the presence of a clear transition region between the plexiform and haversian components [5]. However, say for the same cross-section and cutting conditions, one was also interested in estimating the AE signal power observed while cutting through the posterior region of the quadrant, which is composed of 70%

haversian and 30% plexiform regions [17]. Such an estimate can be obtained using the weighted average of the AE signal powers calibrated on the pure haversian and pure plexiform regions. Fig. 5.14(b) shows a plot of the AE signal power thus calculated in the posterior region of the cortical bone.

Also included in Fig. 5.14(b) is a plot of the AE signal calculated in the cancellous region. Cancellous bone with its inherently high porosity of 65% to 82% [128], provides another opportunity for assessing AE suitability for process planning purposes. As seen in Fig. 5.14(a), this is the spongy bone that is encountered after the saw cuts through the cortical bone. The cancellous bone is similar in property to the interstitial matrix in cortical bone [129]. For calculating the AE signal power in the cancellous region, only the contribution of the interstitial matrix is considered (i.e., 100% interstitial matrix) along with a porosity estimate of 75%.

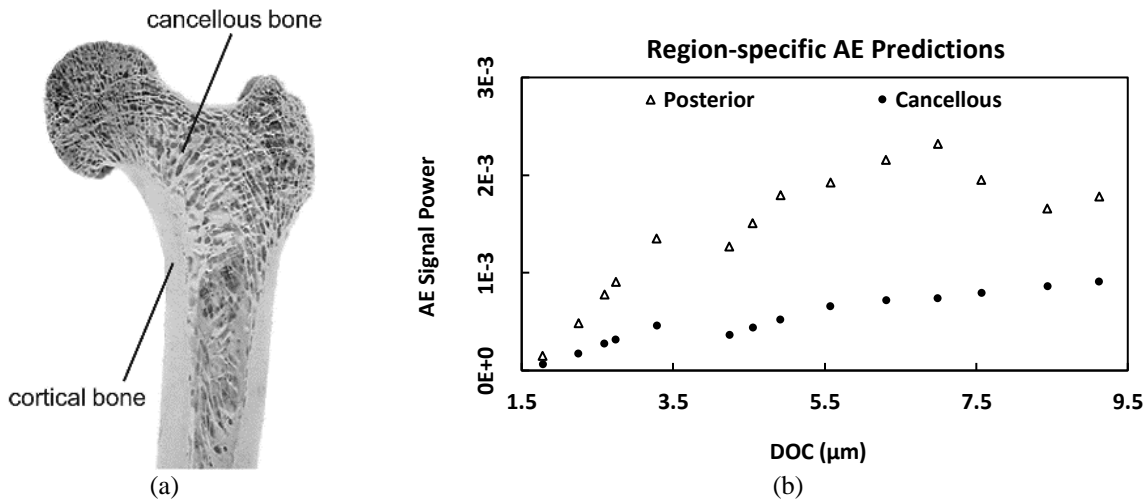


**Figure 5.14: (a) Image showing cancellous bone alongside cortical bone [130], and (b) the AE signal power predicted in the posterior region of the cortical bone, and the cancellous bone. [Note: For the cancellous bone,  $n = 0$  in Eq. 5.10]**

From the plots in Fig. 5.14(b), it is clear that cancellous bone results in significantly lower AE signal power predictions. The difference between the cortical bone and cancellous bone predictions can be used to estimate the transition of the bone saw from one bone type to the other.

This is also evidenced in the literature associated with bone drilling where AE signatures are shown to be very different for the cortical and cancellous regions [53].

## 5.6 Conclusions

The following specific conclusions can be drawn from this study:

1. This study presents an approach to model the AE signal power as a function of the specific cortical bone microstructures and the depth of cut encountered by the bone-saw tooth.
2. Using the cutting force predictions from Conward [5] as input, the AE signal power is modeled based on the energies dissipated in the shearing and ploughing zones encountered by the rounded cutting edge. For this calculation, the rounded edge geometry of the sawtooth is modeled as a combination of (i) shear-based cutting from a negative rake cutting tool and (ii) ploughing deformation from a round-nose indenter.
3. The spread seen in the AE signal power is captured by modeling the variations in the sawed surface height profile, the tool cutting edge geometry, and the porosity of the bone.
4. The AE model is first calibrated on the pure haversian and pure plexiform regions of the bovine cortical bone and then validated on the transition region containing mixed haversian and plexiform microstructures. The model shows a good correlation ( $>0.9$ ) between the predicted and experimentally measured AE signal power.
5. The validated AE model is useful for process planning both in terms of its ability to predict trends in AE signal power and cutting force variations, based on the differences in the underlying bone microstructures.

## **6. A MULTI-SENSOR MODALITY TO MONITOR BULK HYDROGEL GELATION**

During the 3D printing of hydrogels, it is important to monitor the stiffness, or conversely the gel-state of the part [6], [117], [131], [132]. This is especially critical to ensure the structural integrity of the printed hydrogel. While there are techniques to monitor the gelation process [7], [112], [114], [118], [133], these technologies are limited in their applicability to 3D printing due to their high cost and their process-integration challenges. The study presented in this Chapter is part of Thrust 3 research efforts and focuses on exploring a low-cost, multi-sensor modality to monitor bulk hydrogel gelation, with an eye towards its eventual deployment in 3D printing environments.

This study will test the hypothesis that a combination of digital images and acoustic pressure signals can be used to estimate the gel-state of a bulk hydrogel sample. A hydrophone will be used to measure the acoustic waves generated in the sample by an external, low-impact energy source. Also, a digital camera will be used to obtain information about the image intensity as the gelation causes the hydrogel to change from a transparent to an opaque. These two signals will be combined to obtain a gel-state estimate.

The scope of this work is limited to hydrogel constructs (of varying thickness) that are subjected to thermo-reversible gelation. Furthermore, this work will not explicitly account for the effect of varying thermal boundary conditions.

The remainder of this chapter is divided into the following sections: Section 6.1 presents, the experiment testbed development, along with the approach of estimating the gel-state based on the hydrophone and the image intensity readings. Finally, Section 6.2 presents the summary and the limitations of this approach.

## 6.1 Experiment Testbed

The hydrogel used in this study is an aqueous solution of agarose, 1% by weight. Agarose undergoes thermo-reversible gelation [23], [24], [26]. This solution is in its gel state at room temperature whereas at temperatures above 70 °C it transforms into its solution state. The experiments involve a warm hydrogel solution (70-75 °C) of specified thickness, gelling at room temperature, while the multi-sensor modalities are in operation to monitor the progress of gelation.

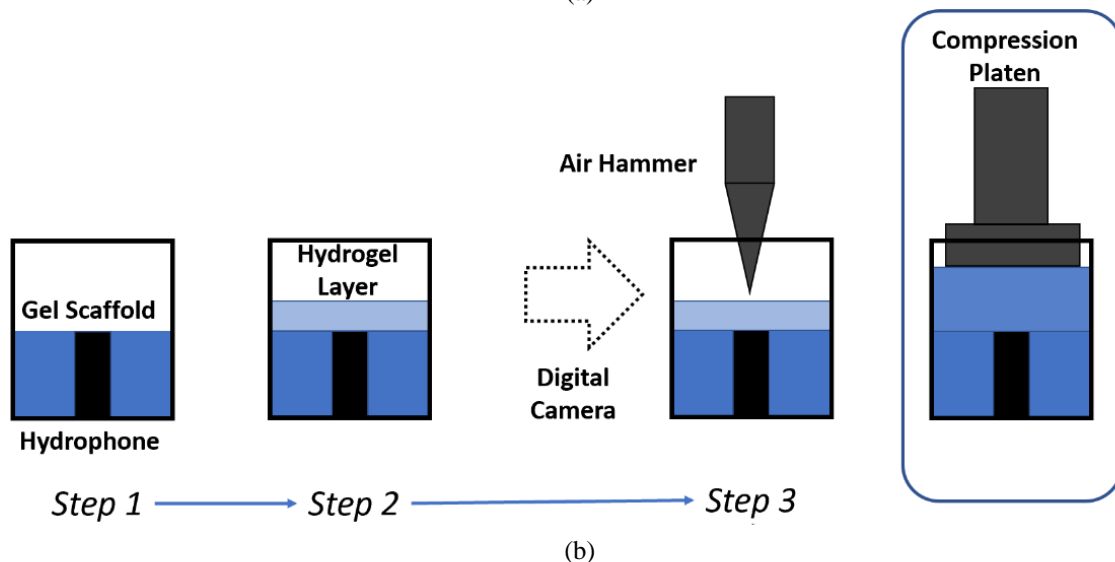
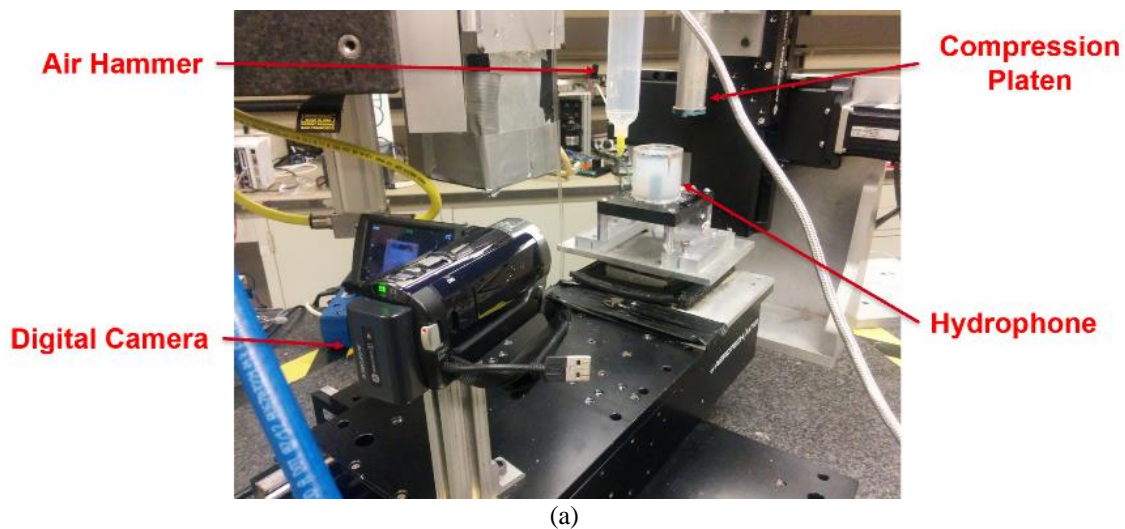


Figure 6.1: (a) Photo of the experiment setup, and (b) a schematic of the steps involved in the experiments.

Fig. 6.1 shows the picture of the experimental setup as well as the steps involved in the experiments. The container for housing the agarose solution during the experiments is an acrylic cylinder of outer diameter 51 mm, wall thickness 7 mm, and a height of 50 mm. The hydrophone BK-8103 (frequency range of 0.1 Hz to 180 KHz) is placed in the center of the container and is embedded in a fully gelled hydrogel casing located at the bottom of the during the experiment. The hydrophone signal is sampled at the rate of 20 KHz based on early-stage experiments that confirmed that only frequency events ( $< 1$  KHz) were critical to the present study. In addition to the hydrophone, a Sony HDR- CX160 digital camera is used as a second sensing modality to monitor the gelation progress. It is known that as the hydrogel changes from solution to a gel state, it changes from being transparent to opaque [134]–[136]. Thus, monitoring the image intensity of the hydrogel will provide additional insight into the gelation process. The transparent nature of the acrylic container housing the hydrogel also helps in the implementation of this second sensing modality.

Table 6.1 lists the various layer thickness values explored in this study. The maximum sample thickness was selected to be comparable with hydrogel constructs in the literature [9]. The minimum thickness selected was due to the experiment constraint, especially the need to obtain good discernible images by the digital camera.

**Table 6.1: Sample thicknesses considered in this study.**

<b>L (mm)</b>	2.5	5	10	20
---------------	-----	---	----	----

The gelation chamber is mounted on Aerotech motion stages that move the hydrogel sample relative to (i) an air-hammer, and (ii) a compression platen. The air hammer acts as an external source of the incident pressure waves on the hydrogel. It consists of a syringe with a 20-gauge dispensing nozzle through which a controlled pressurized air (5 – 50 psi) is blown intermittently (every 30 s) for short durations (0.1 s) at the top of the hydrogel sample so that the

pressure waves generated there, travel through the sample before reaching the hydrophone. The values for the air pressure and the duration of the air-hammer use were determined through early-stage experiments such that while they were sufficient to generate pressure waves in the hydrogel that are sensitive enough to be picked up by the hydrophone, while also not interfering with the integrity of the hydrogel samples. The protocol implied that the air pressure used for the air-hammer was also adjusted, based on the hydrogel thickness, with higher pressure values being used for thicker samples. It should be noted that this change in the air pressure does not affect the hydrophone signal metric used in this study, viz. the ‘change in attenuation coefficient’.

The compression platen consists of a cylindrical rod made of aluminum with a diameter about 2 mm smaller than the inner diameter of the acrylic cylinder housing the hydrophone and the hydrogel sample. The compression platen is attached to a Kistler 9256C1 dynamometer mounted on one of the Aerotech stages. At specific instances in the experimentation cycle, the compression platen is moved slowly at a rate of 1 mm/min while compressing the hydrogel sample up to 10% strain to measure the force and calculate the elastic stiffness. The motion profile was dictated by similar tests found in the literature [137], [138]. It should be noted here that this modality was only deployed for the 20 mm thick sample since it is difficult to implement for thinner samples without damaging the sample that is being studied.

The protocol for the experiments consists of the following steps as shown in Fig. 6.1 (b):

1. The hydrophone is first encased in a fully gelled hydrogel layer that spans the entire height of the sensor.
2. A warm solution (70 – 75 °C) of the hydrogel is poured to the desired thickness as per Table 6.1.

- As this sample gels at room temperature, the air-hammer blows air for the duration of 0.1 s every 30 s throughout the experiment duration of 30 mins. During this time both the hydrophone as well as the digital camera are used for continuously collecting data related to the acoustic pressure waves, and gelation grayscale, respectively.

### 6.1.1 Hydrogel Signal Characterization

A typical signal from the hydrophone is shown in Fig. 6.2 showing the bursts corresponding to the air-hammer operation. As mentioned, the air-hammer is in operation for 0.1 s every 30s.

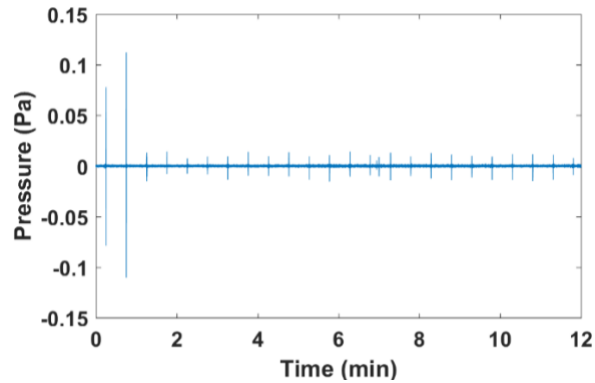


**Figure 6.2: Hydrophone signal for gelation of a 2.5 mm thick sample, showing the multiple bursts caused by the ‘air hammer’ application.**

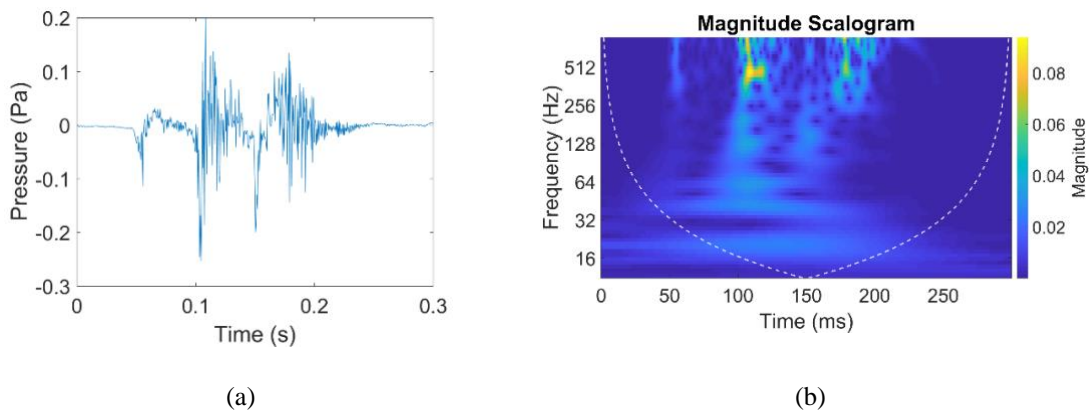


**Figure 6.3: (a) Typical hydrophone signal burst due to ‘air hammer’ application, and (b) a scalogram of the signal burst showing dominant frequency components around 400 Hz.**

Looking into a typical hydrophone signal burst caused by the air-hammer, it can be seen from the scalogram generated using Matlab™ that the frequency components lie around 400 Hz. Fig. 6.3 shows a typical hydrophone signal burst and its corresponding scalogram.

The hydrophone signal parameter considered is the 'change in attenuation coefficient' [139]–[144], as attenuation is a measure of the physical nature of the material through which the pressure wave is propagating. Eq. 6.1 shows the approach for finding the change in attenuation coefficient:

$$\begin{aligned}
 d &= L, \\
 A &= A_0 e^{-\alpha f d}, \\
 \Delta\alpha_i &= \alpha_{i+1} - \alpha_i = \frac{\ln A_i - \ln A_{i+1}}{f d}, \tag{6.1}
 \end{aligned}$$

where 'd' is the distance traveled by the wave, 'L' is the sample thickness of the hydrogel, 'A' is the attenuated wave amplitude, 'A<sub>0</sub>' is the incident wave amplitude, 'α' is the attenuation coefficient, 'f' is the incident wave frequency, and 'i' refers to the instance. In the present study, the incident wave amplitude is the pressure used for the air hammer. The incident wave frequency of the hydrophone signals in the experiment was found to be around ~ 400 Hz (Fig. 6.3(b)). This frequency appears to be characteristic of the air blowing from the air-hammer used in this study. Therefore, a constant frequency value of 400 Hz was used in the calculations in this study. Finally, the distance traveled by the wave will be the hydrogel thickness as the air hammer nozzle is placed at the top surface and the hydrophone sensor is at the bottom surface of the hydrogel sample.

The hydrophone signal parameter is thus defined as the change in the attenuation coefficient:

$$S_1(t) = \Delta\alpha_i, \tag{6.2}$$

where S<sub>1</sub>(t) is the hydrophone signal parameter, Δα<sub>i</sub> is the instantaneous change in the attenuation

coefficient, and  $t$  is the time corresponding to the instance. Fig. 6.4 shows the plot of the change in attenuation coefficient for different samples.

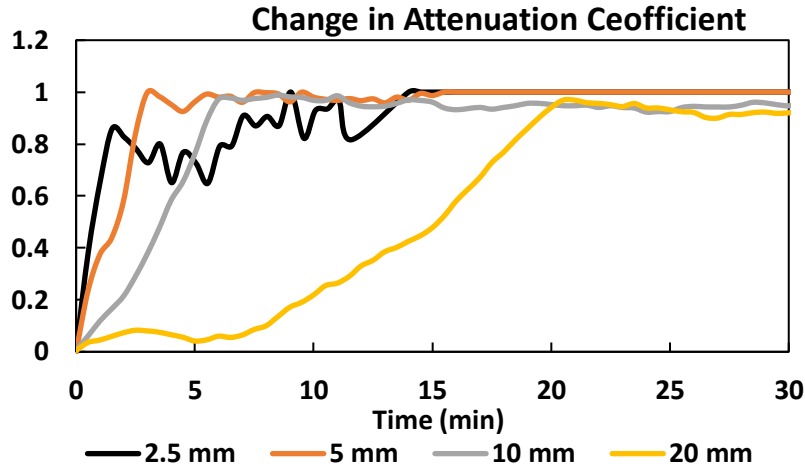


Figure 6.4: Change in attenuation coefficient from the hydrophone signals corresponding to different samples.

### 6.1.2 Digital Image Characterization

As a digital camera is also used as a sensing approach in this study,  $S_2(t)$  is defined as the image intensity parameter which is the image intensity found from the video stills using Matlab™. To obtain the image intensities, the video stills were converted to grayscale images and the mean gray values were found [145]–[147]. Fig. 6.5. shows the video stills of 20 mm agarose solution in solution state with a normalized image intensity of 0; fully gelled state with a normalized image intensity of 1.

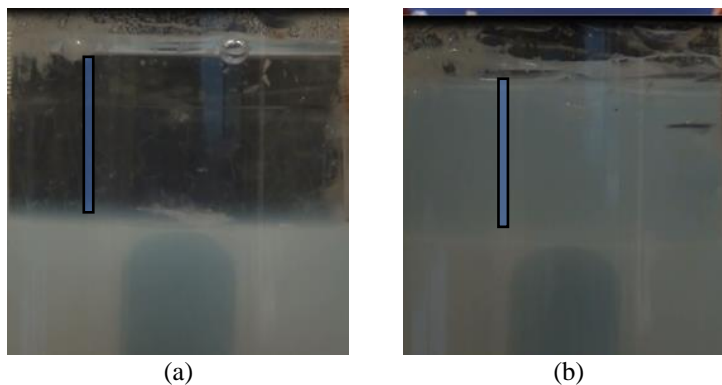


Figure 6.5: Video stills of a 20 mm thick layer at (a) 0 min, and (b) 100 min. [Note: The blue line shows the region where image intensity was calculated]

### 6.1.3 Multi-sensor Signal Metric

While both the hydrophone signal and the image intensity values separately give a measure of the gel-state, it is important to combine the two signals to get a more balanced insight into the gelation process. The hydrophone signal by its very nature will provide a localized measure of the gel-state based on the location of the hydrophone and the air-hammer along the centerline of the hydrogel sample. On the other hand, the image intensity from the video stills provides a more global insight into the gelation process as the image is not of a particular region of the sample but the whole sample as seen by the digital camera.

A unified expression for the gel state estimate to be used in this study is shown in Eq. 6.3. The expression considers the contribution of the hydrophone signal and the image intensity and uses a power-law relationship to arrive at the gel-state estimate since it is observed in the literature that the gel-state follows a power-law relation to material properties, e.g., shear modulus [11]. The expression for gel state estimate, thus established is:

$$\widehat{\Phi}_n(t) = \sum_{i=1}^2 a_i S_i^{b_i}(t) + c, \quad (6.3)$$

where  $t$  is the time,  $S_i$  refers to the signal of  $i$ -sensor, and  $a_i$ ,  $b_i$ ,  $c$  are the calibration constants.

### 6.1.4 Gel-state Estimate: Calibration, Indirect Validation, and Prediction

Fig. 6.6 shows a flowchart for finding the gel state estimate (Eq. 6.3) for the case of a 20 mm thick sample.

The gel temperature of 35 °C [8], [24], [26], [148], [149] is assumed to correspond to the time for the gel-state estimate to cross 0.5. For the case of the 20 mm thick sample, a thermocouple was used to record the temperature evolution during gelation (Fig. 6.6). The time needed to reach a temperature of 35 °C and consequently 0.5 gel state (as assumed in this study), is 18 min. This

time is denoted by  $t_L$ , i.e., the time needed for a sample of thickness  $L$  undergoing gelation at room temperature, to reach an assumed gel state of 0.5. Similar to the reason for employing the compression platen for the 20 mm sample case only, the thermocouple was also used for only this case as it was more suitable to implement considering the size of the sample. Smaller samples presented difficulties for implementing the thermocouple to get the temperature readings.

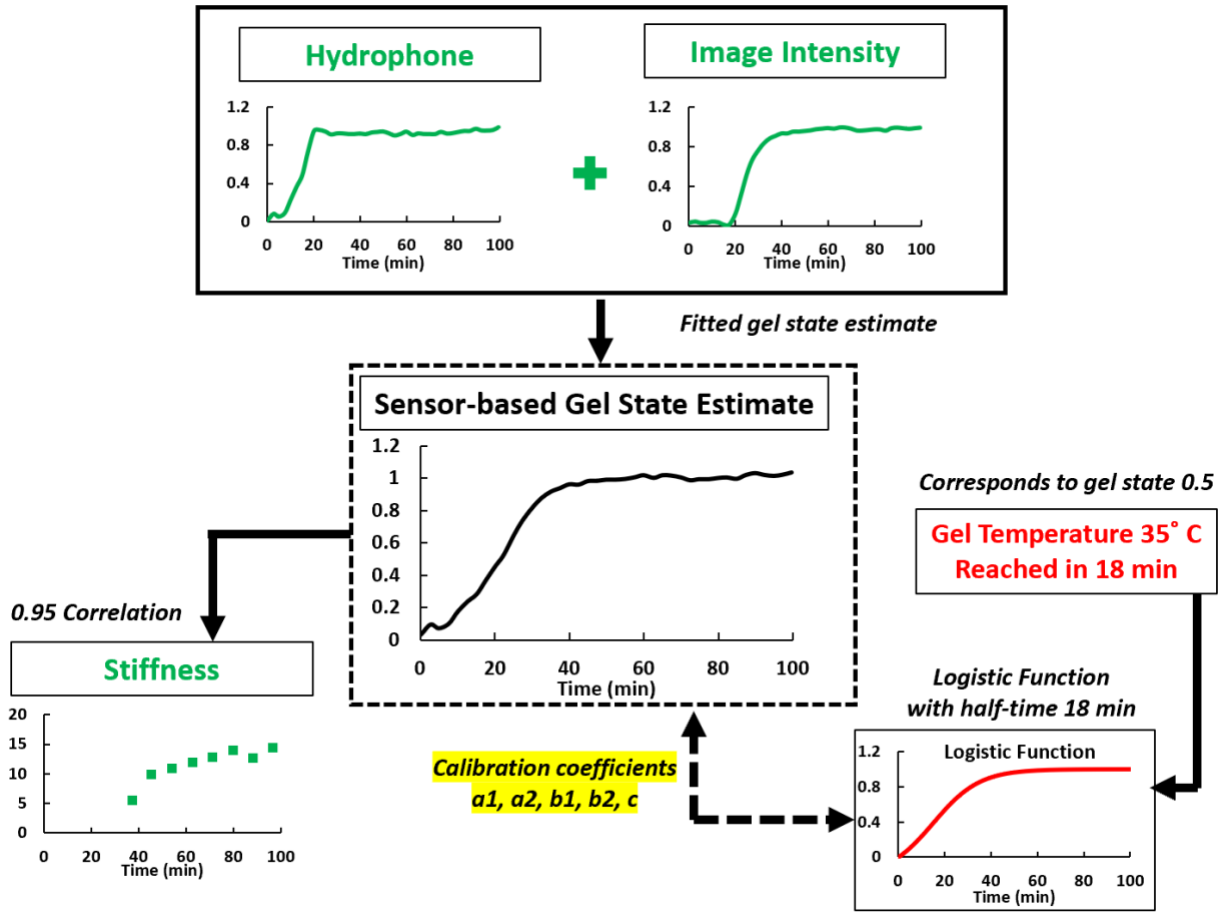


Figure 6.6: Flowchart for finding gel-state estimate in the case of a 20 mm sample.

Fig. 6.7 shows the evolution of the image intensity during the gelation process for the 20mm case. As marked on the plot, the time corresponding to a temperature of 35 °C also corresponds to the time there is a sharp rise in the image intensity of the sample. This relationship is suitable for estimating  $t_L$  values for samples with thicknesses  $< 20$  mm, where no thermal

histories are available. Using this relationship, based on the image intensities, the values for the other cases are shown in Table 6.2.

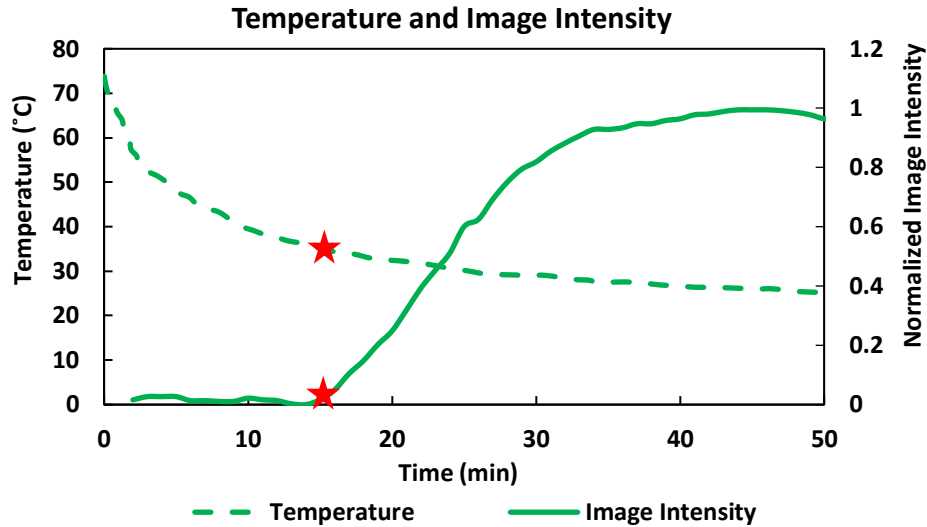


Figure 6.7: Temperature and image intensity evolution during the gelation of a 20 mm sample.

Table 6.2: The half-time value corresponding to sample thickness L.

L (mm)	2.5	5	10	20
$t_L$ (min)	1	2	8	18

The gelation is seen in literature to follow a logistic function [150]. Based on this knowledge, a logistic function is fitted to the sensor-based estimated gel state with a half-time corresponding to  $t_L$  provides for the calibration factors  $a_i$ ,  $b_i$ ,  $c$ . The calibration factors thus determined are shown in Table 6.3.

Table 6.3: Calibration constants.

a1	a2	b1	b2	c
0.44	0.60	0.67	1.59	0.01

From the calibration factors in Table 6.3, it can be seen that  $a_1$ ,  $b_1$  are smaller than  $a_2$ ,  $b_2$ . This shows that the contribution of the hydrophone signal is lower than the contribution of the image intensity. One reason may be the different nature of the sensors and their sensitivities vis-à-vis monitoring gelation. Another way of interpreting the findings is that the hydrophone signal is more localized in nature in the sense that the sensor and the ‘air hammer’ are located along the

centerline of the cylindrical hydrogel sensor and the wave propagation is along that direction only. Thus, in effect the hydrophone sensor signal is mostly affected by the gelation in the center of the hydrogel specimen. On the other hand, the image intensity of the hydrogel sample is a more globalized measure. Though the video stills are two-dimensional images, they still contain information about how the sample as a whole gradually changes from transparent to opaque as measured by the image intensity. As opposed to the hydrophone sensor, this is not a localized measure.

To validate the accuracy of these calibration factors, for the case of a 20 mm thick sample, the gel-state estimate was correlated with the stiffness measurements, as shown in Fig. 6.8. A correlation coefficient of 0.95 proves that the gel-state estimate is a good measure of the physical property of the hydrogel at least for the time when the stiffness is probed. It should be noted that this is only an indirect validation of the gel-estimate metric and as such, the use of sensitive stiffness measurement modalities will be needed to capture the stiffness variation in the time domains  $< 40$  min.

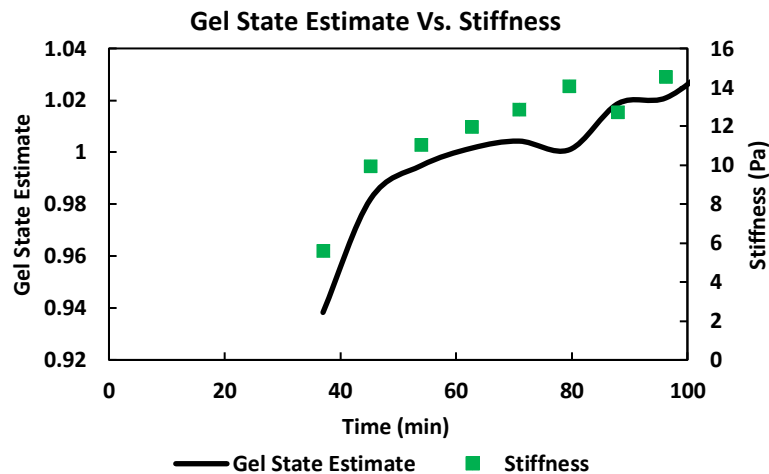


**Figure 6.8:** Comparison of gel-state estimate with stiffness in a 20 mm thick sample.

The gel state estimates thus calculated from Eq. 6.3 for the different sample thicknesses are shown in Fig. 6.9. As expected, it can be seen that the curves are different for the different

sample thickness values and that the gel state estimate of 1 is reached faster for samples with lower thickness values.

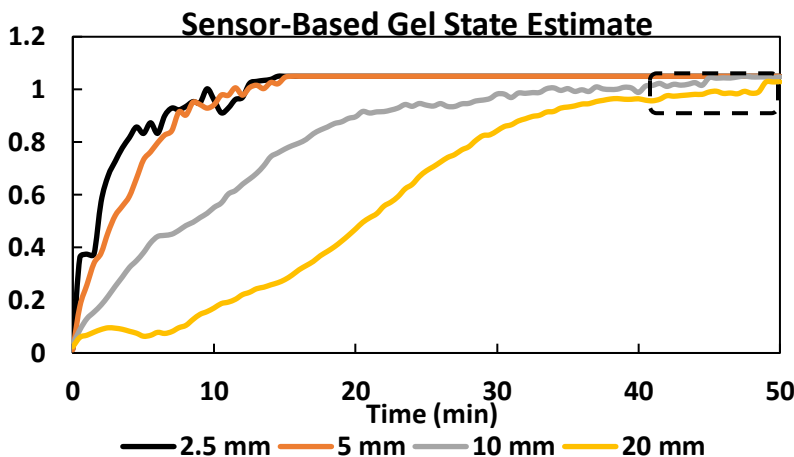


Figure 6.9: Estimated gel-states for different sample thicknesses. [Note: validation is done beyond 40 min for the 20 mm thick layer, as shown by the dashed box]

## 6.2 Summary and Limitations

The hypothesis that a combination of digital images and acoustic pressure signals can be used to estimate the gel-state of a bulk hydrogel sample has been successfully tested. In this multi-sensor modality, a hydrophone is used to collect acoustic waves generated in the sample by an external, low-impact energy source. Also, a digital camera is used to get information about the image intensity as the gelation causes the hydrogel to change from transparent to opaque. The two signals are then combined to obtain a gel-state estimate. This modality holds the promise of being implementable in a hydrogel 3D printing environment.

While this study provides a practical approach to estimating the gel-state in an agarose hydrogel there are certain limitations of the work:

1. The gel-state estimate predicted in this study should be validated using chemical sensing modalities that can accurately confirm the gel-state of the sample. Without such an external validation, the accuracy of the prediction may be anecdotal.

2. The effects of thermal gradients should be investigated and included as part of the gel estimate.
3. A critical next step towards adaptation in 3D printing will be to investigate the effect of layer-by-layer printing on this multi-sensor gel-estimate.

## 7. CONCLUSIONS AND RECOMMENDATIONS

The overall objective of this research is to explore the effectiveness of using acoustic sensing modalities to monitor manufacturing processes involving two classes of biomaterials, viz. hard biomaterials (bovine bone), and soft biomaterials (tissue-mimicking hydrogel). To achieve this objective, research efforts were focused on the following three thrusts:

- **Thrust 1- Hard biomaterial: Fracture-dominant cutting of bovine bone:** On this front, the work involved the use of AE signals to distinguish the microstructure-specific failure mechanisms encountered during the fracture-cutting of bone. Machining experiments were conducted under conditions that induce fracture-dominant failures. Cutting forces and AE signals were correlated to specific failure mechanisms observed using high-speed imaging. The work enabled the development of AE signal metrics to identify specific fracture-related failures in the bovine bone.
- **Thrust 2- Hard biomaterial: Shear-dominant cutting (sawing) of bovine bone:** This study involved modeling of the AE signal power trends, as a function of the specific cortical bone microstructures and the depth of cut encountered by the sawtooth. The AE response was modeled based on the cutting energy dissipation as well as the microstructural features. The model was first calibrated on the pure haversian and plexiform regions of the bovine cortical bone and then validated on the transition region containing both haversian and plexiform microstructures. The work was aimed at using AE signals for effective process planning in bone sawing.
- **Thrust 3- Soft biomaterial: Monitoring gelation in tissue-mimicking hydrogel:** The overarching objective of this thrust was to estimate the gel-state of the hydrogel construct using both acoustic signals and digital images. This work involved hydrogel constructs that are

subjected to thermo-reversible gelation. A hydrophone was used to measure acoustic waves generated in the sample by an external, low-impact energy source. A digital camera was also used to get information about the image intensity as the gelation causes the hydrogel to change from being transparent to opaque. The two signals were then be combined to get a gel-state estimate of the hydrogel. This effort was aimed at implementing gelation monitoring modalities during 3D printing of hydrogels.

## **7.1 Conclusions**

The specific conclusions from each of the three research thrust areas are summarized in this Section.

### **7.1.1 Acoustic Emission Analysis of Failure Mechanisms Encountered in Fracture-cutting of Bovine Bone**

Haversian and plexiform components of bovine bone were orthogonally machined at a depth of cut of 70  $\mu\text{m}$  to induce fracture-based cutting, and the force and AE responses of the failure mechanisms were studied. The following specific conclusions can be drawn from this work:

- With the aid of high-speed camera images, the dominant failure mechanisms in haversian and plexiform components of bone have been correlated with their corresponding AE signatures. In haversian bone, the dominant failure mechanisms are cement line, osteon, and interstitial matrix fractures. In plexiform bone, the dominant mechanisms are lamellar, woven, and transverse-lamellar fractures.
- The AE signal was transient and consisted of multiple ‘bursts’. These ‘bursts’ or waveforms were helpful in tracking the fracture process as the crack initiation and propagation, and the chip breakage were observed to result in AE waveforms.

- Typical AE signatures of the different mechanisms were established. Two metrics – (i) the number of AE bursts, and (ii) the ratio of maximum-to-minimum amplitude were used to effectively distinguish the AE responses of the different failure mechanisms.
- Acoustic energies were calculated, and it was observed that the failures in the haversian bone resulted in much higher energies than in the plexiform-0° bone. However, the trans-lamellar fracture in plexiform-90° bone results in acoustic energies comparable to haversian failure mechanisms. In haversian bone, the cement line results in lower acoustic energies than both osteon and interstitial matrix fractures, which have comparable acoustic energies.
- AE appears to be more sensitive than the cutting force in capturing the microstructure-specific failure modes observed during fracture cutting of bovine bone.

### **7.1.2 Microstructure-based Mechanistic Model for Bone Sawing: Acoustic Emission Signal Power Predictions**

The following specific conclusions can be drawn from this study:

- This study presents an approach to model the AE signal power as a function of the specific cortical bone microstructures and the depth of cut encountered by the bone-saw tooth.
- Using the cutting force predictions from Conward [5] as input, the AE signal power is modeled based on the energies dissipated in the shearing and ploughing zones encountered by the rounded cutting edge. For this calculation, the rounded edge geometry of the sawtooth is modeled as a combination of (i) shear-based cutting from a negative rake cutting tool and (ii) ploughing deformation from a round-nose indenter.
- The spread seen in the AE signal power is captured by modeling the variations in the sawed

surface height profile, the tool cutting edge geometry, and the porosity of the bone.

- The AE model is first calibrated on the pure haversian and pure plexiform regions of the bovine cortical bone and then validated on the transition region containing mixed haversian and plexiform microstructures. The model shows a good correlation ( $>0.9$ ) between the predicted and experimentally measured AE signal power.
- The validated AE model is useful for process planning both in terms of its ability to predict trends in AE signal power and cutting force variations, based on the differences in the underlying bone microstructures.

### **7.1.3 A Multi-sensor Modality to Monitor Bulk Hydrogel Gelation**

This effort successfully tested the hypothesis that a combination of digital images and acoustic pressure signals can be used to estimate the gel-state of a bulk hydrogel sample. In this multi-sensor modality, a hydrophone was used to measure acoustic waves generated in the sample by an external, low-impact energy source. A digital camera was also used to get information about the image intensity as the gelation causes the hydrogel to change from being transparent to opaque. The two signals were then combined to obtain a gel-state estimate. This modality holds the promise of being implementable in a hydrogel 3D printing environment.

## **7.2 Directions of Future Research**

Based on the conclusions from this research on AE-based monitoring of fracture and shear dominant cutting of bovine cortical bone, and gelation monitoring in agarose hydrogel, directions for future research can be identified. Broadly speaking, the following future research pathways are suggested:

### 7.2.1 Clinically-relevant Studies on Human Bone Specimens

While bovine bone has provided a viable alternative to the human bone in studying the different bone microstructures and their responses in different machining conditions, the logical next step in the research will be to conduct experiments with human bone specimens under clinically relevant conditions. Conward [5] also points to the need to study the microstructural failure mechanisms in human bone after understanding the responses of bovine bone under different machining conditions.

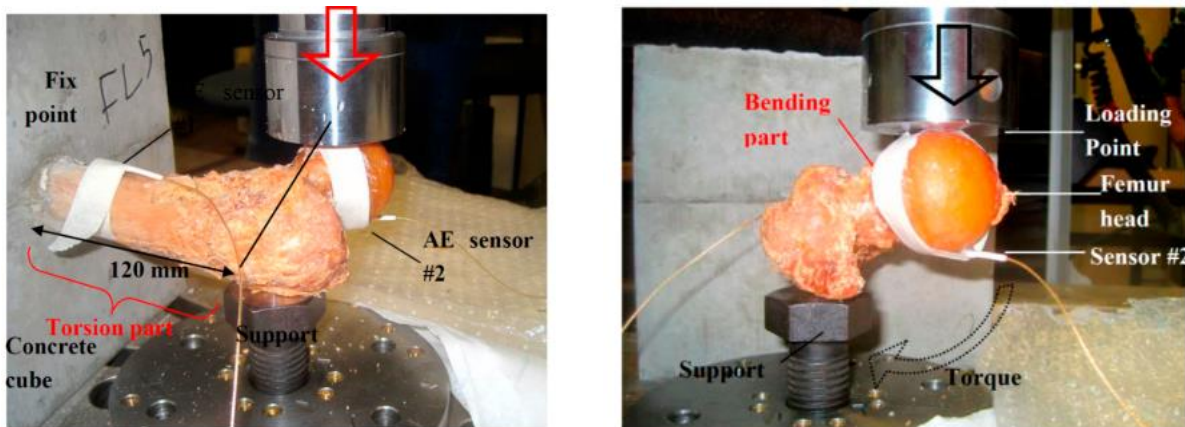


Figure 7.1: Acoustic emission-monitored fracture study on human femur bone [95].

Mechanical testing studies have been conducted on human bone specimens to understand the fracture process under different load conditions [90], [151]–[154]. In a particular study incorporating AE monitoring in fracture of the human femur bone under bending-torsion loads, Aggelis et al. [95] demonstrated the detection of micro-fracture onset using AE, in addition to discovering the differences in the AE signals corresponding to the bending at the femur neck and the torsion at the femur diaphysis region. Fig. 7.1 shows photos of the fracture test experiment conducted by Aggelis et al. [95] at two angles. These past material-testing studies are very beneficial in understanding and controlling the damage during bone surgeries, however, the field

will benefit immensely from the AE-based machining studies involving human bone , as described in this thesis.

### 7.2.2 Exploring Diverse and Realistic Bone Cutting Strategies

While the single-point cutting strategy of orthogonal machining has been widely used in studying bone response in machining due to the simplistic nature of the cutting process [20], [21], the actual bone surgeries often involve a variety of tools which complicate the cutting process [155]. Bone surgical approaches include a variety of cutting processes like milling, drilling, and sawing. Taking the example of bone sawing, Pearlman [155] mentions the broad classification of power saws used for surgical purposes – oscillating sagittal saw and reciprocating sternal saw. As shown in Fig. 7.2, these saws consist of multiple teeth and the cutting path can be an arc (sagittal arc) or linear (sternal saw). Also, the cutting direction alternates with each pass. For the implementation of a robust process monitoring approach, these factors also need to be accounted for in the sensing modality. Thus, the next step after AE monitoring of orthogonal fracture and shear-based studies is the implementation of AE in studies involving cutting strategies that closely resemble the actual bone surgery.

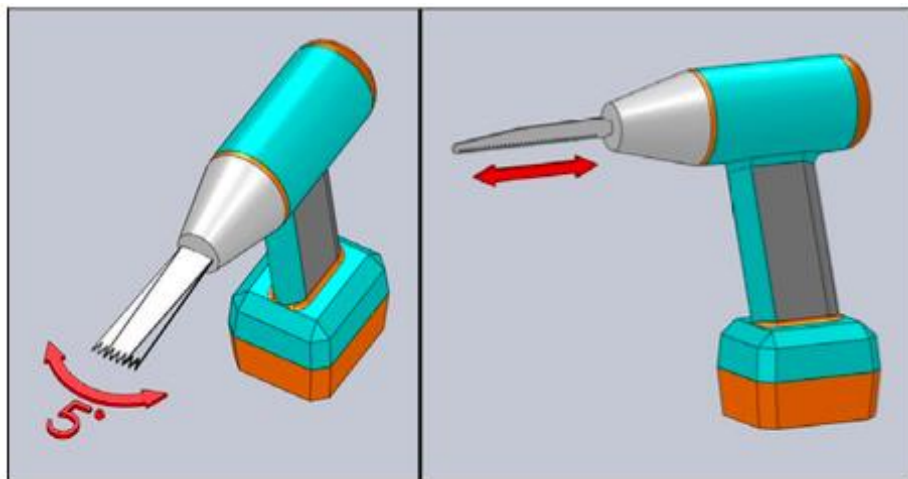


Figure 7.2: Sagittal (left), and sternal (right) saws [155].

### **7.2.3 Monitoring Failures in Heterogeneous Materials**

The effectiveness of the AE technique in monitoring the microstructure-specific fractures during the machining of the bovine cortical bone has applications in the machining of other heterogeneous material systems. Composite materials, specifically unidirectional fiber-reinforced composites, can benefit from the AE-based monitoring technique during machining. Also, the approach presented in developing the AE prediction model in bone sawing can be further explored in the machining of different composite materials.

### **7.2.4 Monitoring Layer-by-layer Hydrogel Printing**

In the case of a multi-sensory gel state estimate for hydrogel gelation, the next steps will involve layer-by-layer printing of hydrogel. While the proposed sensing approach has been shown to work well for bulk specimens of multiple thicknesses, a layer-by-layer printing involves additional complications that need to be addressed. For instance, it will become imperative to monitor the gelation in all the layers separately, in addition to the gross state of gelation in a multi-layered construct. The effect of layers on the gelation of the prior layers will also need to be studied as thermal and physical loads will act upon the layers. Lastly, the layer-by-layer printing studies may also incorporate thermal constraints to introduce gelation fronts in the hydrogel layers by the imposition of temperature gradients. A sensing modality capable of estimating the evolution of the gel front in the hydrogel layers could then be implemented in an actual 3D printing setup.

## REFERENCES

- [1] C. B. Scruby, “An introduction to acoustic emission,” *J. Phys. E: Sci. Instrum.*, vol. 20, pp. 946-953, Aug. 1987.
- [2] H. N. G. Wadley, C. B. Scruby, and J. H. Speake, “Acoustic emission for physical examination of metals,” *Int. Met. Rev.*, vol. 25, no. 1, pp. 41–64, 1980, doi: 10.1179/imtr.1980.25.1.41.
- [3] D. Dornfeld, “Application of acoustic emission techniques in manufacturing,” *NDT E Int.*, vol. 25, no. 6, pp. 259–269, Dec. 1992.
- [4] M. Conward and J. Samuel, “Machining characteristics of the haversian and plexiform components of bovine cortical bone,” *J. Mech. Behav. Biomed. Mater.*, vol. 60, pp. 525–534, Mar. 2016.
- [5] M. Conward, “Effects of haversian and plexiform components on the machining of bovine cortical bone,” Ph.D. dissertation, Mech. Eng., Rensselaer Poly. Inst., Troy, NY, USA, 2018.
- [6] P. Chiarelli, A. Lanatà, and M. Carbone, “Acoustic waves in hydrogels: A bi-phasic model for ultrasound tissue-mimicking phantom,” *Mater. Sci. Eng. C*, vol. 29, no. 3, pp. 899–907, Apr. 2009.
- [7] M. P. Brewin *et al.*, “Characterisation of elastic and acoustic properties of an agar-based tissue mimicking material,” *Ann. Biomed. Eng.*, vol. 43, no. 10, pp. 2587–2596, Mar. 2015.
- [8] S. Yadav, “Determination of thermal conductivity of tissue mimicking gel,” B.Tech. thesis, Dept. of Mech. Eng., N.I.T., Rourkela, India, 2013.
- [9] M. Hospodiuk, M. Dey, D. Sosnoski, and I. T. Ozbolat, “The bioink: A comprehensive review on bioprintable materials,” *Biotechnol. Adv.*, vol. 35, no. 2, pp. 217–239, Mar. 2017.
- [10] Y. Zhou, “The application of ultrasound in 3D bio-printing,” *Molecules*, vol. 21, no. 5, pp. 590-615, May 2016.
- [11] B. Zhou, Y. Heider, S. Ma, and B. Markert, “Phase-field-based modelling of the gelation process of biopolymer droplets in 3D bioprinting,” *Comput. Mech.*, vol. 63, no. 6, pp. 1187–1202, Jun. 2019.
- [12] B. Pokusaev *et al.*, “Thermokinetics and rheology of agarose gel applied to bioprinting technology,” *Therm. Sci.*, vol. 24, no. 1A, pp. 347-353, 2020, doi: 10.2298/TSCI191101453P.
- [13] T. P. James, J. J. Pearlman, and A. Saigal, “Predictive force model for haptic feedback in bone sawing,” *Med. Eng. Phys.*, vol. 35, no. 11, pp. 1638–1644, Jun. 2013.

- [14] J. J. Roberts, A. Earnshaw, V. L. Ferguson, and S. J. Bryant, “Comparative study of the viscoelastic mechanical behavior of agarose and poly(ethylene glycol) hydrogels,” *J. Biomed. Mater. Res. - Part B Appl. Biomater.*, vol. 99 B, no. 1, pp. 158–169, Jun. 2011.
- [15] I. S. Hage and R. F. Hamade, “Structural micro processing of haversian systems of a cortical bovine femur using optical stereomicroscope and MATLAB,” in *Proc. 2012 ASME Int. Mechanical Engineering Congr. & Expo.*, Houston, TX, USA, November 9-12, 2012, pp. 595-601.
- [16] M. Marco, M. Rodríguez-Millán, C. Santiuste, E. Giner, and M. H. Miguélez, “A review on recent advances in numerical modelling of bone cutting,” *J. Mech. Behav. Biomed. Mater.*, vol. 44. pp. 179–201, Apr. 2015.
- [17] J. H. Kim, M. Niinomi, T. Akahori, J. Takeda, and H. Toda, “Effect of microstructure on fatigue strength of bovine compact bones,” *JSME Int. J.*, vol. 48, no. 4, pp. 472–480, Apr. 2006.
- [18] B. Takabi and B. L. Tai, “A review of cutting mechanics and modeling techniques for biological materials,” *Med. Eng. Phys.*, vol. 45, pp. 1–14, Jul. 2017.
- [19] C. H. Jacob, J. T. Berry, M. H. Pope, and F. T. Hoaglund, “A study of the bone machining process-Drilling,” *J. Biomech.*, vol. 9, no. 5, pp. 131–136, 1976, doi: 10.1016/0021-9290(76)90056-7.
- [20] Z. Liao and D. A. Axinte, “On chip formation mechanism in orthogonal cutting of bone,” *Int. J. Mach. Tools Manuf.*, vol. 102, pp. 41–55, Mar. 2016.
- [21] A. Feldmann, P. Ganser, L. Nolte, and P. Zysset, “Orthogonal cutting of cortical bone: Temperature elevation and fracture toughness,” *Int. J. Mach. Tools Manuf.*, vol. 118–119, pp. 1–11, Aug. 2017.
- [22] K. L. Wiggins and S. Malkin, “Orthogonal machining of bone,” *J. Biomech. Eng.*, vol. 100, no. 3, pp. 122–130, Aug. 1978.
- [23] D. Nordqvist and T. A. Vilgis, “Rheological study of the gelation process of agarose-based solutions,” *Food Biophys.*, vol. 6, no. 4, pp. 450–460, May 2011.
- [24] E. Fernández, D. López, C. Mijangos, M. Duskova-Smrckova, M. Ilavsky, and K. Dusek, “Rheological and thermal properties of agarose aqueous solutions and hydrogels,” *J. Polym. Sci. Part B Polym. Phys.*, vol. 46, no. 3, pp. 322–328, Feb. 2008.
- [25] H. M. Pauly, L. W. Place, T. L. Haut Donahue, and M. J. Kipper, “Mechanical properties and cell compatibility of agarose hydrogels containing proteoglycan mimetic graft copolymers,” *Biomacromolecules*, vol. 18, no. 7, pp. 2220–2229, Jun. 2017.
- [26] V. Normand, D. L. Lootens, E. Amici, K. P. Plucknett, and P. Aymard, “New insight into agarose gel mechanical properties,” *Biomacromolecules*, vol. 1, no. 4, pp. 730–738, Nov. 2000.

- [27] Z. H. Mohammed, M. W. N. Hember, R. K. Richardson, and E. R. Morris, “Kinetic and equilibrium processes in the formation and melting of agarose gels,” *Carbohydr. Polym.*, vol. 36, no. 1, pp. 15–26, May 1998.
- [28] Z. Wang *et al.*, “In situ observation of sol-gel transition of agarose aqueous solution by fluorescence measurement,” *Int. J. Biol. Macromol.*, vol. 112, pp. 803–808, Jun. 2018.
- [29] D. G. Eitzen and H. N. G. Wadley, “Acoustic emission: Establishing the fundamentals,” *J. Res. Natl. Bur. Stand. (1934).*, vol. 89, no. 1, pp. 75–100, Jan. 1984.
- [30] D. A. Dornfeld and E. Kannatey-Asibu, “Acoustic emission during orthogonal metal cutting,” *Int. J. Mech. Sci.*, vol. 22, no. 5, pp. 285–296, 1980, doi: 10.1016/0020-7403(80)90029-6.
- [31] H. Gaja, “Analysis and modeling of depth-of-cut during end milling of deposited material,” M.S. thesis, Missouri S&T, Rolla, USA, 2011.
- [32] A. Hase, M. Wada, T. Koga, and H. Mishina, “The relationship between acoustic emission signals and cutting phenomena in turning process,” *Int. J. Adv. Manuf. Technol.*, vol. 70, no. 5–8, pp. 947–955, Feb. 2014.
- [33] M. Fotouhi, P. Suwarta, M. Jalalvand, G. Czél, and M. R. Wisnom, “Acoustic emission monitoring of thin ply hybrid composites under repeated quasi-static tensile loading,” *FME Trans.*, vol. 46, no. 2, pp. 238–244, Jan. 2018.
- [34] C. Suresh Kumar, V. Arumugam, and C. Santulli, “Characterization of indentation damage resistance of hybrid composite laminates using acoustic emission monitoring,” *Compos. Part B Eng.*, vol. 111, pp. 165–178, Feb. 2017.
- [35] J. M. Griffin and F. Torres, “Dynamic precision control in single-grit scratch tests using acoustic emission signals,” *Int. J. Adv. Manuf. Technol.*, vol. 81, no. 5–8, pp. 935–953, May 2015.
- [36] E. N. Landis and L. Baillon, “Experiments to relate acoustic emission energy to fracture energy of concrete,” *J. Eng. Mech.*, vol. 128, no. 6, pp. 698–702, May 2002.
- [37] G. Michlmayr, D. Cohen, and D. Or, “Sources and characteristics of acoustic emissions from mechanically stressed geologic granular media - A review,” *Earth-Science Rev.*, vol. 112, no. 3–4, pp. 97–114, May 2012.
- [38] N. Zhu, C. Tanaka, T. Ohtani, and H. Usuki, “Automatic detection of a damaged cutting tool during machining I: Method to detect damaged bandsaw teeth during sawing,” *J. Wood Sci.*, vol. 46, no. 6, pp. 437–443, Dec. 2000.
- [39] H. Trebacz and A. Zdunek, “Three-point bending and acoustic emission study of adult rat femora after immobilization and free remobilization,” *J. Biomech.*, vol. 39, no. 2, pp. 237–245, 2006, doi: 10.1016/j.jbiomech.2004.10.040.
- [40] V. Perfileyev, I. Lapsker, A. Laikhtman, and L. Rapoport, “Scratching of copper and silicon: Acoustic emission analysis,” *Tribol. Lett.*, vol. 65, no. 1, Mar. 2017, Art. no. 24.

- [41] M. Shateri, M. Ghaib, D. Svecova, and D. Thomson, "On acoustic emission for damage detection and failure prediction in fiber reinforced polymer rods using pattern recognition analysis," *Smart Mater. Struct.*, vol. 26, no. 6, May 2017, Art. no. 065023.
- [42] S. Rangwala and D. Dornfeld, "A study of acoustic emission generated during orthogonal metal cutting-1: Energy analysis," *Int. J. Mech. Sci.*, vol. 33, no. 6, pp. 471–487, 1991, doi: 10.1016/0020-7403(91)90082-e.
- [43] Y.-J. Park, "A study of acoustic emissions in orthogonal cutting operations," M.Eng. thesis, Dept. of Mech. Eng., Univ. of Wollongong, Australia, 1995.
- [44] C. U. Grosse and M. Ohtsu, *Acoustic emission testing*, Berlin, DE: Springer, Berlin, Heidelberg, 2008.
- [45] F. Ning, H. Wang, W. Cong, and P. K. S. C. Fernando, "A mechanistic ultrasonic vibration amplitude model during rotary ultrasonic machining of CFRP composites," *Ultrasonics*, vol. 76, pp. 44-51, Apr. 2017.
- [46] M. Xiqing and X. Chuangwen, "Tool wear monitoring of acoustic emission signals from milling processes," in *Proc. 1st Int. Workshop Education Technology and Computer. Science*, Wuhan, Hubei, CN, 2009, pp. 431–435.
- [47] M. G. R. Sause and S. Richler, "Finite element modelling of cracks as acoustic emission sources," *J. Nondestruct. Eval.*, vol. 34, no. 1, pp. 1-13, Feb. 2015.
- [48] K. Asamene and M. Sundaresan, "Acoustic emission-based monitoring of surfaces subjected to friction," in *Proc. SPIE 8347*, Apr. 2012, doi: 10.1117/12.915446.
- [49] M. S. H. Bhuiyan, I. A. Choudhury, M. Dahari, Y. Nukman, and S. Z. Dawal, "Application of acoustic emission sensor to investigate the frequency of tool wear and plastic deformation in tool condition monitoring," *Meas. J. Int. Meas. Confed.*, vol. 92, pp. 208–217, Oct. 2016.
- [50] Y. B. Guo and S. C. Ammala, "Real-time acoustic emission monitoring for surface damage in hard machining," *Int. J. Mach. Tools Manuf.*, vol. 45, no. 14, pp. 1622–1627, Nov. 2005.
- [51] X. Zhuang and X. Yan, "Investigation of damage mechanisms in self-reinforced polyethylene composites by acoustic emission," *Compos. Sci. Technol.*, vol. 66, no. 3–4, pp. 444–449, Mar. 2006.
- [52] M. Saeedifar, M. Ahmadi Najafabadi, K. Mohammadi, M. Fotouhi, H. Hosseini Toudeshky, and R. Mohammadi, "Acoustic emission-based methodology to evaluate delamination crack growth under quasi-static and fatigue loading conditions," *J. Nondestruct. Eval.*, vol. 37, no. 1, pp. 1-32, 2018, doi: 10.1007/s10921-017-0454-0.
- [53] Z. Liao and D. A. Axinte, "On monitoring chip formation, penetration depth and cutting malfunctions in bone micro-drilling via acoustic emission," *J. Mater. Process. Technol.*, vol. 229, pp. 82-93, Mar. 2016.
- [54] S. T. S. Bukkapatnam, S. R. T. Kumara, and A. Lakhtakia, "Analysis of acoustic emission signals in machining," *J. Manuf. Sci. Eng.*, vol. 121, pp. 568–576, Nov. 1999.

- [55] C. Maradei, R. Piotrkowski, E. Serrano, and J. E. Ruzzante, “Acoustic emission signal analysis in machining processes using wavelet packets,” *Lat. Am. Appl. Res.*, vol. 33, no. 4, pp. 443–448, Oct. 2003.
- [56] C. L. Jiaa and D. A. Dornfeld, “Experimental studies of sliding friction and wear via acoustic emission signal analysis,” *Wear*, vol. 139, no. 2, pp. 403–424, Aug. 1990.
- [57] S. Rangwala and D. Dornfeld, “A study of acoustic emission generated during orthogonal metal cutting-2: Spectral analysis,” *Int. J. Mech. Sci.*, vol. 33, no. 6, pp. 489-499, 1991, doi: 10.1016/0020-7403(91)90083-F.
- [58] K. Hakiai, Y. Ishida, and T. Asano, “Monitoring droplet ejection and landing in electrospray with electric current and acoustic emission,” *Jpn. J. Appl. Phys.*, vol. 47, no. 4(1), pp. 2279–2284, Apr. 2008.
- [59] J. Voltaire, “Ink Film Splitting Acoustics in Offset Printing,” Ph.D. dissertation, Royal Inst. of Tech., Sweden, 2006.
- [60] J. Barry, G. Byrne, and D. Lennon, “Observations on chip formation and acoustic emission in machining Ti-6Al-4V alloy,” *Int. J. Mach. Tools Manuf.*, vol. 41, no. 7, pp. 1055–1070, May 2001.
- [61] J. Barry and G. Byrne, “Study on acoustic emission in machining hardened steels Part 1: acoustic emission during saw-tooth chip formation,” *Proc. Inst. Mech. Eng. Part B J. Eng. Manuf.*, vol. 215, no. 11, pp. 1549–1559, Nov. 2001.
- [62] J. Barry and G. Byrne, “Study on acoustic emission in machining hardened steels Part 2: Acoustic emission during continuous chip formation with a non-overlapping cutting arrangement,” *Proc. Inst. Mech. Eng.*, vol. 215, no. 11, pp. 1561-1570, Nov. 2001.
- [63] S. Cedergren, G. Petti, and G. Sjöberg, “On the influence of work material microstructure on chip formation, cutting forces and acoustic emission when machining Ti-6Al-4V,” *Procedia CIRP*, vol. 12, pp. 55-60, 2013, doi: 10.1016/j.procir.2013.09.011.
- [64] M. S. H. Bhuiyan, I. A. Choudhury, and Y. N. Nukman, “An innovative approach to monitor the chip formation effect on tool state using acoustic emission in turning,” *Int. J. Mach. Tools Manuf.*, vol. 58, pp. 19–28, Jul. 2012.
- [65] H. Arslan, A. O. Er, S. Orhan, and E. Aslan, “Tool condition monitoring in turning using statistical parameters of vibration signal,” *Int. J. Acoust. Vib.*, vol. 21, no. 4, pp. 371–378, Dec. 2016.
- [66] M. P. Gómez, A. M. Hey, J. E. Ruzzante, and C. E. D’Attellisc, “Tool wear evaluation in drilling by acoustic emission,” *Physics Procedia*, vol. 3, no. 1, pp. 819–825, Jan. 2010.
- [67] Z. W. Zhong, J. H. Zhou, and Y. N. Win, “Correlation analysis of cutting force and acoustic emission signals for tool condition monitoring,” in *2013 9th Asian Control Conf. (ASCC)*, Istanbul, TR, 2013, pp. 1-6, doi: 10.1109/ASCC.2013.6606333..

- [68] S. A. Niknam and V. Songmene, “Burr formation and correlation with cutting force and acoustic emission signals,” *Proc. Inst. Mech. Eng. Part B J. Eng. Manuf.*, vol. 231, no. 3, pp. 399–414, Feb. 2017.
- [69] X. Rimpault, J. F. Chatelain, J. E. Klemberg-Sapieha, and M. Balazinski, “Fractal analysis of cutting force and acoustic emission signals during CFRP machining,” *Procedia CIRP*, vol. 46, pp. 143–146, 2016, doi: 10.1016/j.procir.2016.03.171.
- [70] Y. Lee, A. K. Chang, and D. A. Dornfeld, “Acoustic emission monitoring for the diamond machining of oxygen-free high-conductivity copper,” *J. Mater. Process. Tech.*, vol. 127, no. 2, pp. 199–205, Sep. 2002.
- [71] M. A. Câmara, A. M. Abrão, J. C. Campos Rubio, G. C. D. Godoy, and B. S. Cordeiro, “Determination of the critical undeformed chip thickness in micromilling by means of the acoustic emission signal,” *Precis. Eng.*, vol. 46, pp. 377–382, Oct. 2016.
- [72] A. Oluwajobi and X. Chen, “Acoustic emission detection signals in the experimental validation of nanometric machining simulations,” In *13th Int. Conf. Tools*, Miskolc, Hungary, Mar. 2012, pp. 395-400.
- [73] L. E. A. Sanchez, J. F. G. Oliveira, and R. T. Coelho, “Detection of cracks in scratching tests in ceramic materials through acoustic emission,” *Proc. Inst. Mech. Eng. Part B J. Eng. Manuf.*, vol. 219, no. 9, pp. 685–693, Sep. 2005.
- [74] F. Torres and J. Griffin, “Control with micro precision in abrasive machining through the use of acoustic emission signals,” *Int. J. Precis. Eng. Manuf.*, vol. 16, no. 3, pp. 441–449, Mar. 2015.
- [75] J. Griffin and X. Chen, “Real-time simulation of neural network classifications from characteristics emitted by acoustic emission during horizontal single grit scratch tests,” *J. Intell. Manuf.*, vol. 27, no. 3, pp. 507–523, Jun. 2016.
- [76] J. Griffin, “Traceability of Acoustic Emission measurements for a proposed calibration method - Classification of characteristics and identification using signal analysis,” *Mech. Syst. Signal Process.*, vol. 50–51, pp. 757–783, Jan. 2015.
- [77] B. Wang and Z. Liu, “Acoustic emission signal analysis during chip formation process in high speed machining of 7050-T7451 aluminum alloy and Inconel 718 superalloy,” *J. Manuf. Process.*, vol. 27, pp. 114–125, Jun. 2017.
- [78] M. E. Merchant, “Basic mechanics of the metal cutting process,” *J. Appl. Mech.*, vol. 11, no. A, pp. 168–175, 1944.
- [79] K. A. Bourne, M. B. G. Jun, S. G. Kapoor, and R. E. DeVor, “An acoustic emission-based method for determining contact between a tool and workpiece at the microscale,” *J. Manuf. Sci. Eng.*, vol. 130, pp. 1-8, Jun. 2008.
- [80] M. Fotouhi, P. Suwarta, M. Jalalvand, G. Czel, and M. R. Wisnom, “Detection of fibre fracture and ply fragmentation in thin-ply UD carbon/glass hybrid laminates using acoustic emission,” *Compos. Part A Appl. Sci. Manuf.*, vol. 86, pp. 66–76, Jul. 2016.

- [81] L. Youyuan and L. Zongjin, “Study of the relationship between concrete fracture energy and AE signal energy under uniaxial compression,” *J. Mater. Civ. Eng.*, vol. 24, no. 5, pp. 538–547, May 2012.
- [82] E. N. Landis, “Micro-macro fracture relationships and acoustic emissions in concrete,” *Constr. Build. Mater.*, vol. 13, pp. 65-72, Mar. 1999.
- [83] E. N. Landis and L. Baillon, “Experiments to relate acoustic emission energy to fracture energy of concrete,” *J. Eng. Mech.*, vol. 128, no. 6, pp. 698–702, Jun. 2002.
- [84] S. Muralidhara, B. K. R. Prasad, H. Eskandari, and B. L. Karihaloo, “Fracture process zone size and true fracture energy of concrete using acoustic emission,” *Constr. Build. Mater.*, vol. 24, pp. 479-486, Apr. 2010.
- [85] J. Saliba *et al.*, “Experimental and numerical analysis of crack evolution in concrete through acoustic emission technique and mesoscale modelling,” *Eng. Fract. Mech.*, vol. 167, pp. 123-137, Nov. 2016.
- [86] P. Rovnaník, H. Šimonová, L. Topolář, P. Bayer, P. Schmid, and Z. Keršner, “Carbon nanotube reinforced alkali-activated slag mortars,” *Constr. Build. Mater.*, vol. 119, pp. 223–229, Aug. 2016.
- [87] I. K. Tragazikis, K. G. Dassios, D. A. Exarchos, P. T. Dalla, and T. E. Matikas, “Acoustic emission investigation of the mechanical performance of carbon nanotube-modified cement-based mortars,” *Constr. Build. Mater.*, vol. 122, pp. 518-524, Sep. 2016.
- [88] T. M. Wright, F. Vosburgh, and A. H. Burstein, “Permanent deformation of compact bone monitored by acoustic emission,” *J. Biomech.*, vol. 14, no. 6, pp. 405–409, 1981, doi: 10.1016/0021-9290(81)90058-0.
- [89] P. Zioupos, J. D. Currey, and A. J. Sedman, “An examination of the micromechanics of failure of bone and antler by acoustic emission tests and Laser Scanning Confocal Microscopy,” *Med. Eng. Phys.*, vol. 16, no. 3, pp. 203–212, May 1994.
- [90] O. Akkus, K. J. Jepsen, and C. M. Rimnac, “Microstructural aspects of the fracture process in human cortical bone,” *J. Mater. Sci.*, vol. 35, no. 24, pp. 6065–6074, Dec. 2000.
- [91] Y. Watanabe, S. Takai, Y. Arai, N. Yoshino, and Y. Hirasawa, “Prediction of mechanical properties of healing fractures using acoustic emission,” *J. Orthop. Res.*, vol. 19, no. 4, pp. 548–553, Jul. 2001.
- [92] J. O’Toole, L. Creedon, J. Hession, and G. Muir, “Hyperbolic source location of crack related acoustic emission in bone,” *J. Biomech. Eng.*, vol. 135, no. 1, pp. 1-9, Jan. 2013.
- [93] Z. Ossi, W. Abdou, R. L. Reuben, and R. J. Ibbetson, “Transmission of acoustic emission in bones, implants and dental materials,” *Proc. Inst. Mech. Eng. Part H J. Eng. Med.*, vol. 227, no. 11, pp. 1237–1245, Aug. 2013.

- [94] M. Strantza, O. Louis, D. Polyzos, F. Boulpaep, D. Van Hemelrijck, and D. G. Aggelis, “Measurement of elastic wave dispersion on human femur tissue,” in *Proc. SPIE 9062*, San Diego, CA, USA, Mar. 2014, doi: 10.1117/12.2048393.
- [95] D. G. Aggelis, M. Strantza, O. Louis, F. Boulpaep, D. Polyzos, and D. van Hemelrijck, “Fracture of human femur tissue monitored by acoustic emission sensors,” *Sensors (Basel, Switzerland)*, vol. 15, no. 3, pp. 5803–5819, Mar. 2015.
- [96] J. Zacal, M. Sustr, V. Kumbar, P. Dostal, S. Nedomova, and F. Karasek, “Acoustic emission monitoring of chicken Femurs Firmness in bending tests,” in *Proc. Int. Phd Students Conf., (MENDELNET 2016)*, Brno , CZ, 2016, pp. 699–705.
- [97] B. D. Goodwin, F. A. Pintar, and N. Yoganandan, “Acoustic emission signatures during failure of vertebra and long bone,” *Ann. Biomed. Eng.*, vol. 45, no. 6, pp. 1520–1533, Mar. 2017.
- [98] F. Guan, Y. Sun, X. Qi, Y. Hu, G. Yu, and J. Zhang, “State recognition of bone drilling based on acoustic emission in pedicle screw operation,” *Sensors (Basel, Switzerland)*, vol. 18, no. 5, pp. 1-17, May 2018.
- [99] H. Hajiha and M. Sain, “Model development for work of fracture of hybrid composites,” *J. Appl. Polym. Sci.*, vol. 134, no. 25, pp. 1-7, Mar. 2017.
- [100] T. H. C. Childs and D. Arola, “Machining of cortical bone: Simulations of chip formation mechanics using metal machining models,” *Mach. Sci. Technol.*, vol. 15, no. 2, pp. 206-230, May 2011.
- [101] B. Zeqiri, “Metrology for ultrasonic applications,” *Prog. Biophys. Mol. Biol.*, vol. 93, no. 1–3, pp. 138–152, Jan. 2007.
- [102] A. Moncion, O. D. Kripfgans, P. L. Carson, J. B. Fowlkes, and M. L. Fabiilli, “Characterization of acoustic droplet vaporization and inertial cavitation thresholds in acoustically-responsive tissue scaffolds,” in *IEEE Int. Ultrasonics Symp.*, Chicago, IL, USA, Sep. 2014, pp. 1646–1649.
- [103] P. A. Anderson *et al.*, “Characterizing shock waves in hydrogel using high speed imaging and a fiber-optic probe hydrophone,” *Phys. Fluids*, vol. 29, no. 5, pp. 1-8, May 2017.
- [104] Y. D. Chashechkin and V. E. Prokhorov, “Acoustics and hydrodynamics of a drop impact on a water surface,” *Acoust. Phys.*, vol. 63, no. 1, pp. 33–44, Feb. 2017.
- [105] Y. D. Chashechkin and V. E. Prokhorov, “Fine structure of acoustic signals caused by a drop falling onto the surface of water,” *Dokl. Phys.*, vol. 60, no. 8, pp. 355–359, Sep. 2015.
- [106] V. E. Prokhorov and Y. D. Chashechkin, “Emission of the sequence of sound packets during a drop falling onto the surface of water,” *Dokl. Phys.*, vol. 57, no. 3, pp. 114–118, Apr. 2012.

- [107] Y. D. Chashechkin and V. E. Prokhorov, "Primary acoustic signal structure during free falling drop collision with a water surface," *J. Exp. Theor. Phys.*, vol. 122, no. 4, pp. 748–758, May 2016.
- [108] P. E. Frommhold and R. Mettin, "Acoustic emission due to drop impact on liquid," in *J. Becker-Schweitzer, G. Notbohm (Hrsg.): Fortschritte der Akustik - DAGA 2011 Dusseldorf*, Deutsche Gesellschaft für Akustik e.V. (DEGA), Berlin, DE, 2011, pp. 821–822.
- [109] L. Chen, V. Trinh, W. Yang, and K. Mohanangam, "Prediction of bubble generation based on acoustic emission," *Acoust. Aust.*, vol. 44, no. 2, pp. 325–331, Apr. 2016.
- [110] M. Djabourov, K. Nishinari, S. B. Ross-Murphy, M. Djabourov, K. Nishinari, and S. B. Ross-Murphy, "The sol–gel transition," in *Physical Gels from Biological and Synthetic Polymers*, Cambridge, MA, USA: Cambridge Univ. Press, 2013, pp. 64–96.
- [111] M. Audebrand, J. L. Doublier, D. Durand, and J. R. Emery, "Investigation of gelation phenomena of some polysaccharides by ultrasonic spectroscopy," *Top. Catal.*, vol. 9, no. 3, pp. 195–203, Sep. 1995.
- [112] S. Serfaty, P. Griesmar, M. Gindre, G. Gouedard, and P. Figuière, "An acoustic technique for investigating the sol-gel transition," *J. Mater. Chem.*, vol. 8, no. 10, pp. 2229–2231, 1998, doi: 10.1039/A803722A.
- [113] S. Serfaty, P. Griesmar, M. Gindre, G. Gouedard, and P. Figuiere, "Acoustic resonance tracking in sol gel materials," *Proc. IEEE Ultrason. Symp.*, Sendai, Japan, Oct. 1998, pp. 1171–1174.
- [114] C. Ould Ehssein *et al.*, "Kinetic study of silica gels by a new rheological ultrasonic investigation," *Ultrasonics*, vol. 44, pp. 881–885, Dec. 2006.
- [115] B. Cros, M. Pauthe, M. Rguiti, and J. Y. Ferrandis, "On-line characterization of silica gels by acoustic near field," *Sensors and Actuators B*, vol. 76, no. 1–3, pp. 115–123, Jun. 2001.
- [116] G. Nassar, B. Nongaillard, and Y. Noel, "Monitoring of milk gelation using a low-frequency ultrasonic technique," *J. Food Eng.*, vol. 48, no. 4, pp. 351–359, Jun. 2001.
- [117] J. M. Walker *et al.*, "Nondestructive evaluation of hydrogel mechanical properties using ultrasound," *Ann. Biomed. Eng.*, vol. 39, no. 10, pp. 2521–2530, Oct. 2011.
- [118] P. Chiarelli, M. Carbone, A. Lanatà, and C. Domenici, "High frequency poroelastic waves in hydrogels," *J. Acoust. Soc. Am.*, vol. 127, no. 3, pp. 1197–1207, Mar. 2010.
- [119] S. M. Naseer *et al.*, "Surface acoustic waves induced micropatterning of cells in gelatin methacryloyl (GelMA) hydrogels," *Biofabrication*, vol. 9, no. 1, pp. 1–12, Feb. 2017.
- [120] H. Hsu, "Ultrasonic wave propagation in poly(vinyl alcohol) and articular cartilage," M.S. thesis, Dept. of Mech. Eng., Georgia Inst. of Tech., Atlanta, USA, 2004.
- [121] M. Mridha, S. Ödman, and P. Å. Öberg, "Mechanical pulse wave propagation in gel, normal and oedematous tissues," *J. Biomech.*, vol. 25, no. 10, pp. 1213–1218, Oct. 1992.

- [122] Q. Chen, S. I. Ringleb, T. Hulshizer, and K. N. An, "Identification of the testing parameters in high frequency dynamic shear measurement on agarose gels," *J. Biomech.*, vol. 38, no. 4, pp. 959–963, Apr. 2005.
- [123] K. A. Calzada, J. Samuel, S. G. Kapoor, R. E. DeVor, A. K. Srivastava, and J. Iverson, "Failure Mechanisms Encountered in Micro-Milling of Aligned Carbon Fiber Reinforced Polymers," *Trans. NAMRI/SME*, vol. 38, pp. 221–228, Jan. 2010.
- [124] Z. Feng, J. Rho, S. Han, and I. Ziv, "Orientation and loading condition dependence of fracture toughness in cortical bone," *Mater. Sci. Eng. C*, vol. 11, no. 1, pp. 41–46, Jun. 2000.
- [125] T. P. James, J. J. Pearlman, and A. Saigal, "Rounded cutting edge model for the prediction of bone sawing forces," *J. Biomech. Eng.*, vol. 134, no. 7, pp. 1-11, Jul. 2012.
- [126] L. N. Devin and S. V. Rychev, "The correlation model of acoustic emission in fine diamond turning," *J. Superhard Mater.*, vol. 39, no. 1, pp. 41–48, Mar. 2017.
- [127] Z. Liu, Z. Shi, and Y. Wan, "Definition and determination of the minimum uncut chip thickness of microcutting," *Int. J. Adv. Manuf. Technol.*, vol. 69, no. 5–8, pp. 1219–1232, Jun. 2013.
- [128] E. R. Hughes, T. G. Leighton, P. R. White, and G. W. Petley, "Investigation of an anisotropic tortuosity in a Biot model of ultrasonic propagation in cancellous bone," *J. Acoust. Soc. Am.*, vol. 121, no. 1, pp. 568–574, 2007, doi: 10.1121/1.2387132.
- [129] J. C. Patterson-Kane and E. C. Firth, "Tendon, ligament, bone, and cartilage: Anatomy, physiology, and adaptations to exercise and training," in *The Athletic Horse: Principles and Practice of Equine Sports Medicine: Second Edition*, Amsterdam, NL: Elsevier, 2014, pp. 202-242.
- [130] N. M. B. K. Willems, G. E. J. Langenbach, V. Everts, and A. Zentner, "The microstructural and biomechanical development of the condylar bone: A review," *Eur. J. Orthod.*, vol. 36, no. 4, pp. 479–485, Aug. 2014.
- [131] N. G. Parker and M. J. W. Povey, "Ultrasonic study of the gelation of gelatin: Phase diagram, hysteresis and kinetics," *Food Hydrocoll.*, vol. 26, no. 1, pp. 99–107, Jan. 2012.
- [132] Q. Chen, S. I. Ringleb, A. Manduca, R. L. Ehman, and K. N. An, "A finite element model for analyzing shear wave propagation observed in magnetic resonance elastography," *J. Biomech.*, vol. 38, no. 11, pp. 2198–2203, Nov. 2005.
- [133] J. L. Gennisson and G. Cloutier, "Sol-gel transition in agar-gelatin mixtures studied with transient elastography," *IEEE Trans. Ultrason. Ferroelectr. Freq. Control*, vol. 53, no. 4, pp. 716–723, Apr. 2006.
- [134] E. R. Draper, T. O. McDonald, and D. J. Adams, "A low molecular weight hydrogel with unusual gel aging," *Chem. Commun.*, vol. 51, no. 30, pp. 6595–6597, Mar. 2015.

- [135] Y. Watanabe, S. Inoue, A. Saito, M. Kawakawami, and H. Furukawa, “3D printable inter cross-linking network (ICN) gels for reversible transparency control with water content,” *Microsyst. Technol.*, vol. 9, no. 2, pp. 1-5, Jul. 2019.
- [136] Y. ichi Kinekawa and N. Kitabatake, “Turbidity and rheological properties of gels and sols prepared by heating process whey protein,” *Biosci. Biotechnol. Biochem.*, vol. 59, no. 5, pp. 834–840, 1995, doi: 10.1271/bbb.59.834.
- [137] W. Zhao, Z. Shi, X. Chen, G. Yang, C. Lenardi, and C. Liu, “Microstructural and mechanical characteristics of PHEMA-based nanofibre-reinforced hydrogel under compression,” *Compos. Part B Eng.*, vol. 76, pp. 292–299, Jul. 2015.
- [138] X. Hu, Y. Wang, M. Xu, L. Zhang, J. Zhang, and W. Dong, “Mechanical testing and reinforcing mechanisms of a magnetic field-sensitive hydrogel prepared by microwave-assisted polymerization,” *Polym. Test.*, vol. 71, pp. 344–351, Oct. 2018.
- [139] A. Capelli, J. C. Kapil, I. Reiweger, D. Or, and J. Schweizer, “Speed and attenuation of acoustic waves in snow: Laboratory experiments and modeling with Biot’s theory,” *Cold Reg. Sci. Technol.*, vol. 125, pp. 1–11, May 2016.
- [140] K. Asamene, L. Hudson, and M. Sundaresan, “Influence of attenuation on acoustic emission signals in carbon fiber reinforced polymer panels,” *Ultrasonics*, vol. 59, pp. 86–93, May 2015.
- [141] J. Wang, B. Liu, G. Kan, G. Li, J. Zheng, and X. Meng, “Frequency dependence of sound speed and attenuation in fine-grained sediments from 25 to 250 kHz based on a probe method,” *Ocean Eng.*, vol. 160, no. 6, pp. 45–53, Jul. 2018.
- [142] M. Amarillo *et al.*, “Impact of sound attenuation on ultrasound-driven yield improvements during olive oil extraction,” *Ultrason. Sonochem.*, vol. 53, no. October 2018, pp. 142–151, May 2019.
- [143] C. Sun *et al.*, “The speed of sound and attenuation of an IEC agar-based tissue-mimicking material for high frequency ultrasound applications,” *Ultrasound Med. Biol.*, vol. 38, no. 7, pp. 1262–1270, Jul. 2012.
- [144] R. Abbasi *et al.*, “Measurement of acoustic attenuation in South Pole ice,” *Astropart. Phys.*, vol. 34, no. 6, pp. 382–393, Jan. 2011.
- [145] S. Guerriero *et al.*, “Tissue characterization using mean gray value analysis in deep infiltrating endometriosis,” *Ultrasound Obstet. Gynecol.*, vol. 41, no. 4, pp. 459–464, Aug. 2013.
- [146] L. Obregón and C. Velázquez, “Discrimination limit between mean gray values for the prediction of powder concentrations,” *Powder Technol.*, vol. 175, no. 1, pp. 8–13, Jun. 2007.
- [147] X. Tao, Z. Jiang, S. Ji, H. Chu, D. Yang, and C. Li, “Influence of light intensity and substrate color on dorsal gray color change in *Phrynocephalus helioscopus* and *Phrynocephalus grumgrzimailoi*,” *J. Arid Environ.*, vol. 157, pp. 22–26, Oct. 2018.

- [148] B. Zhou, Y. Heider, A. Blaeser, S. Raith, H. Fischer, and B. Markert, "Simulation of the gelation process of hydrogel droplets in 3D bioprinting," *Proc. Appl. Math. Mech.*, vol. 16, no. 1, pp. 117–118, Oct. 2016.
- [149] M. Zhang *et al.*, "Experimental determination of thermal conductivity of water-agar gel at different concentrations and temperatures," *J. Chem. Eng. Data*, vol. 56, no. 4, pp. 859–864, 2011, doi: 10.1021/je100570h.
- [150] A. S. Ogrenci, O. Pekcan, S. Kara, and A. H. Bilge, "Mathematical characterization of thermo-reversible phase transitions of agarose gels," *J. Macromol. Sci. Part B Phys.*, vol. 57, no. 5, pp. 364–376, Apr. 2018.
- [151] E. A. Zimmermann, M. E. Launey, and R. O. Ritchie, "The significance of crack-resistance curves to the mixed-mode fracture toughness of human cortical bone," *Biomaterials*, vol. 31, no. 20, pp. 5297–5305, Jul. 2010.
- [152] E. A. Zimmermann, M. E. Launey, H. D. Barth, and R. O. Ritchie, "Mixed-mode fracture of human cortical bone," *Biomaterials*, vol. 30, no. 29, pp. 5877–5884, Oct. 2009.
- [153] U. Hansen, P. Zioupos, R. Simpson, J. D. Currey, and D. Hynd, "The effect of strain rate on the mechanical properties of human cortical bone," *J. Biomech. Eng.*, vol. 130, no. 1, pp. 1-8, Feb. 2008.
- [154] D. Sanchez-Molina *et al.*, "Fractal dimension and mechanical properties of human cortical bone," *Med. Eng. Phys.*, vol. 35, no. 5, pp. 576–582, May 2013.
- [155] J. Pearlman, "Cutting velocity effects in bone sawing," M.S. thesis, Dept. of Mech. Eng., Tufts Univ., Medford, MA, USA, 2011.

## APPENDICES

### A.1 Sensor Specifications

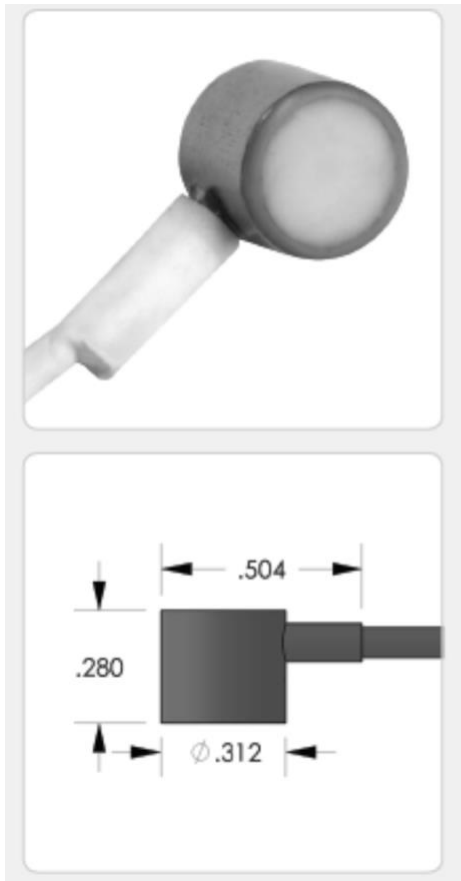
#### A.1.1 Acoustic Emission Sensor

The information presented here comes from the product datasheet of the Nano-30 AE sensor from Physical Acoustics available here:

[http://www.physicalacoustics.com/content/literature/sensors/Model\\_Nano30.pdf](http://www.physicalacoustics.com/content/literature/sensors/Model_Nano30.pdf).

### Nano30 Sensor

#### Medium Frequency Resonant Miniature Sensor



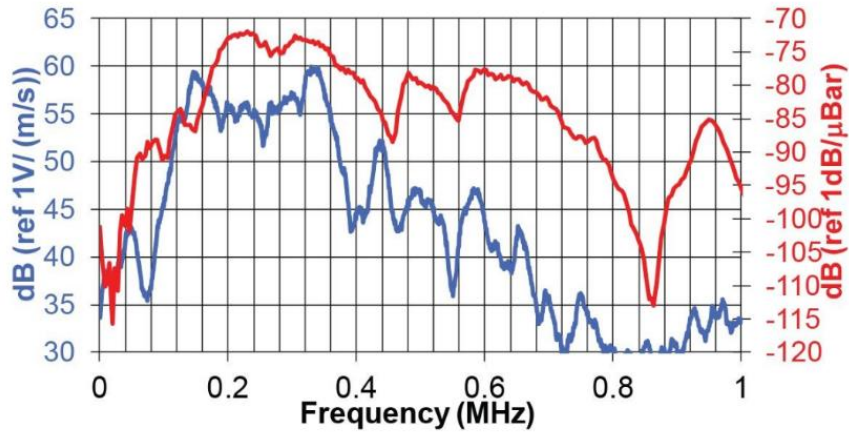
#### DESCRIPTION AND FEATURES

The Nano-30 miniature AE sensor has a resonant response at 300Khz and a good frequency response over the range of 125 – 750 kHz. Its size makes the sensor an ideal candidate for applications where small size is important. The sensor features a small, 1 meter, integral coax cable, which exits from the side of the sensor with a BNC connector on the end.

#### APPLICATIONS

The sensor can be used in any application requiring a small, mid-band frequency response. It can easily be mounted using epoxy and can be mounted in small and tight spaces.

The sensor has a resonant response at 300 KHz, and a good frequency response over the range of 125-750 KHz.



OPERATING SPECIFICATIONS	
<i>Dynamic</i>	
Peak Sensitivity, Ref V/(m/s).....	62 dB
Peak Sensitivity, Ref V/μbar .....	-72 dB
Operating Frequency Range .....	125-750 KHz
Resonant Frequency, Ref V/(m/s) .....	140 KHz
Resonant Frequency, Ref V/μbar .....	300 KHz
Directionality .....	+/- 1.5 dB
<i>Environmental</i>	
Temperature Range .....	-65 to 177°C
Shock Limit .....	500 g
Completely enclosed crystal for RFI/EMI immunity	
<i>Physical</i>	
Dimensions.....	0.3"OD X 0.3"H
.....	8 mm OD X 8 mm H
Weight .....	2 grams (8 with cable & connector)
Case Material.....	Stainless steel
Face Material.....	Ceramic
Connector.....	BNC
Connector Locations.....	Side
ORDERING INFORMATION AND ACCESSORIES	
Nano30.....	Nano30
Cable (specify cable length in meters).....	1 m
Preamplifier.....	0/2/4, 2/4/6
Amplifier Subsystems .....	AE2A, AE5A
Preamp to System Cable (specify length in 'm') .....	1234-X
<i>Sensors include</i>	
NIST Calibration Certificate & Warranty	

### A.1.2 Hydrophone

The information provided here comes from the product datasheet of the Type 8103 Hydrophone from Brüel & Kjær available here:

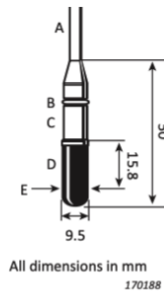
<https://www.bksv.com/-/media/literature/Product-Data/bp0317.ashx>

The sensor has a frequency range of 0.1 Hz to 180 KHz, and a sensitivity of -211 dB re 1

V/ $\mu$ Pa. The sensor details are given below.

Voltage sensitivity with cable at 20°	30 $\mu$ V/Pa $\pm$ 8 $\mu$ V
Charge sensitivity	0.12
Capacitance with integral cable	3850
Frequency range re. 250 Hz	0.1Hz to 20 kHz (+1/ $\square$ 1.5 dB) / 0.1Hz to 180 kHz (+3.5/-12.5 dB)
Operating temperature range short-te...	-30 to +80
Max operating static pressure	252 dB = $4 \times 10^6$ Pa
Dimensions	50 mm (1.97 inch)
Weight including integral cable	170 g (0.37 lb)
Integral cable	6 m waterproof low-noise double-shielded teflon cable with standard miniature coaxial plug

- A: Integral low-noise, double-shielded cable
- B: Mounting seal
- C: Supporting body: CuNi
- D: Lead free, nitrile butadiene rubber
- E: Acoustic centre



#### Miniature Hydrophone Type 8103

A small-size transducer with a high sensitivity relative to its size and good all-round characteristics; applicable to laboratory, industrial and educational use. Its high-frequency response is valuable when measuring pressure-distribution patterns in ultrasonic-cleaning baths, for example.

#### Uses

- Cavitation measurements
- Ultrasonic measurements in liquids
- Acoustic investigation of marine animals
- Laboratory and industrial measurements in liquids and gases
- Noise measurements in humid and polluted atmospheres

#### Features

- Frequency range: 0.1 Hz to 180 kHz
- Receiving sensitivity: -211 dB re 1 V/ $\mu$ Pa
- Very small size (50  $\times$  9.5 mm)
- -3 dB limit in air at 15 kHz
- Integral cable ending with 10-32 UNF connector (male), length from 1 to 400 m (3.3 to 1312 ft)

## A.2 Matlab Codes

### A.2.1 Codes used in Chapter 3

The code below was used to find the forces in the x, y, and z directions from the 6 dynamometer channel signals:

```
file=dat; % signal from dynamometer
```

```

CAx=2.5; %X charge amplification constant (N/V)
CAy=2.5; %Y charge amplification constant (N/V)
CAz=2.5; %Z charge amplification constant (N/V)

%Amplify channels by component CA constants
T=file;
T(:, [1,2])=T(:, [1,2])*CAx;
T(:, [3,4])=T(:, [3,4])*CAy;
T(:, [5,6])=T(:, [5,6])*CAz;

%Low-pass butter filter
fc = 14e3; % cut-off frequency = nyquist frequency
fs = 30e3; % sampling rate 30KHz
[b,a] = butter(4,fc/(fs/2)); % 4th order filter
fT= filter(b,a,double(T(:, :)));

%Combine filtered data
Fx=fT(:,1)+fT(:,2);
Fy=fT(:,3)+fT(:,4);
Fz=fT(:,5)+fT(:,6);
%%%%%%%%%%%%%%%%%%%%%%%%%%%%%%%%%%%%%%%%%%%%%%%%%%%%%%%%%%%%%%%%%%%%%%%%

```

The code below was used to find the work done by the cutting force:

```

%Fc_area is the work done by the cutting force in Nm
%Fx is the cutting force signal (N); x and y are start and end points
%corresponding to a fracture
%Sampling rate is 30e3 samples per s
%Cutting speed is 13.33E-3 m/s (800 mm/min)

Fc_area = trapz(abs(Fx(x:y)))*(13.33e-3/30e3)
%%%%%%%%%%%%%%%%%%%%%%%%%%%%%%%%%%%%%%%%%%%%%%%%%%%%%%%%%%%%%%%%%%%%%%%%

```

The code below was used to plot the cutting/thrust force and AE signals obtained from cutting a workpiece:

```

%Plottting Cutting/Thrust Force and AE signals for a single experiment
%Force signals x1:y1 correspond to AE signal x2:y2

%Fx and Fz are the cutting and thrust force signals
Fx1=Fx(x1: y1);
Fz1=Fz(x1: y1);

%dat_ae is the AE signal
dat_ae1=dat_ae(x2: y2);

th = 1.5e-3;% AE signal threshold

x(1:length(dat_ae1)) = th;

figure
subplot(2,1,1)

```

```

plot(Fx1); hold on; plot(Fz1);
xlabel('Sample')
ylabel('Force (N)')
legend('Cutting Force')
set(gca,'FontSize',30)
set(findall(gca, 'Type', 'Line'),'LineWidth',2);

subplot(2,1,2)
plot(dat_ae1);hold on; plot(x);
xlabel('Sample')
ylabel('Amplitude (N)')
legend('AE Signal', 'Threshold')
set(gca,'FontSize',30)
set(findall(gca, 'Type', 'Line'),'LineWidth',2);
%%%%%%%%%%%%%%%%%%%%%%%%%%%%%%%%%%%%%%%%%%%%%%%%%%%%%%%%%%%%%%%%%%%%%%%%

```

The code below was used to determine some metrics from the AE signal:

```

th = 1.5e-3;%threshold
x(1:length(dat)) = th;
plot(dat);hold on; plot(x);

[yupper,ylower] = envelope(dat,100,'peak');

dat1=dat(1310028:1332554); % manually select the limits
yupper1=yupper(1310028:1332554);

time=(0:length(dat1)-1)/4e6; % sampling rate is 4MHz
ae_amplitude = max(abs(dat1)) % amplitude
ae_marse = trapz(abs(yupper1)) % ae marse
ae_energy = sum(dat1.^2) % ae signal energy
ae_counts = sum(dat1>th) %not abs(dat1)
ae_duration = 1000*(length(dat1)/4e6) % duration in ms
ae_risetime = 1000*time(abs(dat1)==max(abs(dat1)))% rise time in ms
%%%%%%%%%%%%%%%%%%%%%%%%%%%%%%%%%%%%%%%%%%%%%%%%%%%%%%%%%%%%%%%%%%%%%%%%

```

## A.2.2 Codes used in Chapter 5

The code below was used to detect the start and end points of the AE signal corresponding to the multiple cuts on the workpiece, and then plot the trimmed signals:

```

%AE signal from a cut

x=movmean(abs(dat,1000);% dat is AE signal
above_threshold = (x>1e-5);%AE threshold

T = above_threshold';
idx = find(diff([false,T,false]));
b = idx(1:2:end);
e = idx(2:2:end);

```

```

for i = 1: length(e)
plot(dat(b(i):e(i)));
hold on;
end;
%%%%%%%%%%%%%%%%%%%%%%%%%%%%%%%%%%%%%%%%%%%%%%%%%%%%%%%%%%%%%%%%%%%%%%%%

```

The code below was used to find the calibration factors for the AE model:

```

function F = calib_factors(x)

%'dat_hav.mat' & 'dat_plex.mat' have 3 columns corresponding to work rates
%in primary, secondary and tertiary deformation zones

dat_hav = importdata('dat_hav.mat');
y_hav = importdata('y_hav.mat');

dat_plex = importdata('dat_plex.mat');
y_plex = importdata('y_plex.mat');

w1_hav=dat_hav(:,1);
w2_hav=dat_hav(:,2);
w3_hav=dat_hav(:,3);
w1_plex=dat_plex(:,1);
w2_plex=dat_plex(:,2);
w3_plex=dat_plex(:,3);

%Haversian Low DOC
for i = 1:42 %
    F(i) = x(4)*(w1_hav(i)*x(1)+w2_hav(i)*x(2)+w3_hav(i)*x(3))+x(7)-
y_hav(i);
end

%Haversian Medium DOC
for i = 43:76 %
    F(i) = x(5)*(w1_hav(i)*x(1)+w2_hav(i)*x(2)+w3_hav(i)*x(3))+x(8)-
y_hav(i);
end

%Haversian High DOC
for i = 77:104 %
    F(i) = x(6)*(w1_hav(i)*x(1)+w2_hav(i)*x(2)+w3_hav(i)*x(3))+x(9)-
y_hav(i);
end

%Plexiform Low DOC
for i = 105:146 %
    F(i)=x(4)*(w1_plex(i-104)*x(1)+w2_plex(i-104)*x(2)+w3_plex(i-
104)*x(3))+x(7)-y_plex(i-104);
end

%Plexiform Medium DOC
for i = 147:180 %

```

```

        F(i)=x(5)*(w1_plex(i-104)*x(1)+w2_plex(i-104)*x(2)+w3_plex(i-
104)*x(3))+x(8)-y_plex(i-104);
end

%Plexiform High DOC
for i = 181:210 %
        F(i)=x(6)*(w1_plex(i-104)*x(1)+w2_plex(i-104)*x(2)+w3_plex(i-
104)*x(3))+x(9)-y_plex(i-104);
End

%%%%%%%%%%%%%%%%%%%%%%%%%%%%%%%%%%%%%%%%%%%%%%%%%%%%%%%%%%%%%%%%%%%%%%%%
ub = [0.99,0.99,0.99,20e-5,20e-5,20e-5]; %% upper bound
lb = [0.1,0.1,0.1,1e-5,1e-5,1e-5]; %% lower bound

x0 = [0.5,0.5,0.5,13e-5,11e-5,11e-5]; %% initial

rng default

options = optimoptions('lsqnonlin','Display','iter');
options.MaxFunEvals = 20000;
%%%%%%%%%%%%%%%%%%%%%%%%%%%%%%%%%%%%%%%%%%%%%%%%%%%%%%%%%%%%%%%%%%%%%%%%

[x,resnorm,residual,exitflag,output] =
lsqnonlin(@calib_factors,x0,lb,ub,options);

```

## A.3 Supplemental Files

### A.3.1 Permissions for Chapter 2

This file contains the license details and general terms for the reproduction of materials used in Chapter 2 of this dissertation.

**File name:** Chapter2\_Permissions.pdf

**File type:** Portable Document Format (PDF)

**File size:** 1.8 MB

**Required application software:** Adobe Acrobat or any standard PDF viewer

**Special hardware requirements:** None

### A.3.2 Permissions for Chapter 4

This file contains the license details and general terms for the reproduction of materials used in Chapter 4 of this dissertation.

**File name:** Chapter4\_Permissions.pdf

**File type:** Portable Document Format (PDF)

**File size:** 72 KB

**Required application software:** Adobe Acrobat or any standard PDF viewer

**Special hardware requirements:** None

### **A.3.3 Permissions for Chapter 5**

This file contains the license details and general terms for the reproduction of materials used in Chapter 5 of this dissertation.

**File name:** Chapter5\_Permissions.pdf

**File type:** Portable Document Format (PDF)

**File size:** 72 KB

**Required application software:** Adobe Acrobat or any standard PDF viewer

**Special hardware requirements:** None